A NUMERICAL STUDY OF THE 15 DECEMBER 1992 TOGA COARE MESOSCALE CONVECTIVE SYSTEM

By

Badrinath Nagarajan

SUBMITTED IN PARTIAL FULFILLMENT OF THE REQUIREMENTS
FOR THE DEGREE OF DOCTOR OF PHILOSOPHY AT

McGILL UNIVERSITY
MONTREAL, QUEBEC
MARCH, 2000

0-612-64626-2

This work is dedicated to

Sridev Ravalnath of Patt, my mother, father and sisters.

Abstract

A 16-h real data numerical simulation of the growing and mature stages of the 15 December 1992 TOGA COARE mesoscale convective system is performed. One of the objectives of this study is to obtain a realistic simulation of the lifecycle and to determine the factors that regulated the convective onsets. Another objective is to document the impact of the mesoscale convective system and its embedded mesoscale precipitation features on the atmospheric heat and moisture budgets over the warm pool and the surface energy balance of the underlying ocean. The lifecycle of the mesoscale convective system was characterized by the initiation at 0530 UTC of two entities S_1 and S_2, which underwent development and eventually merged to form a large anvil cloud by 1830 UTC. To obtain a realistic simulation of the lifecycle, improvements to the initial moisture field, the convective and surface flux processes in the model were undertaken.

The lifecycle of the mesoscale convective system was realistically simulated. The growing stage was composed of three convective onsets at 0600, 1100, and 1400 UTC. The onsets were governed by three factors: occurrence of convective available potential energy, large scale ascent and a favorable surface potential temperature dropoff. The first onset occurred in a region of convective available potential energy, favorable surface potential temperature dropoff and large-scale ascent associated with the transequatorial flow. The second onset, although located in a region of convective available potential energy and vertical motion associated with a confluence zone, was regulated by the development of a favorable surface potential temperature dropoff from the vertical advection of low potential temperature air in the boundary layer. The third onset lies in a region of moderate convective available potential energy and favorable surface potential temperature dropoff. It was regulated by the evolution of the vertical motion controlled by a quasi-2-day wave. The third onset was responsible for the merger of the entities S_1 and S_2.

The calculated heat and moisture budgets of the mesoscale convective system were characterized by two heating and drying peaks (300 hPa and 925 hPa) with cooling and moistening occurring at midlevels (450 - 700 hPa). The low level heating and drying were associated with deep convection while the upper level heating and drying were the result of deep convection and the vapor deposition process on ice crystals. The midlevel cooling and moistening arose due to sublimation of ice crystals above the freezing level and evaporation of rain and cloud droplets below the freezing level. As the mesoscale convective system evolved, the magnitudes of heating and moistening increased due to the increase in the area occupied by deep convection. Following the convective onsets, the atmospheric boundary layer eddy processes restore the boundary layer to a state to support again deep convection, with a recovery time of about 8 h.

The surface energy balance was not affected by solar radiation because the system evolved nocturnally. Latent heat flux and the net longwave radiation were the two largest components in the surface energy budget. During the second and third convective onsets, the net longwave radiation remained essentially unchanged but the latent and sensible heat fluxes increased. The enhanced surface fluxes during the onsets increased the residual ocean fluxes, particularly over the region occupied by the third convective onset.

Résumé

Le système convectif à méso-échelle observé le 15 décembre 1992 lors de l'expérience TOGA-COARE est simulé numériquement pendant une période de 16 h. Le premier objectif de la présente étude est d'obtenir une simulation réaliste du cycle de vie de ce cas et de déterminer les facteurs de déclenchement de la convection. Un deuxième objectif est de documenter l'impact de ce système convectif et des précipitations qui lui sont associées sur l'environnement à plus grande échelle en terme de dégagement de chaleur latente et d'humidité, tout en étudiant les échange d'énergie avec la surface de l'océan. Le cycle de vie de ce système précipitant est caractérisé par le développement à 0530 UTC de deux entités distinctes S_1 et S_2 qui interagissent entre elles jusqu'à former un important amas nuageux vers 1830 UTC. Afin d'obtenir une simulation réaliste, de nombreuses modifications ont été entreprises, notamment sur le champ initial d'humidité ainsi que sur les paramétrisations de la convection et des flux de surface.

Les différentes étapes du cycle de vie de ce système convectif ont été simulées avec réalisme. Son développement se décompose en trois épisodes convectifs successifs à 0600, 1100 et 1400 UTC intimement liées à trois facteurs : l'existence d'énergie potentielle convective disponible, une ascendance à grande échelle et une chute favorable de température potentielle en surface. Le premier épisode convectif apparaît dans une région où ces trois facteurs sont présents, l'ascendance à grande échelle étant associée au flux trans-équatorial. En plus d'être situé dans une région de convergence potentiellement instable, le second épisode est dû à une chute favorable de température potentielle en surface provenant de l'advection d'air à faible température potentielle vers les basses couches. Enfin, le troisième a lieu dans une région caractérisé par une instabilité modérée, par une chute favorable de température potentielle et par une ondulation de la vitesse verticale de deux jours de période. Cette dernière est responsable de la fusion des deux entités S_1 et S_2.

Les bilans d'humidité et de dégagement de chaleur effectués sur le système convectif simulé montrent deux pics de réchauffement et d'assèchement (au niveaux 300 et 925 hPa), alors qu'un refroidissement et une humidification sont observés à mi-niveaux (entre 450 et 700 hPa). Le réchauffement et l'assèchement sont associés à la convection profonde et, pour le haut du domaine, aux processus de déposition de vapeur sur les cristaux de glace. A l'inverse, le refroidissement et l'humidification à mi-niveaux sont dûs à la sublimation de ces mêmes cristaux de glace au dessus du niveau de congélation, ainsi qu'à l'évaporation des particules de pluie et d'eau nuageuse sous ce même niveau. Au fur et à mesure que le système précipitant évolue, l'amplitude du réchauffement et de l'humidification augmente du fait de l'étalement de la zone de convection profonde. Après chaque épisode convectif, les processus de turbulence rétablissent les basses couches à un état favorable à de nouveaux développement de convection profonde après une période de 8 h environ.

L'équilibre d'énergie de surface n'a pas été affecté par la radiation solaire car le système s'est développé de nuit. Les flux de chaleur latente et les radiations de grande longueur d'onde sont les deux composantes principales du bilan d'énergie de surface. Pendant le deuxième et le troisième épisode convectif, ces radiations restent à peu près stables alors que les flux de chaleur latente et sensible augmentent. Ceci a pour effet d'augmenter le résidu du flux océanique, particulièrement au dessus de la région où se développe le troisième épisode.

Statement of Originality

The following aspects of the study are considered original:

1. The first real data numerical simulation of the lifecycle of a mesoscale convective system (MCS) over the warm pool.
2. Addition of low level moisture in the analysis of the initial moisture field to account for the diurnal warming of sea surface temperature.
3. A demonstration that to simulate successfully the lifecycle of the MCS, it is necessary to:
   - incorporate two additional criteria; the surface potential temperature drop off and the deep column ascent, into the Kain-Fritsch (KF) trigger function.
4. The attainment of realistic anvil cloud coverage and horizontal distribution of surface precipitation in the simulation by the addition of:
   - An alternative treatment for detrainment of cloud water and ice to the KF cumulus parameterization scheme (CPS), and
   - Introduction of accretion as a rain formation process in the KF CPS, and the detrainment of the accreted rain onto the resolvable-scales.
5. The incorporation of the convective gust effects on the surface wind speed to simulate adequately the effects of deep convection.
6. A discovery of the mechanisms that governs the convective onsets in the MCS.
7. A computation of the residue free heat and moisture budgets of the MCS.
8. Calculation of the deep convective effects on the surface energy balance of the warm pool using the simulation results.

Acknowledgements

I would like to thank my supervisors Prof. M. K. Yau and Prof. Da-Lin Zhang for suggesting this research project and allowing great academic freedom to go about the research. Their suggestions at various stages of this work have been invaluable. I am greatly indebted to the innumerable valuable suggestions of Dr. Yubao Liu during the course of this work. A very friendly atmosphere prevailed during the weekly meetings of the mesoscale modelling group at McGill, for which I am very thankful to Liang Ma, Ning Bao, Stephen Dery, Jason Milbrandt, Vasubhandu Misra, Ron McTaggart-Cowan, Yongsheng Chen, David Anselmo and Dov Bensimon. At the beginning of this study I greatly benefited from the help given to me by Dr. Fanyou Kong and Mr. C. Li. My appreciation is extended to Mr. Michel Desgagne and Dr. Robert Benoit who helped me get started with the MC2 modeling system in 1995 and also for providing relevant material for the implementation of the Mercator projection in the model. I wish to thank Dr. Thibaut Montmerle for his help with the translation of the abstract.

Marco Carrera's friendship contributed to the creation of a very pleasant atmosphere admist the daily rigors of doctoral research, and helped me sail through most of the course work during my first year at McGill. My gratitude to all his family members who have made my stay at Montreal a very pleasant experience. Ning Bao's opinion on both the research and personal front have been very helpful especially on occasions when the research phase was going through a very rough patch. I wish to also thank Dr. R. Nair and his wife for the several lunches and dinner we had at his place during 1995-1998. Special thanks to Vasu Misra on the many inputs he gave at any time whenever doubts arose. Special thanks are extended to Stephen Dery for helping with several things. To my friend Ramón de Elía words are not enough to thank him fully for the several suggestions on many aspects of both research, personal and official matters related to an international student. Finally this research study

would not have been possible without the dreams and aspirations of my parents and sisters whose support has been steadfast. Lastly my thanks go to my wife Aruna but for whose help with the typing of the entire thesis, the completion would have certainly been a long and arduous task.

Badrinath Nagarajan

Contents

List of Figures

List of Tables

Chapter 1

Introduction

Beginning in the early 1980's there has been unprecedented interest in the phenomenon of El Ñino. An international effort, in the form of the Tropical Ocean Global Atmosphere program (TOGA) in 1985, has established that the warm pool region over the western Pacific is the center of action for the El Ñino - Southern Oscillation. The warm pool, characterized by sea surface temperatures in excess of 29°C, experiences considerable diabatic heating throughout much of the overlying atmosphere and receives the largest mean annual rainfall in the world (3-5 m year^{-1}, see Webster and Lukas, 1992). The diabatic heating, accompanied by the fresh water flux into the ocean, is realized through deep convective processes modulated on diurnal time scales as well as on time scales of 30-40 days. In particular, the supercloud clusters (Nakazawa, 1988) or the multiday clusters (Mapes and Houze, 1993), associated with the Madden-Julian Oscillation (MJO), represent the longest length and time scales. The tropical cloud clusters or mesoscale convective systems (MCSs) exhibit intermediate scales, whereas individual convective cells occur at the smallest scale.

The development of MCSs over the warm pool significantly impacts the atmosphere and the underlying ocean. Above the sea surface, the cloud cover alters the local radiation budget. The transports by clouds affect the heat, moisture and momentum budgets in the vertical. At the sea surface, the MCS introduces spatial variability in sea surface temperature (SST) through enhanced surface fluxes of latent and sensible heat as a result of the drying and cooling effects of deep convection (Hagan *et al.*, 1997). Hartmann *et al.* (1984) pointed out that the planetary-scale tropical circulation and the communication between the tropics and the higher latitudes change substantially with different vertical profiles of convective heating. Sui *et al.* (1997) suggested that to successfully simulate the multiscale variations in the MJO, both the atmospheric convective processes on the diurnal timescale and ocean mixed layer processes must be resolved.

To resolve the atmospheric convective processes, it is necessary to clarify how convection is organized. Webster and Lukas (1992) consider this a 'zeroth order' problem. Specifically, the lifecycle of the MCS, including the initiation, growing, mature and dissipating stages must be understood. It should be pointed out that Tollerud and Esbensen (1985) distinguished the lifecycle of an MCS from the lifecycle of a mesoscale precipitation feature (MPF). They defined an MCS as a system composed of one or more MPFs. The MPFs appear as entities in radar reflectivity measurements and represent the mesoscale organization of an MCS (Leary and Houze, 1979).

1.1 Stages of lifecycle

During GATE (GARP Atlantic Tropical Experiment), studies were carried out on the lifecycle of the MCSs (Houze and Betts, 1981). On a scale of about a thousand kilometers, the growing, mature, and dissipating stages were identified on the basis of areal-average vertical velocity (Nitta, 1977), and anvil cloud fraction data (Tollerud and Esbensen, 1985). The growing stage is characterized by maximum vertical motion in the lower troposphere and is dominated by convective cells. During the mature stage, the strongest vertical motion shifts to the upper troposphere, because of the development of upward motion in the anvil region. During the dissipation stage, the upward motion collapses in the lower troposphere but remains in the upper troposphere (Tollerud and Esbensen, 1985).

The lifecycle of MPFs in GATE was documented by Leary and Houze (1979). Sherwood and Wahrlich (1999) studied the MPF lifecycle over the warm pool using satellite data. Both of the studies classified the entire lifecycle into the initiation, growing, mature, and dissipating stages. In the initiation stage, also referred to as the convective onset, the MPF takes the form of a line of isolated cumulonimbus cells oriented perpendicular to the low-level flow. Raymond (1995) suggested that warm pool deep convection is initiated when the convective deficit (defined as the difference between the saturation equivalent potential temperature of the cloud layer and the boundary layer equivalent potential temperature or $\theta_{et} - \theta_{eb}$) is close to zero. Specifically convection starts when the equivalent potential temperature of the boundary-layer (θ_{eb}) exceeds the saturation equivalent potential temperature (θ_{et}) of the cloud layer. This increase in boundary-layer equivalent potential temperature is associated with the deposition of the surface fluxes in the boundary layer. With the onset of deep convection, the boundary layer is injected with air of low equivalent potential temperature from the downdrafts to increase the convective deficit. Thus, it was proposed that warm pool convection is regulated by a balance between the tendencies of surface fluxes and convective downdrafts which act to increase and decrease the boundary-layer equivalent potential temperature respectively.

During the growing stage, new convective cells develop between and ahead of existing cells in the outflow regions of convective-scale downdrafts. In the upper troposphere an overhang of cloud and precipitation particles extends downwind in the layer of outflow from convective updrafts. During the mature stage, an MPF is characterized by a region of convective cells along its leading edge and a large area of horizontally uniform precipitation to the rear. The rainfall in the horizontally uniform precipitation area is maintained by organized mesoscale updrafts in the anvil clouds. Beneath the anvil clouds, cooling due to evaporation (melting) of falling rain (ice) drives mesoscale downdrafts. In the dissipating stage, convective cell formation along the leading edge ceases but the area of horizontally uniform precipitation persists for at least several hours longer.

During the lifecycle of the MPFs, complex interaction like mergers and splits among the MPFs were noted. This interaction was referred to as the gregarious behavior of tropical convection (Mapes, 1993) and was associated with gravity waves from deep convection. Mapes (1993) showed that by specifying a heating profile similar to that observed in a tropical MCS, the compensating subsidence required to balance the upward mass flux sets off gravity waves which produced upward displacements in the lowest 4 km in the mesoscale vicinity of the heated region. Air parcels in the ABL were lifted to reach their level of free convection, thereby promoting new convection in the mesoscale vicinity.

1.2 Impact of MCSs

The evolution of MCSs and their associated MPFs introduce spatial and temporal variability in the convective heating profiles over the tropical oceans. The occurrence of MCSs also affects the surface exchange processes.

1.2.1 Heat and Moisture Budgets

Hartmann *et al.* (1984) showed that the tropical atmospheric circulation at the planetary scale and the interaction between tropics and midlatitudes are very sensitive to the specification of the vertical heating profile over the warm pool. Large scale heat

$(Q_1$

(Th ... g GATE

Mor ... istralian

(Yar ... eriment

conv ... num in

the ... than in

profi ... stening

COA ... TOGA

from ... ic, one

(OSA ... array

the e ... l along

the e ... l along

south ... h and

easter ... er the

et al., ... mpson

vectiv ... a con-

region ... iform

Pacific ... tic vs

differe ... ed by

As ...

differe ... are

evapor ... rong

events. ... wind

and a ... iPa)

level dr ... wer-

500 hP ... the

drying ... ible

(1973). ... *t al.*

s at

(Q_1) and moisture (Q_2) budgets computed for the tropical atmosphere during GATE (Thompson *et al.*, 1979), COPT81 (Chong and Hauser, 1990), AMEX (Australian Monsoon Experiment, see McBride *et al.*, 1989) and the Marshall Islands experiment (Yanai *et al.*, 1973) show different characteristics. For instance, the maximum in convective heating over the warm pool occurs at a much higher elevation than in the Atlantic. Lin and Johnson (1996b) described the mean heating and moistening profiles for the warm pool during the intensive observation period (IOP) of TOGA COARE. The heating profiles over two different regions of the western Pacific, one from the intensive flux array (IFA) and the other from the outer sounding array (OSA), were found to be similar. The IFA exhibited a minimum rainfall band along the equator, and the OSA region was characterized by a minimum rainfall band along the equator with a double inter-tropical convergence zone (ITCZ) to the north and south of the equator. Peak heating is located between 400 and 450 hPa. Over the eastern Atlantic ITCZ during GATE, the heating peak is at 600 hPa (Thompson *et al.*, 1979). The Q_1 profile for MCSs was decomposed into a stratiform and a convective part by Houze (1989). He noted that the heating profile in the stratiform region exhibited little variation for MCSs from different regions (tropical Atlantic vs Pacific oceans). Thus, he concluded that the variations in the Q_1 profile is caused by different convective heating under different environmental conditions.

As for the moistening profile, the distribution of Q_2 for the IFA and OSA are different. The IFA region exhibits strong moistening below 850 hPa due to strong evaporation and upward transport of moisture by shallow cumuli during high wind events. The OSA region indicates a double drying maxima (at 700 hPa and 500 hPa) and a minimum in drying near 600 hPa. Johnson (1984) proposed that the lower-level drying peak is a result of cumulus updrafts in the convective region, while the 500 hPa drying comes from mesoscale updrafts within the anvil clouds. Such double drying structure was also reported for the Marshall Islands experiment by Yanai *et al.* (1973). In contrast, the Q_2 profile during GATE (Thompson *et al.*, 1979) peaks at lower levels at around 900 hPa.

The evolution of the heating and moistening profiles over the different stages in the lifecycle of an MCS was studied by Nuret and Chong (1998). They computed the Q_1 and Q_2 profiles for an MCS observed on Nov. 26 and 27 over the warm pool region. During the initial developing stage, the system was dominated by growing shallow cumulus convection. There was heating (peaked at 700 hPa) and drying (peaked at 800 hPa) at the low levels and cooling/moistening below 900 hPa. Later on, an upper-level heating and drying peak (at 400 hPa) appears, indicating the development of shallow clouds to deep clouds. Below 700 hPa, the heating and moistening profiles remained similar to the initial developing stage. During the mature stage, the upper tropospheric heating and drying intensify as a result of latent heating associated with ice processes in the anvil region. There is also heating and drying below 800 hPa, but in the 600 - 700 hPa layer moistening occurs as a result of evaporation of cloud droplets and rain drops. The dissipation stage is marked by considerable weakening of heating and drying in the upper and lower troposphere with midlevel moistening remaining at about the same magnitude. The later stages of dissipation is marked by the presence of shallow cumulus clouds, and therefore, the heating and drying are concentrated below the 700 hPa level.

On a smaller scale, Sherwood and Wahrlich (1999) studied the heating and moistening of MPFs during their lifecycle. They classified rawinsonde temperature and relative humidity data into six stages, namely nonconvective, about to occur, just started, ongoing, about to finish and just finished. A grand mean and anomalies for both temperature and relative humidity were computed using the data from the six stages. The first 3 stages are akin to the developing stage, ongoing is the mature stage and the last two stages are the dissipation stage in the lifecycle of an MPF. The ABL exhibited cooling (1.5 °C) with the onset of the MPF and was caused by the cold convective downdrafts. Cooling in the lower to mid-troposphere (1.2 °C), centered near 725 hPa in the developing stage, rose to 600 hPa by the dissipation stage. The cooling was attributed to the evaporation of stratiform precipitation. There is warming in the upper troposphere (1.3°C), centered near 250 - 275 hPa, during the developing and mature stages, but the warming weakened during the dissipation stage. Cooling above 175 hPa was present, once the onset of the MPF occurred, likely due to dry-adiabatic ascent above the cloud top associated with the mesoscale updraft and cloud-top radiative cooling. In the dissipation stage, slight warming (less than 0.5°C) between 800 and 950 hPa occurred in association with the unsaturated descent of the mesoscale downdrafts in the stratiform region of the MPF. Moistening (nearly 20%) throughout the troposphere above 800 hPa was evident at all stages of the lifecycle. The 850 - 950 hPa layer exhibited drying (less than 10%) during the dissipation stage.

1.2.2 Surface energy balance

Using the time series of flux measurement from the IFA during COARE, Weller and Anderson (1996) concluded that the warm pool loses energy during periods characterized by convective events. Sui *et al.* (1997) suggested that atmospheric radiative-convective processes on the diurnal time scale and ocean mixed layer processes need to be resolved in a coupled model to simulate the multiscale variations that occur in the Intraseasonal Oscillation (ISO).

Grant and Hignett (1998) obtained aircraft data for conditions ranging from undisturbed to moderately disturbed, and computed different terms in the surface energy balance equation for the warm pool region. The dominant terms in the balance are the solar flux and the turbulent latent heat flux. No data were available for the period when MCSs were present. For the case of a convective system (moderately disturbed) the ocean lost energy due primarily to enhanced fluxes of latent heat and reduced solar insolation resulting from the cloud cover. For undisturbed conditions, the net longwave cooling balances the fluxes of sensible and latent heat with surface solar insolation being the dominant term. The high moisture content of the atmospheric surface layer results in significant absorption of the solar radiation and may explain the diurnal behavior of the surface air temperature over the warm pool (Chen and Houze, 1997).

Young *et al.* (1992) undertook a short observational study of the surface energy budget of the warm pool. The data was partitioned to include the convectively disturbed, convectively undisturbed and convectively transitional regimes. The study corroborated the GATE findings that deep precipitating convection has a profound effect on most components of the surface energy budget of tropical oceans. Variations in short wave radiation caused by convective clouds were mostly responsible for the day-to-day variability of the surface energy budget, with surface fluxes being of secondary importance. They also noted variability on time scales of a few hours during convective events.

The warm pool region is characterized by weak wind speeds at the surface (typically less than 1 m s^{-1} near the equator). Thus, one of the goals of the COARE's air-sea interface subprogram was to study the role of deep convection on the surface fluxes under varying ambient surface wind speeds. Jabouille *et al.* (1996) simulated two convective cases observed during COARE that corresponded to light and moderate surface wind conditions. They found local enhancements by a factor of two for the latent heat flux and three for the sensible heat flux in the rainy area, mainly due to increased wind gusts in the region of the convective outflow. They concluded that significant mesoscale variability of the surface fluxes occur in association with deep convection and that considerable attention must be given to the determination of mean wind speed used in the surface flux scheme of the General Circulation Model(GCM) to capture the convectively generated flux enhancement.

In conclusion, observational studies by Mapes and Houze (1987) and Kingsmill and Houze (1999) documented the mature and dissipating stages of the lifecycle of the MCSs. Few numerical simulation studies initialized with three-dimensional observations (or real data simulation) have been performed for the tropical regions and lifecycle studies over the warm pool are absent in the literature. Despite the improved understanding of the mechanisms that regulate the convective onsets, successful prediction of the MCS remains a challenge for meteorologists (Kodama and Businger, 1998). The problem of convective onsets is compounded by the failure of traditional convective indices and the occurrence of sufficient convective available potential energy (CAPE) 90% of the time (Sherwood, 1999). This also hinders real data simulation studies whose success critically depends on correctly predicting the convective onsets (Kain and Fritsch, 1992; Zhang and Fritsch, 1986; Stensrud and Fritsch, 1994). Much of the previous work on the impact of MCSs on the surface processes over the warm pool have been confined to squall line type of systems. However, warm pool convection exhibits diverse modes of organization (Rickenbach and Rutledge, 1998). Thus, a study on the convective effects associated with an MCS and its embedded MPFs are deemed necessary to obtain a better representation of the surface processes over the warm pool.

1.3 Objectives of the thesis

The purpose of this research is to fill a gap in the literature on the lifecycle of MCSs over the warm pool. Our approach is through a real data simulation of the 15 December 1992 TOGA COARE MCS using the Canadian Mesoscale Compressible Community (MC2) model. Specifically, our scientific objectives are to:

1. Simulate realistically the growing and mature stages of the lifecycle of the MCS;
2. Determine the mechanisms that regulate the convective onsets during the lifecycle of the MCS;
3. Study the characteristics of the heat and moisture budgets of the MCS as a

whole and those associated with the MPFs; and

4. Document the effects of deep convection on the surface energy balance of the underlying ocean.

The remaining thesis is organized as follows. The next chapter describes the evolution of the MCS using infrared (IR) imagery, brightness temperature data and airborne Doppler radar data. The large-scale synoptic setting and the preconvective environmental characteristics are also presented. Chapter 3 contains modeling procedures and the improvements to the initial fields of the European Center for Medium-Range Weather Forecasts (ECMWF) analysis. Chapter 4 describes the improvements to the MC2 model. In chapter 5, the CONTROL simulation is verified against available observations obtained from wind profilers, GMS satellite, airborne Doppler radar and buoys. The sensitivity to the convective initiation mechanisms employed in the model is also addressed. Chapter 6 describes the factors responsible for the successful prediction of the convective onsets associated with the MCS's lifecycle. The apparent heat source and apparent moisture sink for the MCS is computed in chapter 7 where the convective effects on the surface energy balance is also presented. A brief summary and concluding remarks are given in chapter 8.

Chapter 2

Case Overview

In this chapter, we describe the development and evolution of a major MCS observed during TOGA COARE (Protat *et al.*, 1998). The MCS was initiated at 0530 UTC 15 December 1992 and lasted till 2330 UTC 15 December 1992. We first trace the evolution of the MCS with the help of the GMS IR imagery and then discuss the large scale dynamic and thermodynamic environment. The structure of the MCS as revealed by air-borne Doppler radar data collected during the mature stage (1700 - 2045 UTC) will also be described.

The large scale synoptic setting was characterized by the Australian Monsoon season. McBride *et al.* (1995) and Lin and Johnson (1996b) documented peak westerly wind burst (WWB) events during the TOGA COARE IOP period, with peak intensity occurring on 1 January 1993. Thus, the MCS occurred two weeks prior to the peak westerly wind burst. In a study of the characteristics of 4-20 day oscillations during the TOGA-COARE IOP, Numaguti (1995) reported the absence of significant wave activity at 850 hPa and 200 hPa in the region 0 - 5°S and 155 - 160°E. Since the wave activity was confined to 190 - 240°E after 23 November 1992, the effects of the 4-20 day period tropical wave are expected to be minimal for this case.

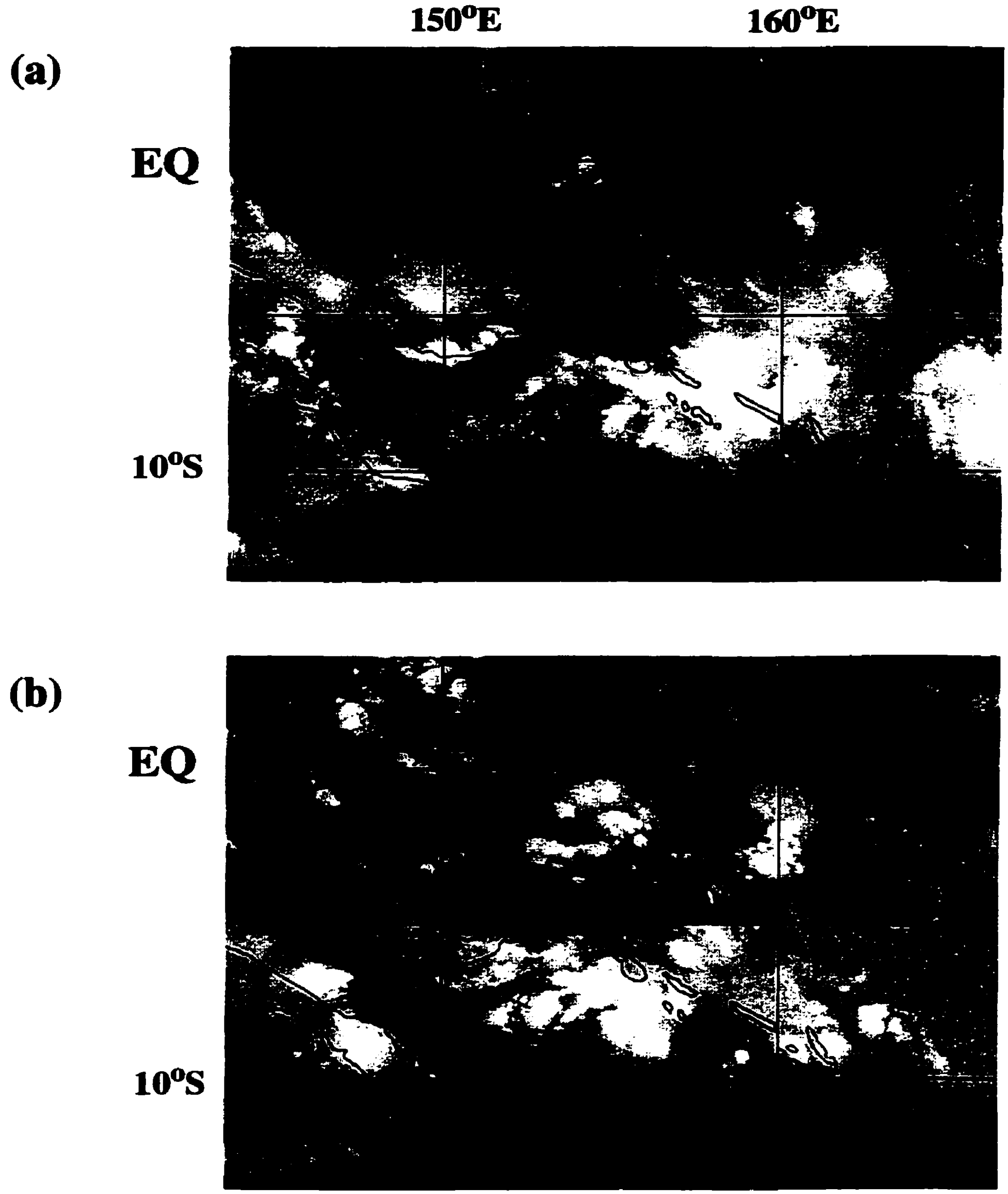

Figure 2.1: Japanese GMS infrared image over study area depicting initiation and development of two systems denoted by S1 and S2 at (a) 0530 UTC and (b) 1023 UTC 15 December 1992 respectively. The merger of S1 and S2 and the mature stage of the mesoscale convective system occur at (c) 1231 UTC and (d) 1831 UTC respectively.

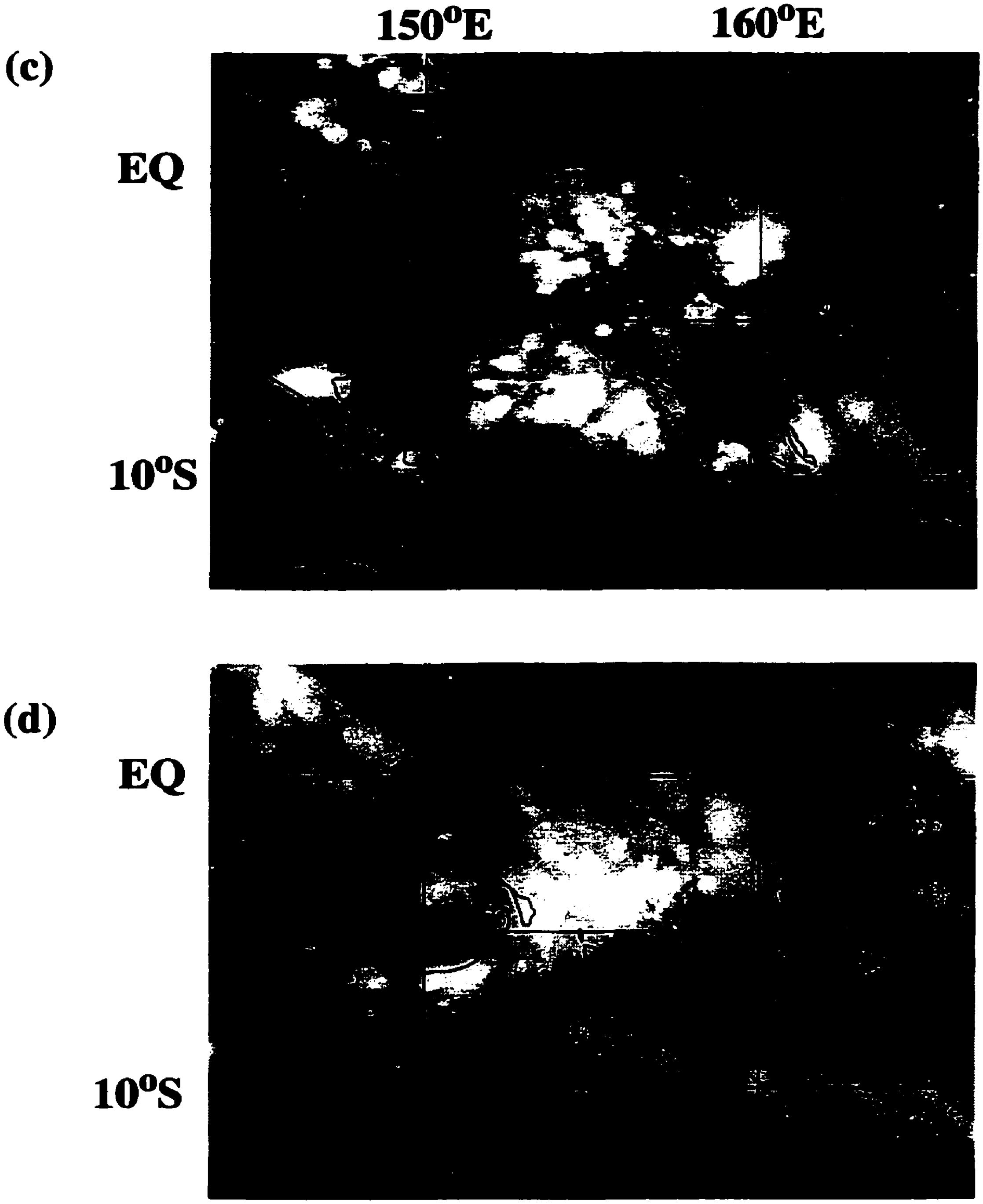

Figure 2.1: Continued.

Figure 2.1 (a) - (d) shows Japanese GMS IR imagery depicting the different stages of the MCS development. Early in the lifecycle, the system was composed of entities S_1 and S_2 (Fig. 2.1a), which developed individually and attained an approximate size of 250 km by 1023 UTC (Fig. 2.1b). At 1231 UTC (Fig. 2.1c) the merger of S_1 and S_2 begins through the onset of new convection between S_1 and S_2. The MCS exhibits a large cloud shield at 1831 UTC (Fig. 2.1d).

The ECMWF analyses were used to obtain the vertical velocity in p-coordinates (ω) at 500 hPa and the CAPE during the preconvective period (0000 UTC 15 December 1992). Figure 2.2 indicates that moderate values of CAPE (shaded regions)

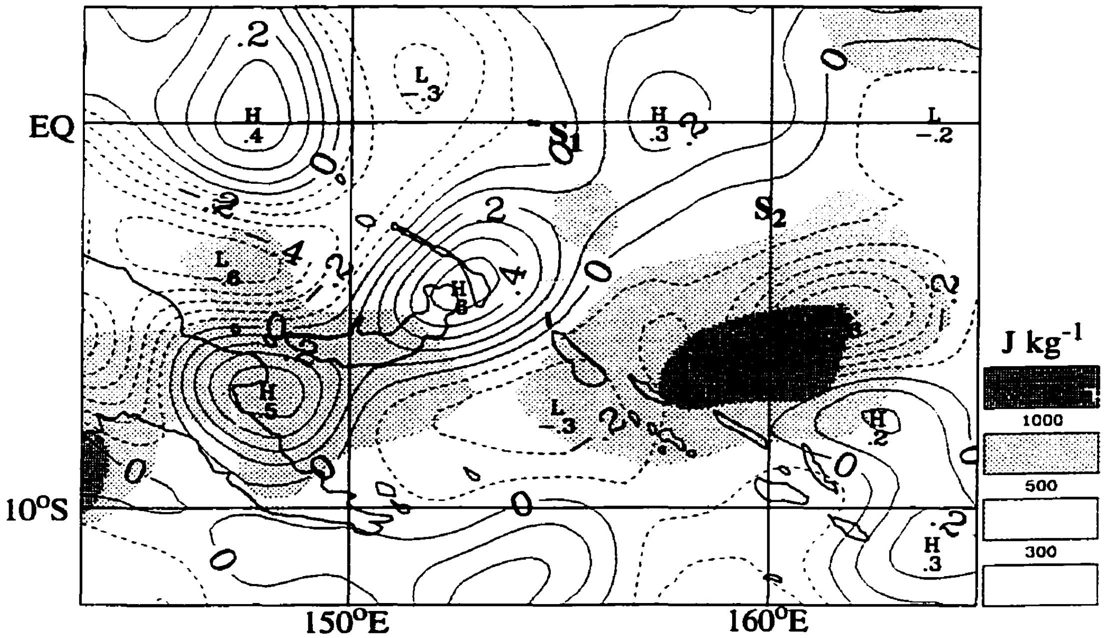

Figure 2.2: Horizontal distribution of vertical velocity at intervals of 0.1 Pa s^{-1} superposed by CAPE (J kg^{-1}) in shade computed from ECMWF analysis for 0000 UTC 15 December 1992. Solid (dashed) lines represent subsidence (ascending motions). The location of the entities S_1 and S_2 at 0530 UTC are indicated.

coincide with upward motion near 5°S, 160°E and 3°S, 145°E where two MCSs are present at 0530 UTC (Fig. 2.1a). However, over the regions where S_1 and S_2 would appear, small CAPE with weak or no vertical motion exists. Nevertheless, the ω field over S_1 and S_2 becomes more favorable with time as is evident from Figures 2.3.

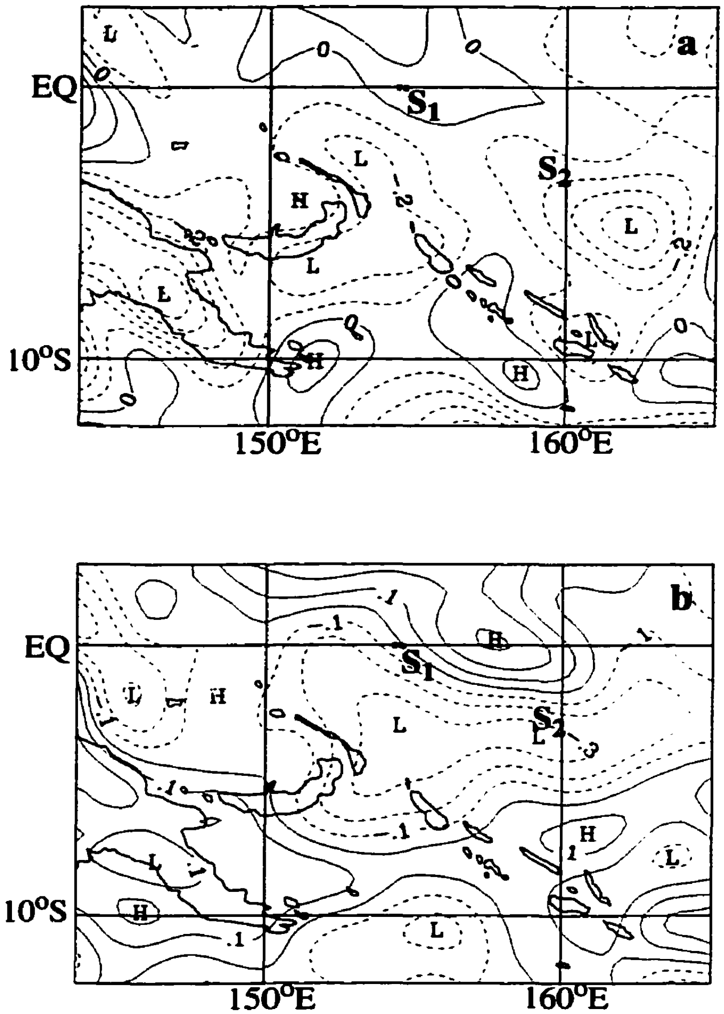

Figure 2.3: As in Fig. 2.2 but for (a) 0600 UTC and (b) 1200 UTC 15 December 1992. CAPE is not shown.

The lifecycle depicted in Fig. 2.1 may be subdivided into 3 distinct stages. Figure 2.4 shows the time variation of the domain-averaged brightness temperature obtained from hourly GMS IR imagery. The domain for averaging is defined between 0 - 5°S and 152.5 - 161°E such that it encompasses S_1 and S_2 during its maximum spatial extent (see Fig. 2.1d). Clearly, between 0530 - 1730 UTC there was a rapid drop

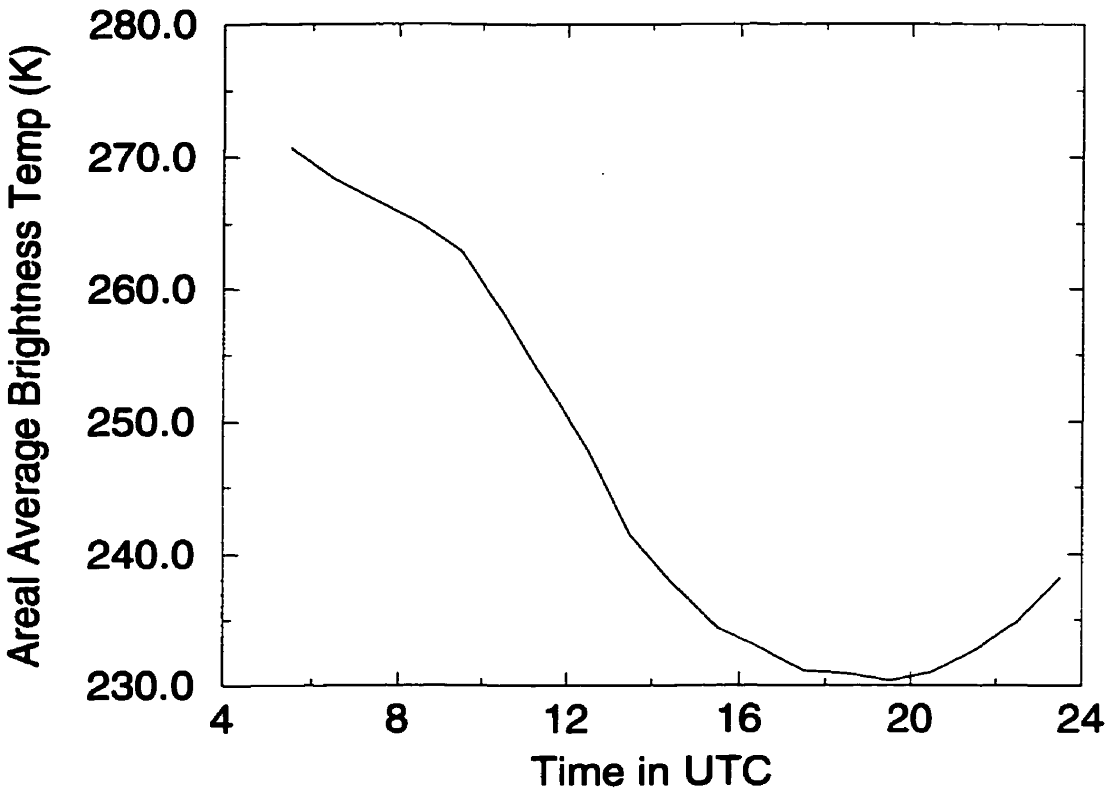

Figure 2.4: Temporal variation of the area-averaged brightness temperature from GMS IR imagery. Averaging area is enclosed by the 0-5°S latitudes and the 152.5-161°E longitudes.

in the brightness temperature indicating a rapid growth of cloud top heights. The existence of an average brightness temperature of $\approx$270 K at 0530 UTC is due to the presence of some cloud cover over the domain (see Fig. 2.1a). In the interval of 0530 - 1730 UTC, S_1 and S_2 were initiated, underwent individual development and merged to form a spatially extensive anvil cloud. This interval will be termed the *growing stage* of the MCS. The interval between 1700 - 2000 UTC clearly exhibits the lowest areal average brightness temperature and the system is almost in a steady state. This interval is designated as the *mature stage* of the MCS. After 2000 UTC there is a rapid increase in brightness temperature signaling the weakening of convective activity and can be viewed as the onset of the *dissipation stage* of the MCS. In the present study, we focus on the growing and the mature stages.

Airborne Doppler radar observation of the MCS during the mature stage was reported by Protat *et al.* (1996, 1998). Doppler wind retrievals and time compositing of the radar data were performed on a mesoscale domain 'M' shown in Figure 3.1. The retrieval domain is a Cartesian grid with a resolution of 5 km rotated 15° in the clockwise direction. Figure 2.5 depicts the time composite (1700 - 2045 UTC) airborne Doppler radar reflectivity data (shaded) and the retrieved wind field at 0.5 km above the sea surface. The two notable features evident in the time composite reflectivity data were the existence of two convective lines designated as L_1 and L_2 with a reflectivity minimum located between the two. Two stratiform precipitation regions are situated to the northwest of L_1 and L_2 respectively (although less developed for L_2). Protat *et al.* (1996) computed the vertical motion in the stratiform regions, which shows subsidence below 3 km and upward motions above with peak values of $\pm$ 10 cm s^{-1}. A vertical cross section through L_1 and L_2 (not shown) indicates stronger vertical motions for system L_1 than L_2 because L_2 was in the decaying stage during this time interval (Protat *et al.*, 1996).

To recapitulate, the MCS under investigation occurred during the Australian monsoon season and two weeks prior to peak WWBs. Its growing stage (0530 - 1700 UTC)

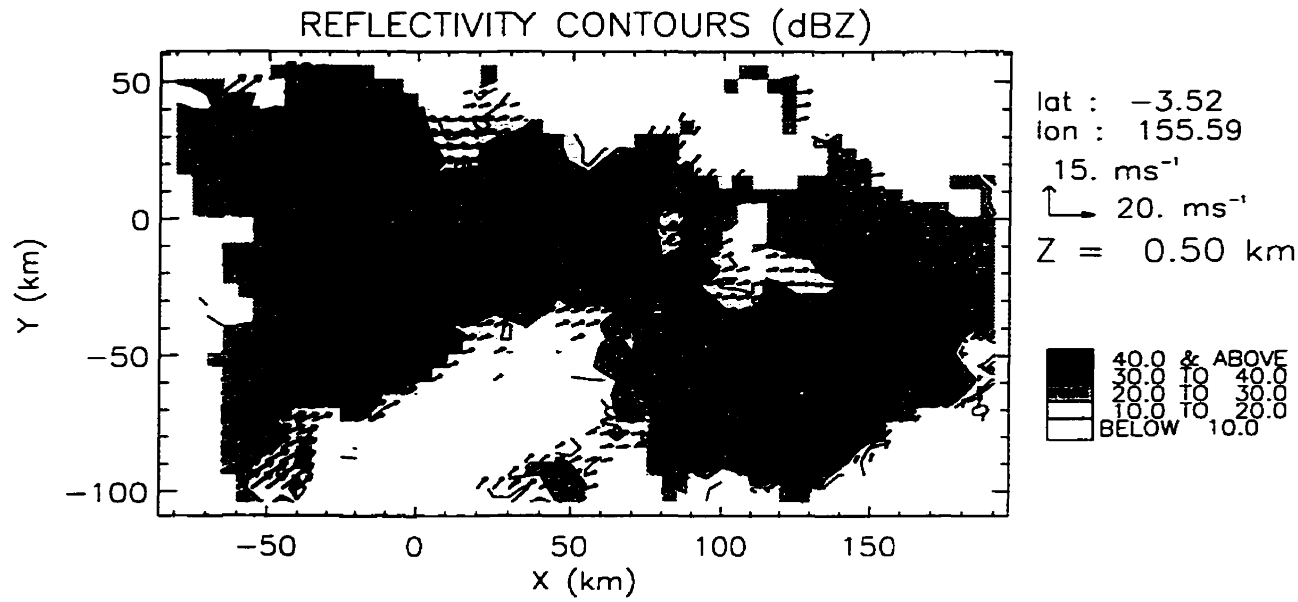

Figure 2.5: Time composite airborne Doppler radar reflectivity (shaded) along with retrieved wind field at 0.5 km height above sea level. The Cartesian grid x-axis is rotated 15° clockwise from true east, see Fig. 3.1. Figure courtesy of Alain Protat.

was marked by the initiation of S_1 and S_2, which eventually merged into a spatially extensive MCS. The mature stage (1700 - 2000 UTC) was observed by airborne Doppler radar. Time composite reflectivity fields (1700 - 2045 UTC) indicated the presence of two lines (L_1,L_2) of deep convection with their associated stratiform regions. The region in between L_1, L_2 showed minimum reflectivity. The stratiform regions exhibited descending motions below 3 km and ascending motion above. The decay of the MCS occurred around 2100 UTC when the area-averaged brightness temperature increases rapidly.

Chapter 3

Modeling procedures and Initial Conditions

3.1 Modeling strategy

An improved version of the Mesoscale Compressible Community (MC2) model is employed (version 3.2, see Bergeron *et al.*, 1994) with two domains, to study the 15 December 1992 MCS. The coarse mesh has a grid size (Δx) of 60 km and the fine mesh has Δx of 20 km. Table 3.1 lists some features of the two domains shown in Figure 3.1.

As described in Appendix A, MC2 is a nested-grid model which allows one-way nesting of variables. The coarse mesh simulation derived its initial and lateral boundary conditions from the ECMWF (1.125° resolution) analyses generated using the PSU/NCAR-MM5 pre-processor systems. The initial moisture field was improved through additional observations as described in section 3.2. The National Center for Environmental Prediction (NCEP) SST analysis was improved by accounting for

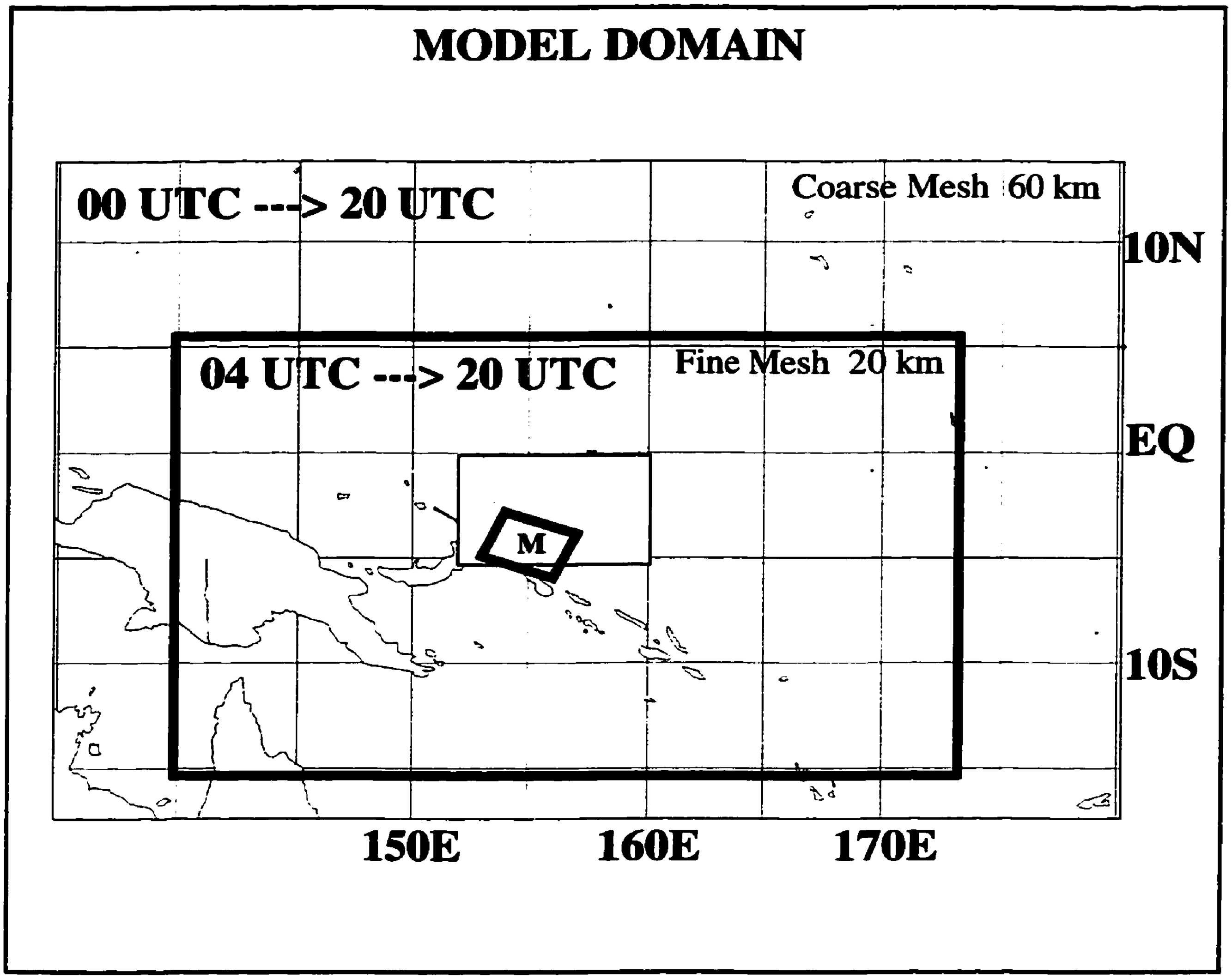

Figure 3.1: Coarse and fine mesh domains used in model simulation along with the duration of integration. Shading depicts the approximate region over which the MCS develops. Grid 'M' depicts the Cartesian grid used for airborne Doppler radar data analysis by Protat *et al.* (1998).

Grid Element Size (Δx)	(x,y,z) dimensions	Simulation Period	Time Step	CPS
60 km	85 × 65 × 25	0000 - 2000 UTC	720 s	BM CPS for deep and shallow convection
20 km	189 × 113 × 25	0400 - 2000 UTC	90 s	KF CPS for deep and BM CPS for shallow convection

Table 3.1: The simulation period, the grid sizes, the time step and CPS used for the coarse and fine mesh simulations. BM and KF stand for Betts-Miller and Kain-Fritsch respectively. CPS denotes cumulus parameterization scheme.

cooling in SST in regions occupied by MCSs between the model initial time and the preceding 6 hours. The reduction in SST was 1.75°C in MCS regions, in accordance with the observations reported by Hagan *et al.* (1997). The initial conditions for the fine mesh simulation were obtained from the coarse mesh simulation at 0400 UTC. The coarse mesh simulation also provided the lateral boundary conditions. The sponge zone for the lateral boundary conditions was 10 grid points wide. Except for the model parameters listed in Table 3.1, all other physical processes were identical in both simulations. The solar and IR radiation schemes were invoked every 30 minutes. ABL processes (surface fluxes, ABL transfer and vertical diffusion in clear air above ABL) and the explicit microphysics processes are also included. Twenty five vertical levels were used. They are 21920.6, 19316.8, 17021.0, 15859.40, 15231.00, 14455.7, 12839.7, 10691.0, 8801.37, 7290.4, 5999.7, 4868.9, 3889.69, 3004.3, 2183.0, 1530.0, 1051.0, 683.75, 416.8, 242.76, 139.8, 73.9, 31.6, 13.42, and 0.0 in Gal-Chen meters. The model top is at 25000 m.

3.2 Initial Conditions

Numerical simulation of MCSs on the meso-β scales have been shown to be critically dependent on two major factors, the inclusion of appropriate model physics and realistic initial conditions. Zhang and Fritsch (1986) emphasized the importance of initial moisture and temperature fields in their simulation of a summer-time mesoscale convective complex. Stensrud and Fritsch (1994), using a subjective mesoanalysis of moisture with addition of mesoscale details, demonstrated a greater probability for a numerical simulation to succeed.

The main difficulty in the conventionally produced analysis is the lack of mesoscale detail in both the temperature and moisture fields, due to the coarse horizontal resolution of the rawinsonde network. This problem is particularly acute for the moisture field and it necessitates other means to improve its initial distribution. One approach is the application of four dimensional data assimilation (Kain and Fritsch, 1992). However, when the technique is applied to regions dominated by convection, as in the western Pacific region (WPR), it is fraught with difficulties (Stensrud and Bao, 1992). Another approach, used successfully by Zhang and Fritsch (1986) and Stensrud and Fritsch (1994), is to augment the observations using artificially constructed dataset.

3.2.1 Improvements to initial fields

Figure 3.2 shows the locations and type of observations used in improving the initial conditions. These improvements may be classified into three major classes: the midlevel moisture field, the low-level moisture, and moisture improvements over data sparse areas that were cloudy.

Most improvements were confined to the moisture field with the exception of locations shown as 'C' in Fig. 3.2 where a composite sounding was used. Nineteen

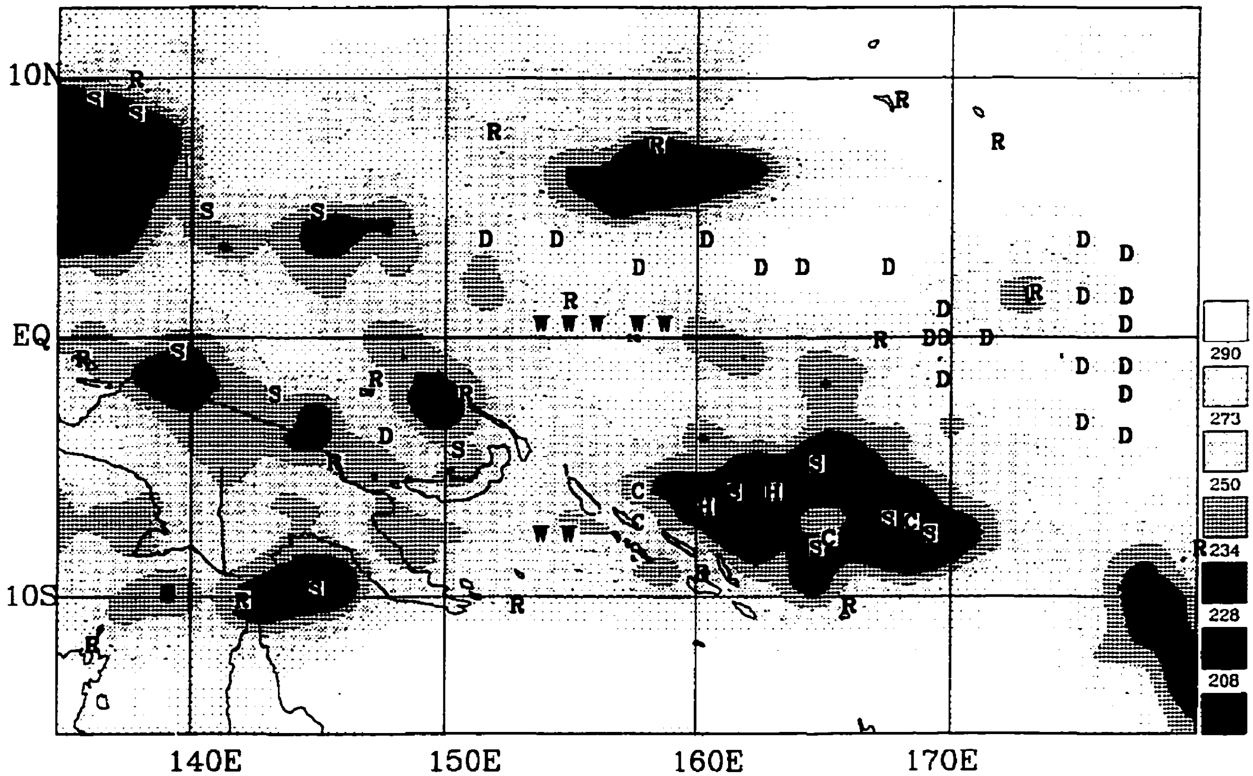

Figure 3.2: Shaded areas show brightness temperature from GMS infrared imagery for 2330 UTC, 14 December 1992 over the coarse model domain. Also shown are locations of different types of observations (upper-air) used to enhance the moisture field. See text for an explanation of the different symbols used.

rawinsonde upper-air observations ('R') were used to enhance the ECMWF analysis into which artificial data were objectively analyzed. These were

- S - Midlevel relative humidity profiles as proposed by Brown and Zhang (1997).
- W - Boundary layer moistening due to diurnal change in SST (Webster *et al.*, 1996; Cooper *et al.*, 1996) .
- C - Composite soundings constructed from aircraft dropsondes and rawinsondes in the 'vicinity' of MCSs during Nov 92-Feb 93.
- H - Deep convective areas with relative humidity $\geq$ 90 percent over a deep atmospheric column in the ECMWF analysis were replaced by Brown and Zhang's rainy period relative humidity profile.
- D - Low precipitation rate regions (as defined by the absence of 208 K IR brightness temperature) where the relative humidity in the 1000-500 hPa layer was reduced.

The basis for the construction of the artificial dataset is described below for the above-mentioned types of data.

3.2.1.1 'S' type data

Lin and Johnson (1996b) computed the IOP mean profiles of relative humidity over the IFA using COARE observations, the ECMWF analysis, and the NCEP analysis. At lower levels, the ECMWF analysis was closer to the observed relative humidity values than the NCEP analysis due likely to the higher vertical resolution in the ABL for the ECMWF analysis. Between 700-400 hPa the ECMWF analysis is too dry with the NCEP analysis being closer to the observations. Beyond the 300 hPa level the relative humidity measurements are questionable due to icing up of the sensors (Lin and Johnson, 1996b). Nuret and Chong (1996) compared the IOP mean ECMWF analysis with three radiosonde station data and obtained similar results.

Tiedtke (1993) used a prognostic instead of a diagnostic cloud scheme and demonstrated how the problem at midlevels could be alleviated. When the prognostic scheme was used, the moistening by evaporation of rain from anvil cloud lead to more realistic midlevel atmospheric moisture structure. The low moisture content at midlevels in the ECMWF analysis was corrected by inserting rainy period humidity profiles of Brown and Zhang (1997) between 700 and 400 hPa levels. Brown and Zhang (1997) presented three mean profiles; the IOP mean, the rainy period mean and the drought period mean using observations taken from three land and four ship sites. The latter two corresponded respectively to the suppressed and active phases of the MJO. The criterion employed for distinguishing the drought period from the rainy period was the rainfall rate over the IFA as measured by microwave sounding unit (MSU), radar and improved meteorological instrument (IMET) buoy. The relative humidity profile of the rainy period between 700-400 hPa was objectively analyzed using the ECMWF analysis as a first guess. The profiles were typically inserted in areas of deep convection as inferred from the 208 K contours (shaded areas in Fig. 3.2).

3.2.1.2 'W' type data

The warm pool region exhibits significant diurnal variation in sea surface temperature. Lukas (1991) documented evidence of the diurnal variation on a ship cruise over a period of 45 days. Chen and Houze (1997) and Fairall *et al.* (1996a) also documented evidence of the diurnal variation. Accurate computation of surface fluxes of sensible heat and latent heat over the warm pool must account for the diurnal changes. Fairall *et al.* (1996a) showed that the skin sea surface temperature can vary by as much as 3°C over the course of a day. The variation of SST was quantified from a synthesis of observations and 1-D ocean mixed-layer model simulation by Webster *et al.* (1996).

Cooper *et al.* (1996) observed that the 950 hPa mixing ratio changes by 1 g kg^{-1} for a step change in SST of 1°C (their Fig. 9). This information enables addition of moisture at low levels (1000 - 900 hPa) at the model initial time, 0000 UTC 15 December 1992, if the change in SST can be estimated. In the present study, the change in SST at the model initial time (1000 LST at 150°E) is estimated by employing the regression relation proposed by Webster *et al.* (1996). The diurnal amplitude of SST depends on daily average surface wind speed, precipitation rate and the peak surface solar insolation. The daily average surface wind speed is determined from the 6 hourly ECMWF analysis for the 24 hours period of 15 December 1992 starting at 0000 UTC. For simplicity, we set the daily precipitation rate to zero. This assumption is expected not to introduce significant errors in the SST amplitude estimates. For instance, the maximum daily precipitation rate during the entire IOP over the IFA was 60 mm day $^{-1}$ or 2.5 mm hr $^{-1}$. This precipitation rate translates to an underestimation of only 0.07°C in the amplitude of the SST.

The peak surface solar insolation (PS) is computed by utilizing the GMS satellite albedo measurements at 2230 UTC 14 December 1992. We assume that this albedo value is valid at local noon over the model domain. By ignoring the effects of water vapor absorption and scattering by air, we have PS = (1-Ac)So where Ac is the albedo and So is the solar constant. Because the low level moistening at model initial time is confined to clear sky columns, our neglect of absorption and scattering effects can lead to overestimation of peak insolation by 20 %. This estimate can be obtained by noting that the true peak solar insolation at sea surface may be written as (McNider *et al.*, 1995)

$$PS_{true} = (1-\alpha)(1-a_t)(1-abs)(1-a_b)(1-A_c)So$$

where

$\alpha \equiv$ the reflection coefficient for beam radiation,

$a_t \equiv$ the water vapor absorption by above cloud-layer,

$abs \equiv$ In cloud water vapor absorption,

$a_b \equiv$ Below-cloud water vapor absorption.

Typical values for these quantities are $\alpha = 0.075$ at local noon (McNider *et al.*, 1995), and

$$a_t = 0.077(\frac{u}{\mu})^{0.3}$$

where u (g cm^{-2}) is the optical path which is numerically the precipitable water and μ is the cosine of the solar zenith angle. We set u to 0.1 g cm^{-2}, yielding $a_t = 0.0386$ if one assumes local noon at all grid points. For below- cloud water vapor absorption,

$$a_b = 0.077(\frac{1.73}{\mu})^{0.3} = 0.091$$

where 1.73 is the precipitable water in the lowest 100 hPa (assuming a cloud base around 900 hPa and a sea level pressure of 1000 hPa). By setting abs to zero for clear sky conditions, the product $(1-\alpha)(1-a_t)(1-abs)(1-a_b) = 0.80$. Therefore, we overestimate PS by 20% in clear sky columns which translates to overestimates in SST amplitudes by the same amount given the relation $\delta T_s = PS(a + d \ln U)$ (Webster *et al.*, 1996). These results are considered as reasonable.

Figure 3.3 shows the diurnal amplitude of SST (δT_s) over the model domain. Areas between 150-165°E, 0-5°N exhibit higher SST amplitudes. This arises due to clear skies (or higher surface insolation) combined with weak surface wind speeds. The region 155-160°E, 0-5°S displays SST amplitudes less than 1°C due primarily to high wind speeds (> 4 m s^{-1}). At the 'W' type data locations (Fig. 3.2), the amplitudes are between 1-2°C

Figure 3.4 shows the CAPE field computed with and without the 'W' type data (or moistening effects due to the diurnal SST change). With the moistening effects, the CAPE at model initial time (0000 UTC 15 December 1992) increases. The coarse simulation between 0000 - 0500 UTC shows that prior to the onset of system S_1 (0530 UTC), the surface latent heat fluxes increase the CAPE in these regions by ≈ 600 J

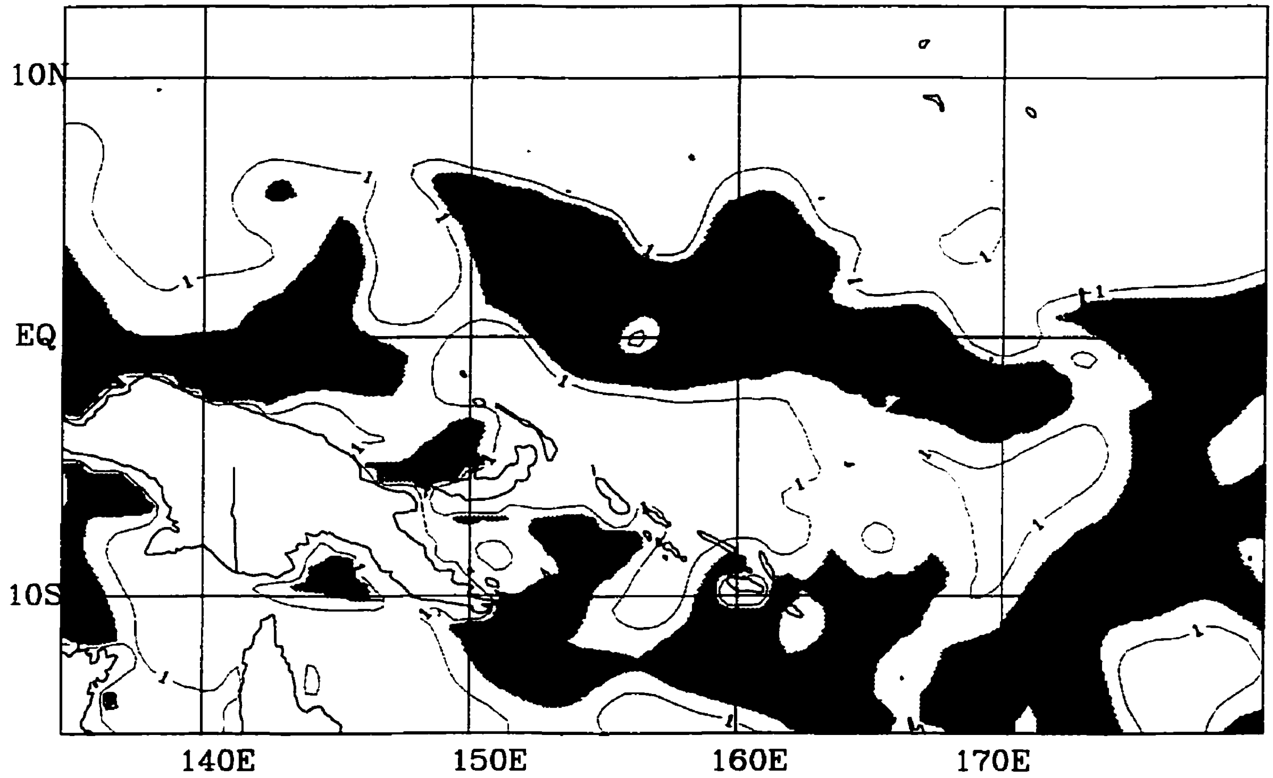

Figure 3.3: Estimated sea surface temperature amplitude (δT_s) for 15 December 1992 over model domain. Shaded areas denote amplitudes $\geq$ 1.5°C.

Kg^{-1}. This suggests that the moistening effects of the diurnal SST change increases the CAPE at model initial time, favoring stronger convection in the S_1 and S_2 regions.

3.2.1.3 'C' type data

As evident from the GMS IR satellite imagery at 2330 UTC 14 December 1992 (see Fig. 3.2), convection is present in several regions. Some major MCSs are located at 155-165°E, 7°N and 5-10°S, 160-170°E. Elsewhere, particularly over 5-10°S, 155-160°E, scattered and deep convection exist. There were upper air observations available at 155-165°E, 7°N. However no data were available over the regions encompassed by 5-10°S, 155-160°E and 5-10°S, 160-170°E. Thus it was desirable to incorporate the convective effects into the initial conditions (T, q_v) in these regions.

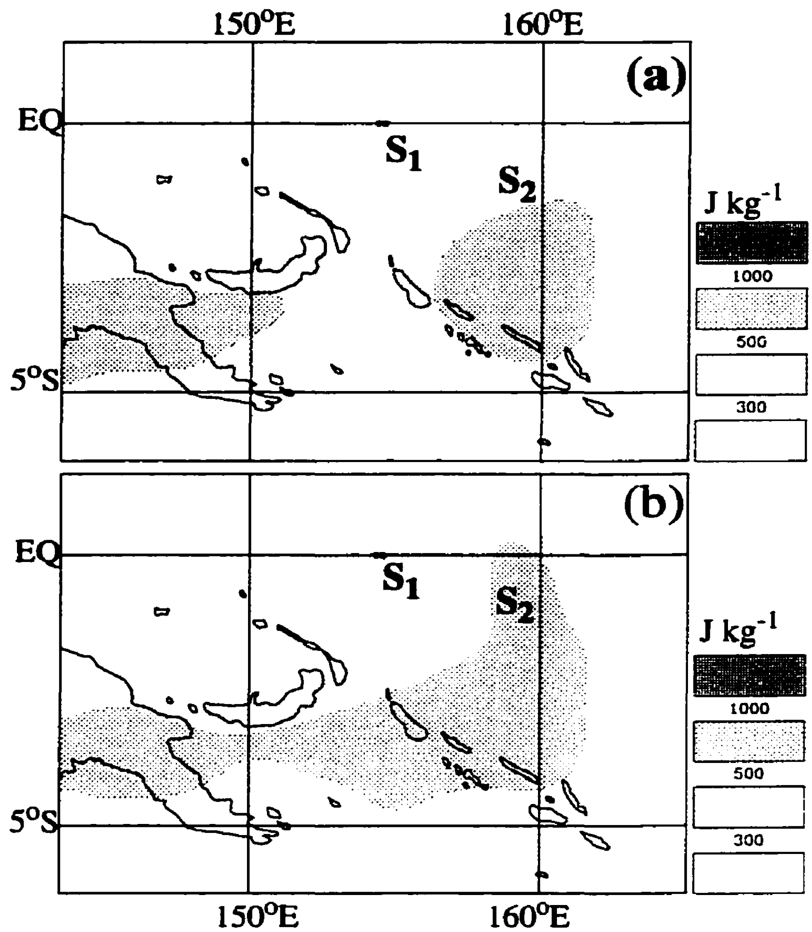

Figure 3.4: Convective Available Potential Energy (J kg^{-1}) at model initial time 0000 UTC 15 December 1992 (a) without moistening and (b) with moistening due to diurnal warming of sea surface temperature. The location of systems S_1 and S_2 at 0530 UTC are indicated. CAPE is computed using the lowest 60 hPa layer mean virtual temperature and specific humidity.

Our approach is to use a composite sounding in regions 5-10°S, 160-170°E and 5-10°S, 155-160°E constructed from aircraft dropsonde and land-based rawinsonde data. The dropsonde data were available from several flight missions during the 4-month IOP period. Since the aim was to improve the representation of the atmospheric state in areas of deep convection, we chose only those dropsonde and rawinsonde that lie in the vicinity of a deep convective system. Our selection of data was guided by radar reflectivity measurements in the case of aircraft dropsondes, but for rawinsondes, the vicinity of deep convection is assumed to be the area enclosed by the 208 K contour for brightness temperature.

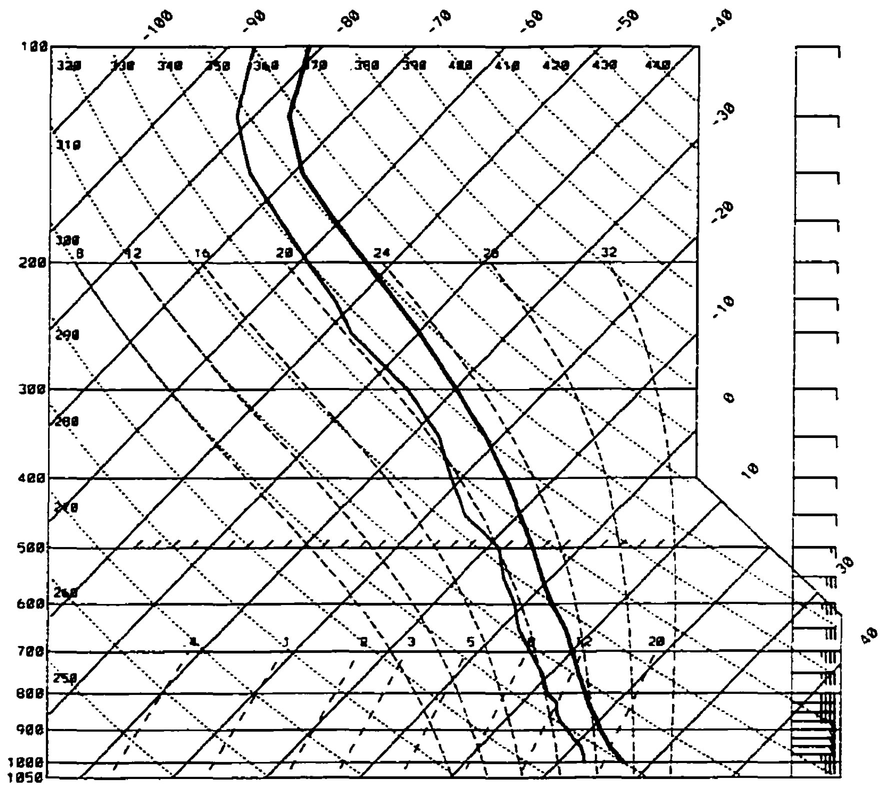

Figure 3.5: Composite sounding constructed from dropsondes, and rawinsondes during the IOP in the vicinity of MCSs. The magnitude of the wind feathers denotes the number of observations used in the composite at various levels.

The composite sounding is shown in Figure 3.5. It reveals a moist atmosphere with a deep conditionally unstable layer. The CAPE and CIN values associated with this sounding are 230 J kg^{-1} and -30 J kg^{-1}, respectively. This is certainly not a favorable sounding for deep convection. However, its use may be justified at the specified locations because one of the regions is associated with a dissipating MCS while the other is associated with scattered deep convection.

3.2.1.4 'D' type data

Areas where this type of observations are located indicate the presence of either shallow cloud tops or clear skies as evident from Figure 3.2. Specifically, hourly infrared GMS imagery during the previous 6 hours, between 1830 - 2330 UTC 14 December 1992, exhibited the following:

1. 0-5°N 150-160°E, a dissipating MCS.
2. 0-5°N 160-170°E, scattered deep convection.
3. 0-5°N 170-180°E, an MCS that propagated westwards from 180°E.
4. 5°S-5°N 170°E, scattered deep convection.

Lin and Johnson (1996a) determined the heating and moistening profiles over the outer sounding array (OSA) and the IFA associated with deep convection for the IOP. The diagnosed Q_2 profile over the OSA is characterized by drying below 200 hPa with the Q_2 profile over the IFA exhibiting moistening in the lowest 150 hPa and drying above. The low-level moistening over the IFA was attributed to moistening by evaporation of precipitation and transport of moisture by shallow cumuli. We used the OSA mean Q_2 profile as the basis to reduce the moisture content at the locations denoted by 'D' in Fig. 3.2. Thus, regions associated with scattered deep convection and dissipating MCS are assumed to exhibit drier conditions in the lower troposphere than the adjoining areas.

The relative humidity in the layer 1000-500 hPa is set to 70%. This procedure resulted in a reduction of relative humidity by 5-10 % between 1000-900 hPa, and about 5 % above 700 hPa. The maximum reduction is about 20 % at 850 hPa level. Our justification is that the D type data occur in data sparse regions where the ECMWF analysis is biased towards the first guess fields. Nuret and Chong (1996) compared the ECMWF analysis with upper-air observations and noted that the former is excessively moist at the low levels but very dry at midlevels. Excessive moisture at low levels is attributed to the production of excessive low-level clouds by the diagnostic cloud model used in the radiation scheme. Slingo (1987) suggested that cloud-top cooling associated with low level clouds produces more low level clouds unless cooling is compensated by the vertical transport of heat due to shallow convective processes (e.g., trade wind regime shallow convection). Tiedtke (1993) addressed this problem using a prognostic cloud scheme and demonstrated a decrease of around 10 % in relative humidity between 1000-500 hPa in the 10°N-10°S latitudinal band. Our reduction in relative humidity reduces the potential to trigger spurious convective activity, which is a major problem in the WPR where deep convection at various stages in their lifecycles simultaneously exist in different regions. Given that the location of this data type is quite removed from the MCS under study, we do not expect significant adverse effect on the simulation of the lifecycle of the MCS.

3.2.1.5 'H' type data

Some areas in the ECMWF analysis exhibited deep moist columns with relative humidity $\geq$ 90% in regions occupied by MCSs at the model initial time. These high values of relative humidity over a deep column may not constitute a realistic humidity condition because the MCSs are already in a well developed stage in their lifecycle. To alleviate this problem, the relative humidity profiles in these regions were replaced by the rainy period relative humidity profiles suggested by Brown and Zhang (1997).

Chapter 4

Model improvements

As mentioned in Chapter 3, a modified version of the MC2 model is employed in this study. The modifications are necessary because MC2 was originally designed for applications in the midlatitudes using a Polar Stereographic projection. To apply it to the tropics, we need a Mercator projection and also make some changes to the physical aspects including those for cumulus convection, the interaction of solar radiation with clouds, and surface flux formulation. The modifications to the system of equations and the model physical processes are summarized in Table 4.1. Interested readers should refer to Appendix A for a more detailed description of the model.

4.1 Dynamical aspects

Modifications to model dynamics include the introduction of the Mercator projection, inclusion of virtual temperature into the system of equations and a refined lateral boundary condition.

Inclusion of the Mercator projection into the model system written on a conformal

Model Improvements	Remarks
Mercator Projection	Eqns. (A.1)-(A.4), section A.2 & 4.1
Virtual Temperature	Eqns. (A.1)-(A.5), section A.2 & 4.1
Lateral Boundary Condition	Section 4.1
Betts-Miller Scheme	Downdrafts & shallow convective initiation, section 4.2
Kain-Fritsch Scheme	Trigger function and cloud water, ice and convective rain detrainment, section 4.2
Surface Processes	TOGA fluxes, solar radiation & clouds, convective gust effects, section 4.2

Table 4.1: Improvements to the MC2 model with the appropriate sections indicated for further details.

projection reduces to the use of a new mapscale factor m (for details see section A.2). The implementation of the Mercator projection is verified against the ECMWF wind field analysis. Figures 4.1 and 4.2 show a comparison of the wind field at 1200 UTC 15 December 1992 obtained from a $\Delta x = 60$ km simulation. The agreement in general is good over the model domain lending confidence to the model performance.

The original system of equations employed temperature as one of the dependent variables. The introduction of virtual temperature into the system of equations allows the air density to be computed on the basis of virtual temperature (rather than temperature) in the pressure gradient terms (right hand side of Eqs. (A.1) to (A.3)). The thermodynamic equation (A.5) is also cast in terms of virtual temperature along the line of Tanguay *et al.* (1989) and Belair (1996).

The lateral boundary conditions in the MC2 model is the Davies-type relaxation scheme (Davies, 1976). This scheme is applied to U, V, T, q_v, and q and optionally to

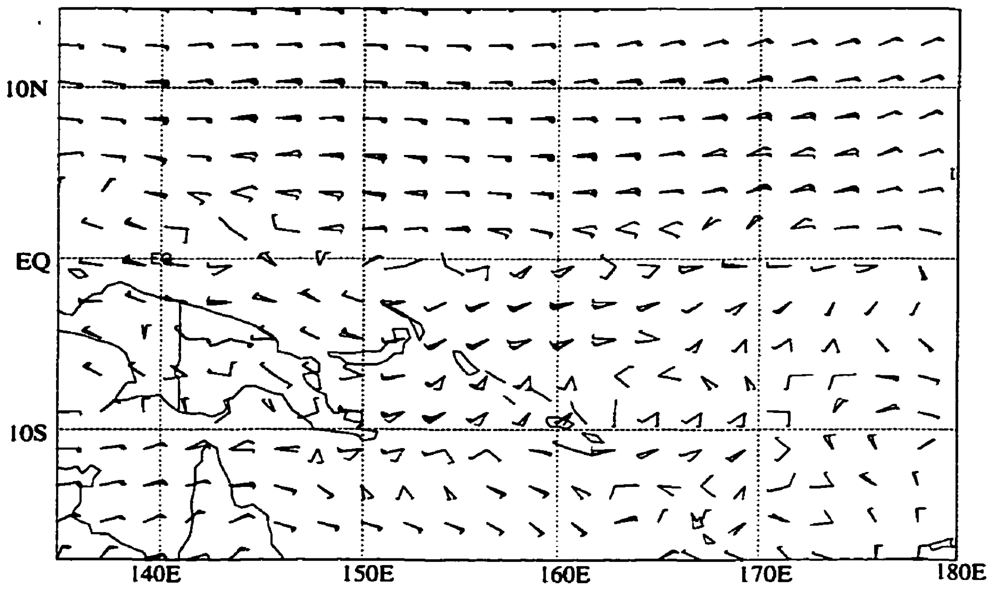

Figure 4.1: The 850 hPa wind field for 1200 UTC 15 December 1992. Thick wind barbs are the ECMWF analyzed wind and thin wind barbs is from the 12 h model simulation with the Mercator projection included in the MC2 model.

w, q_i, q_c and q_r. The relaxation scheme used is

$$\psi_N = \psi_S (1 - P) + P\psi_A$$

where ψ_N is the nested variable, ψ_S is the simulated variable and ψ_A is the driver model/analysis variable. P is the attenuation function of the form

$$P(C_o) = \cos^2\left(\frac{\pi}{2}C_o\right)$$

where C_o is the normalized distance of the point in the sponge zone (typically 10 grid intervals) from the lateral boundary. Thus, ψ_N is a blend of model forecasts and the large scale driver model values in the sponge zone.

A new attenuation function P is introduced following Kallberg (1977). It is given by

$$P = \frac{2\mu_{ri}\Delta t}{1 + 2\mu_{ri}\Delta t} \tag{4.1}$$

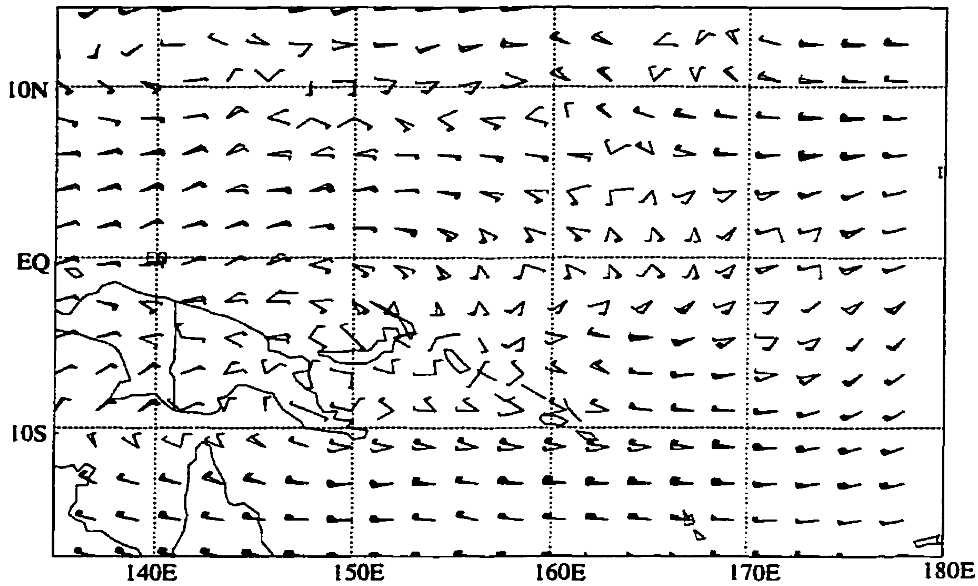

Figure 4.2: Same as Figure 4.1 but for 200 hPa.

with

$$\mu_{ri} = \frac{\alpha_i}{1-\alpha_i}\frac{1}{2\Delta t}\frac{\Delta t}{300}\frac{0.5\times 111.13\times 10^3}{\Delta x}$$

and

$$\alpha_i = 1-\tanh\frac{0.5d_i}{\Delta} \text{ for i} = 1,2,\cdots,10$$

Here $\alpha_o = 1$, d_i is the distance of point i from the lateral boundary and Δ is the grid size.

4.2 Physical Processes

Processes related to cumulus convection, surface fluxes and the effect of clouds on solar radiation need refinement. Modifications to convective processes include the addition of convective initiation mechanisms, an alternate treatment of hydrometeor detrainment in the Kain-Fritsch (KF) cumulus parameterization scheme (CPS) and additional precipitation formation processes in the KF scheme. The explicit microphysics and the evaporation of detrained rain drops from the KF scheme are also addressed. Improvements to the Betts-Miller (BM) CPS include the initiation mechanism for shallow convection and the incorporation of downdrafts in the deep convection scheme.

Fairall *et al.* (1996b) suggested several modifications in the computation of surface fluxes of heat and vapor over the warm pool. Since the simulation covers near-equatorial regions where the surface wind speeds are < 2 m s^{-1}, these modifications are expected to be important. The convective gust effects on the surface fluxes are incorporated along the lines of Jabouille *et al.* (1996). Day time latent heat fluxes over some of the islands turned out to be excessive due to a high potential evapotranspiration. Cloud cover in the form of cirrus clouds occur frequently over the western Pacific region. Heymsfield *et al.* (1998) showed that cirrus clouds associated with deep convection tend to be optically thick, thereby increasing the albedo effect of these clouds on the incoming radiation. Each of the modification will be described in detail along with some motivating factors.

4.2.1 Cumulus convective processes

Downdrafts in the BM scheme

The BM shallow and deep convection schemes are used in the coarse-mesh simulation. The original scheme (Betts, 1986) was designed primarily for tropical convection and downdrafts were neglected which precludes the interaction of deep convection with the ABL processes. It is known that cooling and drying at low levels from convective downdrafts can have an impact on convective development downstream, through advection of the cold and dry air over a period of several hours even under weak surface wind regimes (such as in the WPR where maximum ABL winds are ≤ 7

m s^{-1}). Preliminary tests show that without downdrafts in the coare-mesh simulation grid-scale instabilities (Zhang *et al.*, 1988) occurred downstream of the island of New Guinea late in the fine-mesh simulation.

Following Betts and Miller (1993), we incorporated downdrafts in the original BM deep convection scheme. The downdrafts are parameterized by defining a simple unsaturated downdraft thermodynamic path (constant θ_e and constant subsaturation) originating at 850 hPa. The adjustment time (τ_{ABL}) for this process is a function of evaporation in downdrafts and the deep convective precipitation (PR).

$$\frac{1}{\tau_{ABL}} = \frac{\alpha PR}{\int_{p_o}^{p_{ABL}} \Delta q_c \frac{dp}{g}} \tag{4.2}$$

where the constant α is set to -0.10 in this study and is a measure of the precipitation efficiency of the cumulus clouds. dp is the vertical pressure interval, g is the gravitational acceleration, p_o and p_{ABL} are the respective pressure at the lowest model level and at the top of the ABL, and Δq_c is the change of q_v along the downdraft descent path. Simply put the temperature and moisture profiles for the downdraft are parallel to the moist adiabat at constant subsaturation. The downdraft air is injected into the 3 lowest model levels (in the ABL).

Figure 4.3 shows the 975 hPa difference fields of water vapor mixing ratio and temperature at 0400 UTC 15 December 1992 between the original Betts-Miller scheme and the modified scheme in the coarse mesh simulation. Since the results from the coarse resolution run at this time is used as initial conditions in the fine-mesh simulation, the structure of the difference fields is significant. Note that in areas of deep convection, low level drying and cooling occur. Of importance is the region east of the Island of New Guinea where with downdrafts included into the BM CPS, the ABL was rendered drier and cooler, and the grid point storms were eliminated.

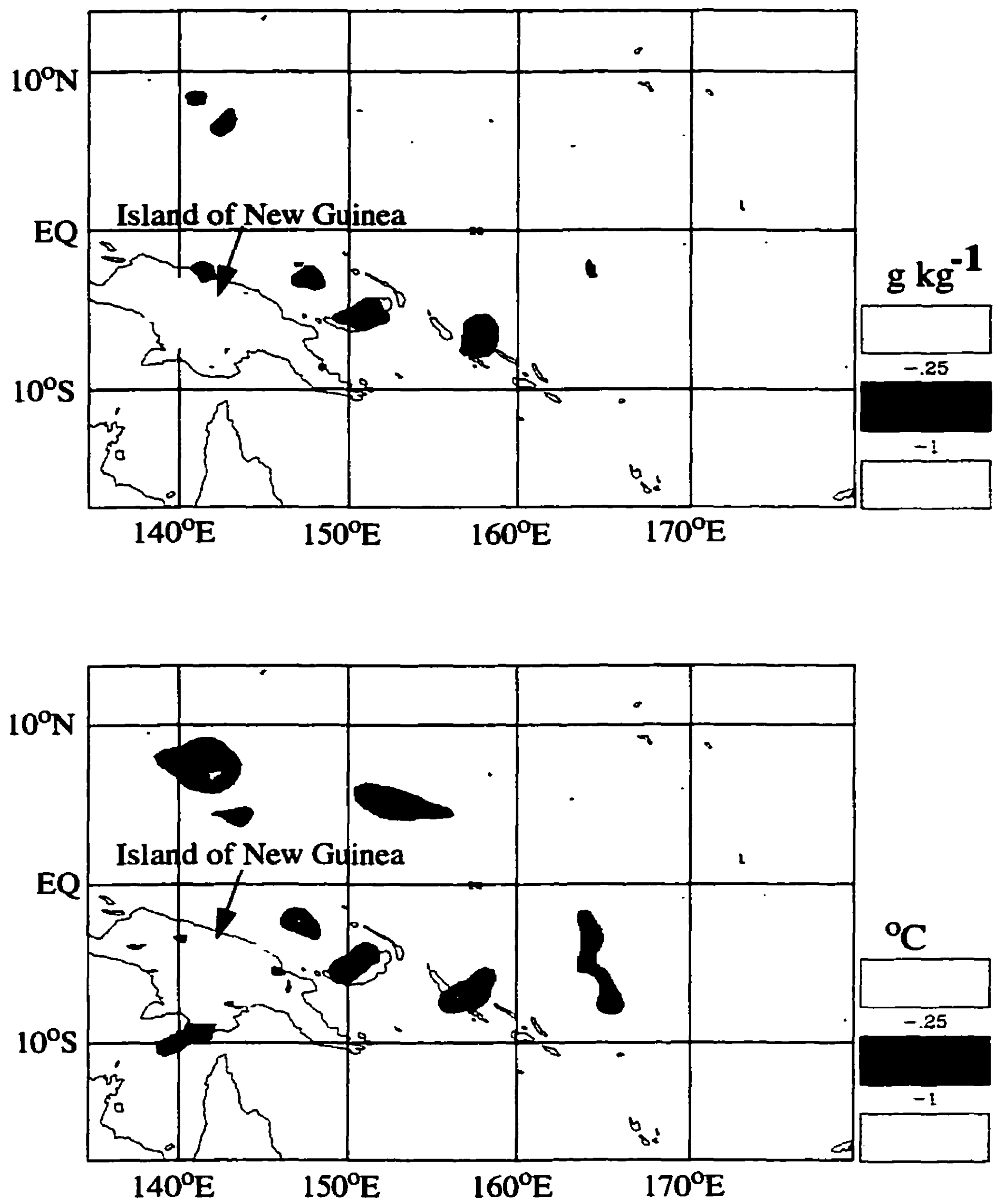

Figure 4.3: Difference field at 975 hPa for 0400 UTC 15 December 1992 for mixing ratio (top) and temperature (bottom) from the coarse mesh simulation. Negative values (shaded) for both mixing ratio and temperature indicate drying and cooling over areas of deep convection and arise due to the parameterized downdrafts in the BM scheme.

Initiation of BM shallow scheme

The significance of shallow cumulus convection has been highlighted in several studies. Using a general circulation model, Tiedtke *et al.* (1988) showed that inclusion of a shallow convection parameterization increased the surface evaporation over the subtropical oceans by as much as 50 W m^{-2}, and consequently enhanced precipitation in some areas of the ITCZ by 10 mm day^{-1}. Gregrory and Miller (1989) emphasized the role of shallow convection in producing realistic moisture profiles below 800 hPa. There exists a wide range of schemes which view shallow cumulus convection as a mixing process between surface layer air and air in the free atmosphere (Siebesma, 1998). Treatment of this mixing process differ from author to author. For instance, Geleyn (1986) proposed to increase the turbulent diffusion coefficient, Siebesma (1998) suggested the use of a mass flux scheme and Betts (1986) advocated the use of a mixing line structure (T, T_d).

The BM shallow scheme has been applied to undisturbed trade wind regions which feature a pronounced inversion near 850 hPa and clouds with bases around 950 hPa. The top of the inversion is marked by a minimum in θ_e which implies a minimum in relative humidity (see Figure 9.2 in Betts and Miller, 1993). In applying the scheme, the cloud top is first calculated. If the calculated cloud top is higher than 700 hPa, the deep scheme is invoked; otherwise the shallow convection scheme is called. When the shallow scheme is called, the grid points in a vertical column is examined as one descends from the specified threshold of 700 hPa. If a sharp increase in relative humidity is found, shallow convection is initiated.

However, the deposition of latent and sensible heat fluxes from the surface by the transport in the ABL may lead to the formation of a near-saturated, conditionally unstable shallow layer. To avoid such unrealistic situation in the model, we also initiated shallow convection if the 20 minute averaged relative humidity between the top of the ABL and the 700 hPa level exceeds 95%.

Kain-Fritsch scheme

We present here a brief summary of the conceptual framework for triggering convection in mesoscale models. The Fritsch-Chappel trigger function proposed by Fritsch and Chappell (1980) is also employed in the Kain and Fritsch (1990) cumulus parameterization scheme. For the sake of consistency we shall refer to the Fritsch-Chappel trigger function as the Kain-Fritsch trigger (KFT) function. The KFT function, its deficiencies and extensions and the modifications used in this study are presented.

Conceptual framework

The criteria determining when and where deep convection will occur are collectively termed as the convective 'trigger function'. This aspect of all CPS remains one of the least developed components (Rogers and Fritsch, 1996). Kain and Fritsch (1992) and Stensrud and Fritsch (1994) showed that some mesoscale simulations can be very sensitive to the trigger criteria used. Unfortunately, the criteria for convective initiation in large-scale models are questionable when applied to mesoscale models (e.g. in the Kuo scheme the moisture convergence, in the Arakawa-Schubert scheme the grid-destabilization rate) primarily due to the development of stronger resolvable scale vertical motion.

The criteria to determine the location and timing of deep convection in mesoscale models will depend on the following two factors:

1. An accurate determination of convective inhibition energy (CIN) between the originating level of the air parcel and its level of free convection (LFC).
2. Whether the large-scale lifting is strong enough to overcome this CIN.

In principle if 1 and 2 are accurately known, the timing and location of convection can be determined in mesoscale models. By definition, CIN is essentially the negative area on a thermodynamic Skew T/Log p diagram between the parcel's originating level and the LFC. To overcome CIN, an impulse buoyancy for an air parcel is first estimated from the grid scale vertical velocity in the Fritsch- Chappel scheme (Fritsch and Chappell, 1980). The relation between the temperature perturbation of the parcel and the vertical motion at its LCL is:

$$\Delta T = C_1 \left(w_G\right)^{\frac{1}{3}} \tag{4.3}$$

where C_1 is a dimensional constant such that a vertical motion (w_G) of 1 cm s^{-1} yields $\Delta T = 1$°C. The original FC trigger mechanism was improved with the inclusion of the effects arising from surface inhomogeneities and convective boundary layer processes by Rogers and Fritsch (1996). However, we did not use this improved trigger function which is expected to be useful over land areas.

Some of the deficiencies in the original KFT function are :

1. Given $\Delta T = C_1 \left(w_G\right)^{\frac{1}{3}}$, it is obvious that when w_G increases with height (true in areas of large-scale ascent such as the ITCZ, quasi-geostrophic forcings etc.) ΔT will also increase, resulting in a greater potential for the KFT to activate.

2. It has been noted in the past that spurious convective activity can arise on account of daytime surface heating over land and also gravity waves resolved by mesoscale models. This has been addressed by Zhang and Fritsch (1986) to some extent although an objective, universal solution is yet to be found.

3. In the original KFT, CIN between the LCL and the parcel originating level is not used in the convective initiation process. Stensrud and Fritsch (1994) incorporated CIN into the KFT function in their study.

Crook (1996) found convective initiation to be most sensitive to surface temperature and moisture dropoff. He suggested that since CIN can be related to the dropoffs, the accuracy of conventional observational systems (with $\pm 1°C$ for temperature and $\pm$ 1 g kg^{-1} for specific humidity) precludes a deterministic view of convective initiation. Thus, improvements in the accuracy of T and q_v measurements in the ABL can lead to better predictability of convective initiation in mesoscale models.

Introduction of additional criteria

In this study, the KFT incorporating the modifications introduced by Zhang and Fritsch (1986) is employed. Additional criteria are introduced as described below because of small tropical CIN values ($\leq$ 10 J kg^{-1}) compared to those reported for midlatitude convection (CIN 60-100 J kg^{-1} LeMone *et al.*, 1998). Also large scale convergence is usually associated with the occurrence of convection (Raymond, 1995). Thus, it remains a challenging task to ensure the occurrence of convection in a mesoscale model at the 'right time' and at the 'right location'.

Deep column ascent

The latent heating associated with tropical MCSs induces vertical motion in the ABL around the MCSs (Mapes, 1993). This ABL lifting occurs due to gravity waves associated with compensating subsidence. Similar occurrence of ABL lifting was suggested as an initiation mechanism for deep convection by Ullrich (1995).

As mentioned earlier, given small CIN values over the warm pool, such ABL lifting due to gravity waves can enable an air parcel from the ABL to easily reach its LFC, thereby initiating convection. Once deep convection is initiated at a particular location, the adjoining regions are in turn rendered favorable through the lifting mechanism. This may lead to the growth of spurious MCSs in the model. To mitigate this type of convective initiation in the model, we impose a condition of deep column ascent as a necessary condition. Deep column ascent is achieved when grid scale vertical velocity w extends upward to at least 600 hPa.

KFT parameters

In the present study, new values for various parameters in the KFT function are used. These new values for the parameters W_{klcl} (the diurnal filter function used to eliminate convection triggered due to day time surface heating, see Zhang and Fritsch, 1986) and C_1 are based on the consideration of weak large-scale forcing. Also the minimum depth of convective clouds to activate the KFT is set to 8 km. This choice is motivated by the results of Rickenbach and Rutledge (1998) who found that convective cloud height distribution is bimodal over the warm pool. One peak lies around 8-9 km while another peak was found around 14-15 km. This new value is twice the value typically used (4 km).

We summarize the new parameter values as follows:

- $W_{klcl} = 0.38$ cm s^{-1} for air parcels (mixed layer) originating in the ABL and $W_{klcl} = 0.76$ cm s^{-1} above the ABL.
- $C_1 = 5.84$, which implies that a grid scale vertical motion of 0.5 cm s^{-1} produces a temperature perturbation of 1°C.
- Minimum cloud depth is 8 km.

Surface Potential Temperature Dropoff (SPTD)

Chen and Houze (1997) attribute the 'diurnal dancing' behavior of deep convection over the warm pool to ABL processes. In other words, an MCS renders the ABL cooler and drier, and therefore stable. It takes about a day for the ABL to recover before it can support deep convection again at the location of the MCS. Thus, any given location over the warm pool is convective every other day. Raymond (1995) associated the occurrence of deep convection over the warm pool with low values of convective deficit, defined as I $= \theta_{et} - \theta_{eb}$, where θ_{et} is the saturated equivalent potential temperature of the cloud layer above the ABL and θ_{eb} is the average equivalent potential temperature of the ABL. Crook (1996) found convective initiation to be most sensitive to SPTD and surface moisture dropoff. In warmer and moist environments (such as the warm pool), he suggested that convective initiation is more sensitive to the SPTD. Given the important role of ABL processes in the initiation of deep convection over the warm pool we were led to the design of an additional function (the SPTD) to be used in conjunction with the KFT function.

The SPTD function is defined as

$$\Delta\theta_{surf} = \theta_{SST} - \overline{\theta}_{ABL} \tag{4.4}$$

where θ_{SST} is the sea-surface potential temperature and $\overline{\theta}_{ABL}$ is the ABL mean potential temperature. Crook (1996) defined $\Delta\theta_{surf}$ as the difference between surface air potential temperature and the ABL mean potential temperature. In models, no superadiabatic air layers occur due to the vertical diffusion scheme (see section A.4.1 for more details). Therefore we employ θ_{SST} in its place.

Interpretation of SPTD and its relation to the KFT

The schematic in Figure 4.4 illustrates the decrease in CIN due to an increase in surface air temperature T_{surf} by ΔT_{surf}. The CIN for the original sounding is reduced due to the increase in surface temperature. The decrease in CIN in the saturated part of the sounding is approximately (Crook, 1996)

$$\Delta CIN_{sat} \approx R\Delta T_{sat} \ln\left(\frac{p_{lcl}}{p_{lfc}}\right) \tag{4.5}$$

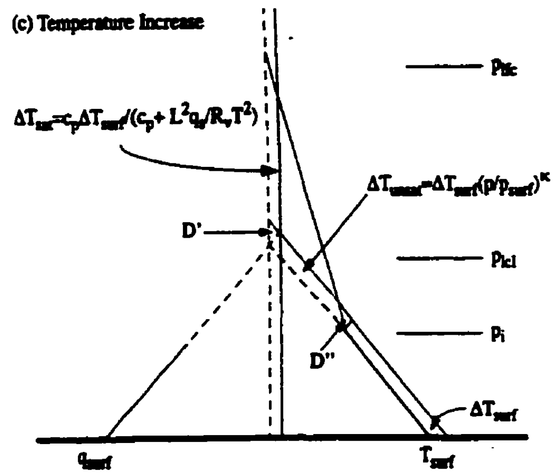

Figure 4.4: Schematics illustrating decrease in CIN in the unsaturated and saturated part of a sounding due to an increase in the surface air temperature T_{surf} by ΔT_{surf}. Reproduced from Crook (1996).

and the decrease in CIN in the unsaturated part is

$$\Delta CIN_{unsat} \approx R\Delta T_{surf}\left(\frac{\overline{p}}{p_{surf}}\right)\ln\left(\frac{p_{lcl}}{p_i}\right) \tag{4.6}$$

where $\overline{p}$ is a mean pressure between p_i and p_{lcl} and ΔT_{sat} is as shown in the figure.

Thus physically when ΔT_{surf} is large, the decrease in CIN is also large. This suggests that with a large SPTD (i.e. $\Delta\theta_{surf}$) convective initiation is highly probable. Since our objective is restricted to the onset of new convection in the model at a grid point, we expect the existence of some threshold value ($\Delta\theta_{surf}$) which correlates with the new convective areas. In other words there exists a value of ΔT_{surf} (say threshold value) for which there is a maximum overlap between areas of new convection and areas enclosed by the ΔT_{surf} threshold-value contour. To quantify the overlap of these two areas, we define a parameter (TS) as:

$$TS = \frac{C}{F} \tag{4.7}$$

where C is the number of grid points where there is an observed convective onset and the SPTD (or ΔT_{surf}) exceeds a threshold value. F is the total number of grid points where SPTD exceeds the threshold value. Thus, the parameter TS represents the fraction of the area enclosed by the SPTD threshold-value contour where convective onsets are observed. The value of TS ranges between 0 and 1. The technique proposed by Sherwood and Wahrlich (1999) is used to determine the convective onsets from hourly GMS IR imagery. New convection is assumed to start at time t, if the cloud fraction associated with the 208 K brightness temperature exceeds 0.1 for the first time within the previous 3 h.

Figure 4.5 shows the variation of the TS parameter with $\Delta\theta_{surf}$ at 0400 UTC 15 December 1992 (the model initial time for the fine mesh simulation). Clearly, TS reaches a maximum when SPTD is close to 1.2°C. This value of SPTD is therefore chosen as a necessary condition for deep convection to occur.

We also found that spurious convective activity occurred in the simulations around sunset time. This primarily happens because $\overline{\theta}_{ABL}$ (causing the SPTD to exceed the threshold value) decreases when solar heating effects are turned off at sunset. Thus we subtract out the increase in $\overline{\theta}_{ABL}$ due to solar radiation (i.e. made independent of solar heating effects).

In summary, the KFT function is extended by the inclusion of two additional criteria; the deep column ascent and the SPTD function. Also new values were used for some parameters in the KFT function. The modified trigger function is depicted schematically in Fig. 4.6.

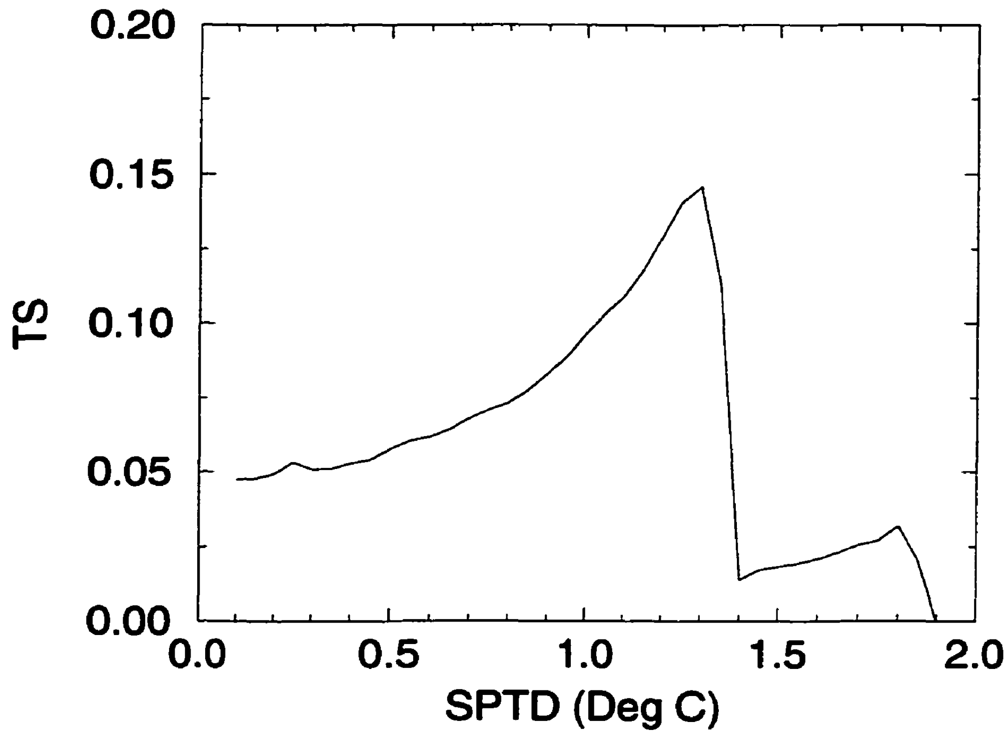

Figure 4.5: Variation of the parameter TS (the fraction of the area enclosed by the SPTD contour where convective onsets are observed) with the SPTD for 0400 UTC 15 December 1992.

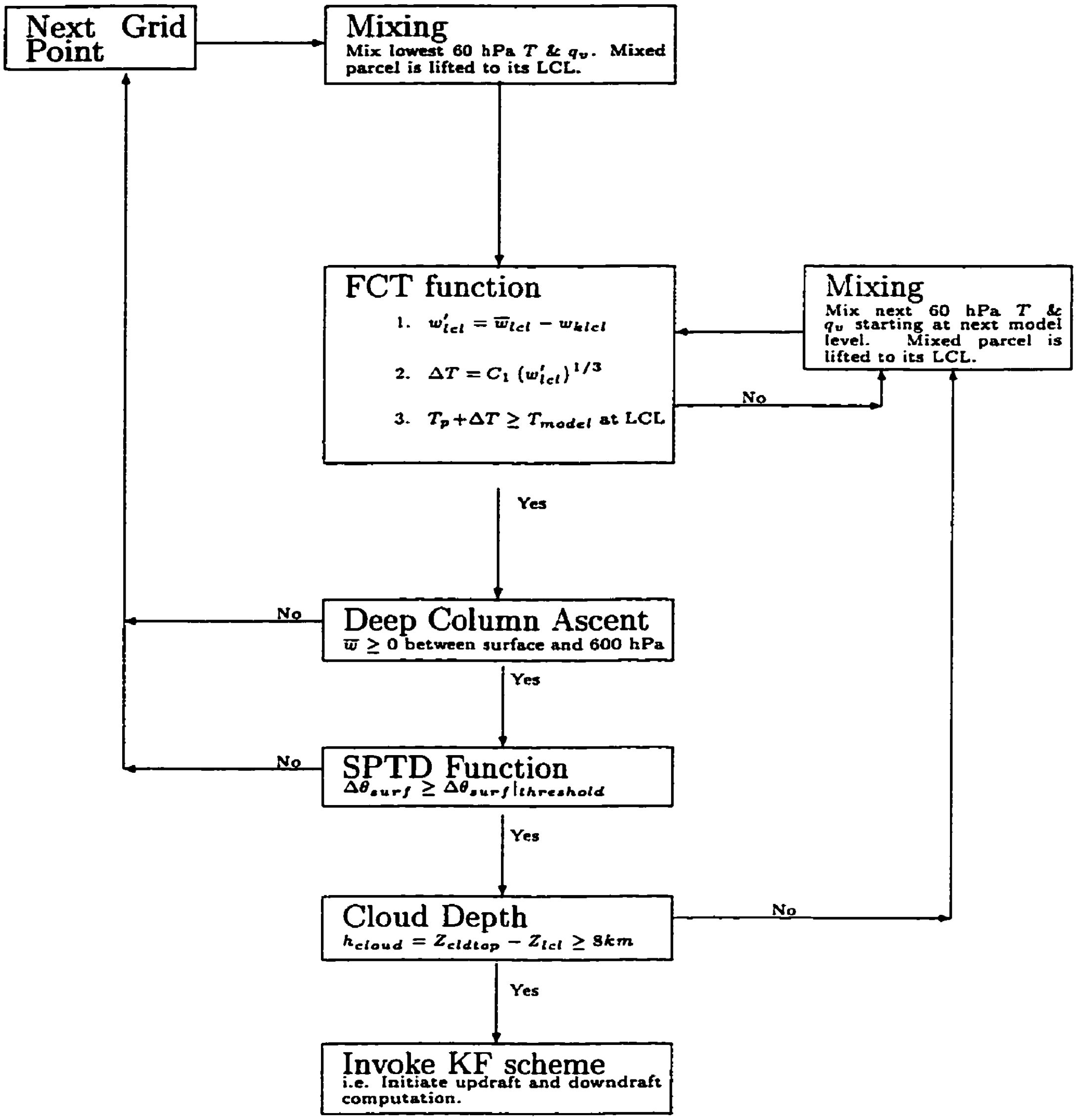

Figure 4.6: Modified Kain-Fritsch Trigger function used in the present study

Detrainment of hydrometeors (q_c^{KF}, q_i^{KF})

Significant amount of moisture supply for stratiform precipitation in MCSs originates from deep convective clouds (Leary and Houze, 1980). Molinari and Dudek (1992) pointed out that the successful simulation of MCSs depends critically on mid and upper tropospheric moisture supply from convective clouds. In the Kain and Fritsch (1990) scheme this moisture supply at the mid- and upper-troposphere comes from detrainment of vapor and hydrometeors (q_c^{KF}, q_i^{KF}) because of mixing between cloudy and clear air.

The hydrometeor feedback in the original KF CPS is given in Appendix A.4.4.2; here we present the modifications. It is clear from equations (A.30) and (A.31) that in the original KF CPS, ice and cloud water are detrained at each level from the cloud base to the cloud top with a magnitude depending on the updraft detrainment rate (δ_u) and layer-mean hydrometeor content. In the present study, we assume that detrainment takes place only in a 150-200 hPa layer below the cloud top. The amount of detrained cloud and ice contents are the accumulated detrainment values for q_c^{KF} and q_i^{KF} between cloud base and 300 hPa in the original KF CPS. We found that this modification results in a realistic cloud coverage over the model domain when compared to GMS IR imagery (see Chapter 5). In addition, we assume that all hydrometeors are liquid if $T > 0°C$ and ice if $T < 0°C$ (i.e., only q_c^{KF} exists when $T > 0$ and q_i^{KF} exists when $T < 0$).

Detrainment of convective rain

Similar to the detrainment of cloud water and ice (see Eqs. A.30 and A.31) the detrainment of convective rain in the original KF CPS is represented by

$$\frac{\Delta q_r^{KF}}{\Delta t} = -\frac{\delta_u q_{ru}}{\Delta p} \tag{4.8}$$

where $\delta_u, \Delta p$ have their usual meanings and q_{ru} is the mean rain water mixing ratio in the updraft.

We modified Eq. (4.8) by adding a term due to the accretion of cloud droplets by raindrops. In the tropics (e.g., the warm pool region), warm rain processes occur in deep convective clouds. Autoconversion of cloud water to rain and accretion of cloud water by rain are the two dominant precipitation formation mechanisms. Recall from section A.4.4.2 that in the KF scheme all convective rain forms from autoconversion. To include the process of accretion, we added a detrainment term for accreted convective rain as:

$$\frac{\Delta q_r^{KF}}{\Delta t} = -\frac{\omega_u q_{ru}|_{acc}}{\Delta p} \tag{4.9}$$

where $\omega_u = -\frac{M_u g}{\Delta x^2}$ is the updraft vertical velocity (in pressure coordinates), M_u is the updraft mass flux and $q_{ru}|_{acc}$ is the rain mixing ratio due to accretion. The accretion term is represented by the relation given in Kong and Yau (1997).

Using (4.9), equation (4.8) is modified to become

$$\frac{\Delta q_r^{KF}}{\Delta t} = -\frac{\delta_u q_{ru}}{\Delta p} - \frac{\omega_u q_{ru}|_{acc}}{\Delta p} \tag{4.10}$$

In the present study, we assume that all accreted convective rain feeds back to the resolvable scale. Our motivation is as follows. The mass flux scheme in the KF CPS extracts moisture from a thin layer (about 150 hPa thick) above the cloud base to satisfy the closure regarding the removal of available buoyant energy in the updraft layers. This closure assumption imposes an upper limit on the convective precipitation produced by the KF scheme. Kain and Baldwin (1999), in an attempt to improve the quantitative precipitation forecasts by the KF scheme during heavy rain episodes, suggest that the convective rainfall should be supplemented by grid resolved precipitation processes. This implies the co-existence of explicit and CPS rain processes.

Once detrained, the accreted rain undergoes evaporation in a subsaturated environment as shown in Fig. A.2. Since the accreted rain originates from deep convection, it descends to the ground in the downdraft core. We assume that the accreted convective rain evaporates in a subsaturated environment by an amount that is proportional to the area of downdrafts. As will be shown in chapter 5, the accreted rain plays a dominant role in producing realistic precipitation amounts.

Modifications of other parameters

The autoconversion rate in the KF scheme is set to a new value of 0.001 (originally 0.01). This results in realistic anvil coverage during the MCS evolution due to more cloud condensate being available for detrainment at the cloud top. The radius of the updraft cores is set to 1500 m in accordance with observed values reported in Lucas *et al.* (1994).

4.2.2 Surface processes

TOGA flux formulation

Motivated by the need to obtain better estimates of surface heat balance terms over the western Pacific warm pool, Fairall *et al.* (1996b) developed the COARE 2.0 bulk flux algorithm. The algorithm was designed to reduce the total uncertainty in the surface energy budget to about 10 W m^{-2}. It incorporates the effects most pertinent to weak wind regimes (i.e., < 2 m s^{-1}). The expression for the roughness length (z_o) and the surface wind speed (V_a), used in the computation of surface fluxes, are substantially improved with the form

$$z_o = 0.011\frac{u_*^2}{g} + 0.11\frac{\gamma}{u_*} \tag{4.11}$$

$$V_a = \sqrt{u_x^2 + u_y^2 + w_g^2} \quad (4.12)$$

with $w_g = \beta w_*$, the gustiness parameter β is a constant set to 1.25 and w_* is the convective velocity scale as given in Benoit *et al.* (1989). u_x, u_y are east-west and north-south wind components at the surface. Clearly, with surface wind speeds ($\sqrt{u_x^2 + u_y^2}$) approaching zero, the convective velocity in the ABL contributes mostly to V_a and the roughness length approaches the aerodynamic smooth flow limit given by the second term in the equation for z_o.

Convective gust effects

In areas of convection, the surface sensible and latent heat fluxes are enhanced. Such enhancement is caused by increased surface wind speeds associated with the outflow from convective downdrafts and is confined mainly to the areas of the gust front. Since the KF CPS does not include cumulus momentum transports, we incorporated the gust effect of deep convection in the surface flux scheme following the manner of Jabouille *et al.* (1996).

Figure 4.7 shows the evolution of the latent and sensible heat fluxes at 2S 156E with and without gust effects in the surface flux scheme. Between 0500 - 1500 UTC sensible heat flux shows little difference while latent heat flux enhancement occurs between 1100 - 1400 UTC. The enhancement between 1600 - 1800 UTC is absent in the simulation without gust effects when fresh outbreak of convection occurs. This feature is evident in the TAO estimated latent heat flux at 2S 156E and less so for the sensible heat flux (not shown).

4.2.3 Solar radiation and clouds

Mailhot *et al.* (1998) noted problem of excessive surface evaporation (hence large

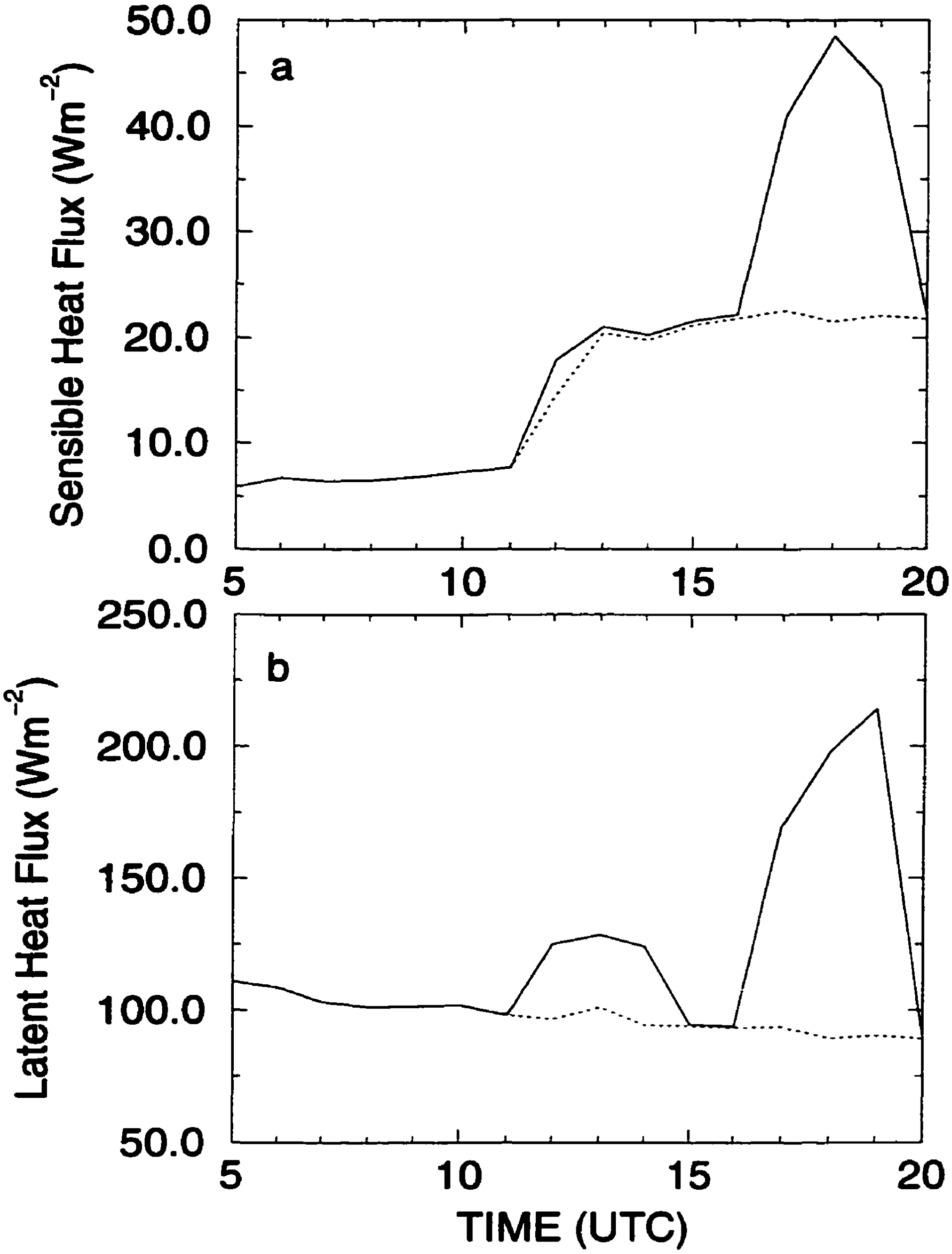

Figure 4.7: Evolution of the simulated surface fluxes at 2°S 156°E of (a) sensible heat and (b) latent heat with (solid line) and without (dashed line) convective gust effects present in the surface flux scheme.

surface latent heat flux) over land areas with the surface scheme of Benoit *et al.* (1989). This resulted in development of intense convection over islands during daytime in the model simulation, eventually leading to the formation of spurious MCSs in the model. Revision of the surface evaporation rate suggested in Mailhot *et al.* (1998) is incorporated in the present study.

Mapes and Houze (1993) reported maximum convective activity around the noon time over the islands in the western Pacific region. Daytime surface heating results in increased surface fluxes causing low-level destabilization, leading to deep convective development. With deep convection occurring over the islands, much of the incoming solar radiation is reflected, causing a slower increase of the ground temperature. However, the ground temperature prediction of Benoit *et al.* (1989) does not include the presence of implicit clouds (parameterized) which will reduce the surface solar insolation. The reduction of surface insolation in the presence of clouds is incorporated in the present study as follows.

Clouds are assumed to occur if a grid point is convectively active (implicit clouds) or if the cloud fraction is greater than zero (explicit clouds). Cloud fraction is determined based on a relative humidity criterion. When clouds are present at a grid point, solar insolation (in the atmosphere and at the surface) is switched off. This modification is likely to reduce the ground temperatures over the island areas during daytime, and alleviate the spurious MCS development downstream of islands. The impact of this modification on the evolution of the MCS under investigation is expected to be minimum because the MCS evolves mostly late in the evening and nighttime and over the water surface.

Reflection of solar radiation and ice clouds

Cloud cover in the form of cirrus clouds occurs frequently over the western Pacific region. Heymsfield *et al.* (1998) showed that cirrus clouds associated with deep convection tend to be optically thick, thereby increasing the albedo effect of these clouds on the incoming radiation. As mentioned in section A.4.3, shortwave fluxes are parameterized using the Fouquart and Bonnel (1980) scheme. The interaction of a cloud layer with the incoming solar radiation is specified in terms of cloud optical depth, the asymmetry factor and the single scattering albedo. The cloud layer reflectivity and transmissivity computed as a function of the solar zenith angle is proportional to the cloud fraction (Stephens, 1984).

Since the publication of the Fouquart and Bonnel (1980) scheme, considerable progress in parameterization of cloud optical properties for water and ice clouds have appeared (Slingo, 1989; Ebert and Curry, 1992). Ebert and Curry (1992) presented a parameterization of ice cloud optical properties based on the state of the art in-cloud observations and radiative transfer theory. The scheme yields shortwave reflectivity for ice cloud depths ranging between 0.8 - 4.7 km (or ice water path ranging from 0 to 300 g m^{-2}). Heymsfield *et al.* (1998) reported comparable cloud depths for cirrus clouds over the TOGA COARE region. For small ice crystals (effective radius r_e = 20μm), Ebert and Curry (1992) showed that shortwave reflectivity varies between 0 and 0.75 as ice water path varies from 0 to 300 g m^{-2} for a solar zenith angle of 30° (see their Fig. 3). Small ice particles have larger cross section when they are numerous and result in high reflectivity. To improve the effect of clouds on solar radiation in the Fouquart and Bonnel (1980) scheme, we set the albedo to 0.7 in the presence of ice clouds ($T < 0$ and the cloud fraction $c > 0$). This modification is expected to have minimal impact on the evolution of the MCS under investigation as it occurs in time between late afternoon and nighttime.

Chapter 5

Model verification and sensitivity study

5.1 Model verification

In this section, the results of the fine mesh run are compared against all available observations to establish the realism of the simulation. The observations include point measurements from wind profiler and the IMET flux array, airborne Doppler radar reflectivity and wind data collected during the mature stage of the MCS. Domain-averaged cloudiness and new convective areas deduced from the GMS infrared imagery are compared to those inferred from the simulation.

5.1.1 Against point measurements

The integrated sounding systems (ISS) were employed at several sites during TOGA COARE (Lin and Johnson, 1996b). Wind profiler measurements from the ISS sites are available at high temporal (every 30 minutes) and high vertical (maximum resolution about 100 m) resolution. For comparison with simulation results, wind measurements from two ISS sites (Kapingamarangi 1.1°N 154.8°E and Kavieng 2.6°S 150.8°E, see Fig. 5.3) located close to the MCS under investigation are chosen. Time-height sections of profiler horizontal wind vectors and the model wind vectors at the grid point closest to the ISS sites are shown in Figures 5.1 and 5.2.

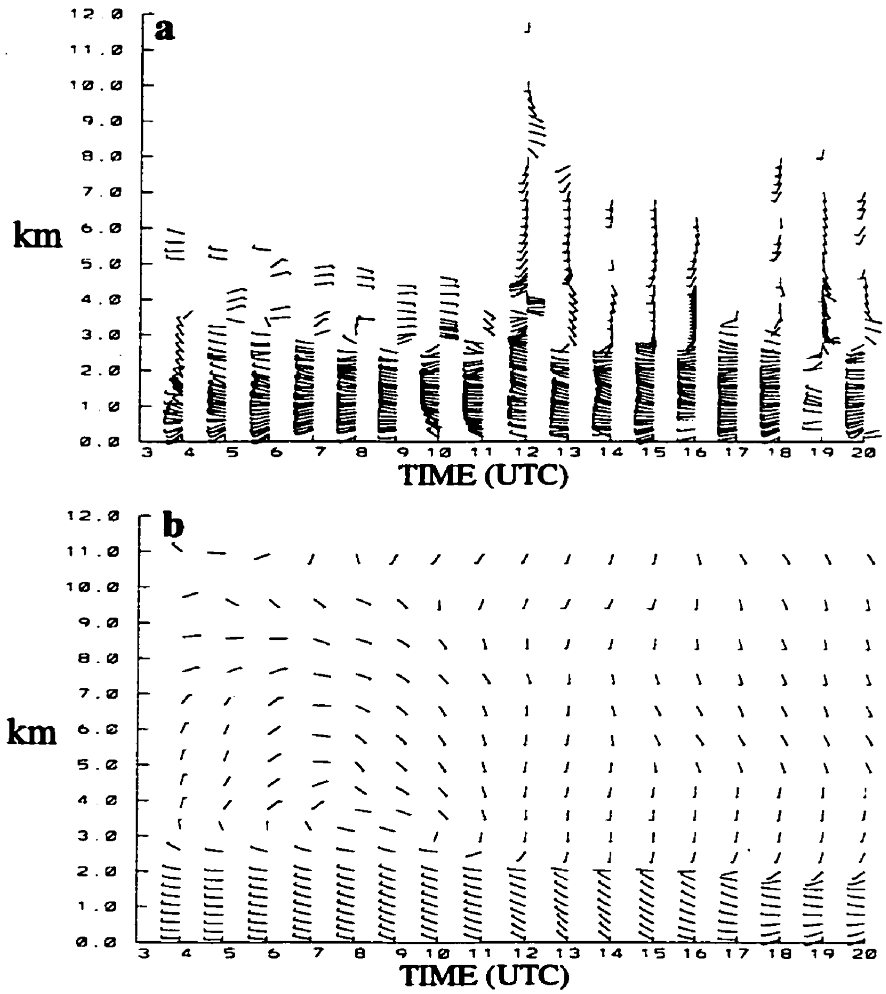

Figure 5.1: Time-height cross sections of horizontal winds from (a) wind profiler located at Kavieng (2.6°S 150.8°E) and (b) a model grid point located at 2.8°S 150.8°E. A full wind barb is 5 m s^{-1}.

In general, the time evolution of the simulated horizontal wind patterns shows good agreement with the profiler wind. The MCS of 15 December 1992 occurred about

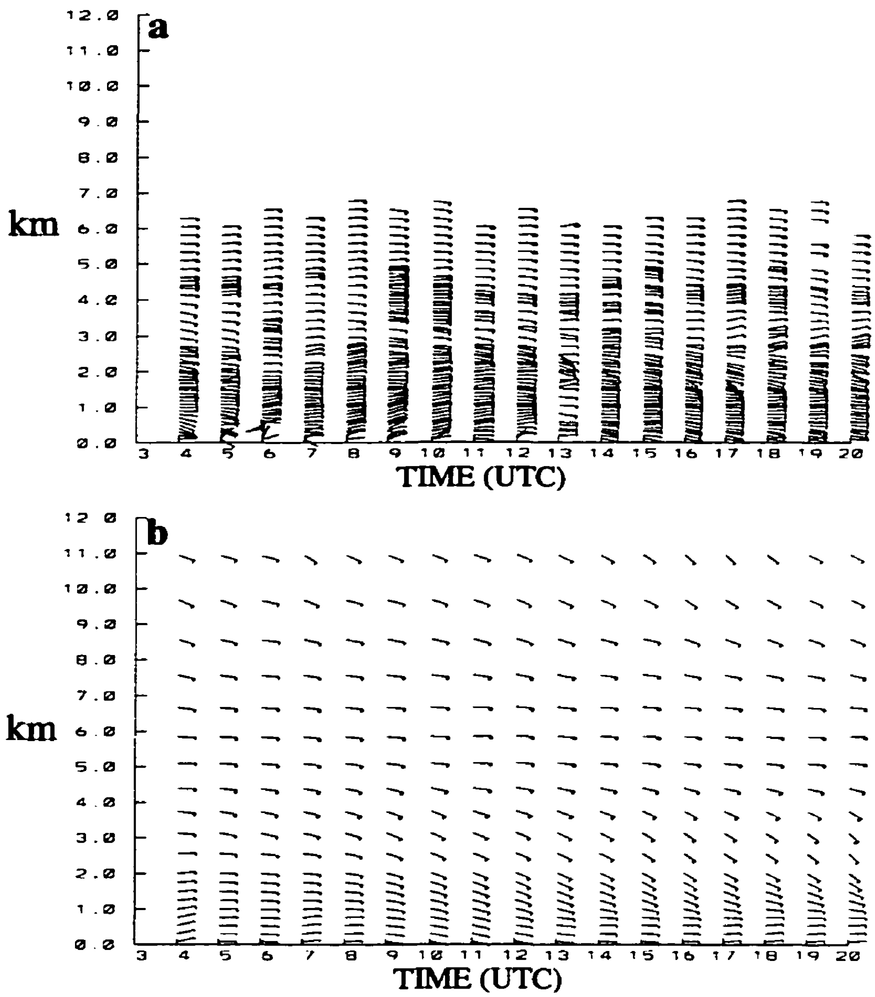

Figure 5.2: Time-height cross sections of horizontal winds from (a) wind profiler located at Kapingamarangi (1.1°N 154.8°E) and (b) a model grid point at the same location. A full wind barb is 5 m s^{-1}.

2 weeks prior to the peak WWBs. Thus low-level westerlies overlaid by easterlies appear at Kavieng (2.6°S 150.8°E). Kapingamarangi (1.1°N 154.8°E) lies just north of the equator and is in the easterly trade wind regime. Over Kavieng the depth of westerlies and the backing of the low level westerlies by roughly 180° between 0600 - 1000 UTC is well simulated by the model. Hourly streamline plots (not shown) between 0600 - 1000 UTC at 700 hPa reveal that this wind backing is caused by the westward migration of a transequatorial flow centered around Kavieng at 0400 UTC (Ramage, 1971).

One may note that the simulated wind speeds are 1-2 m s^{-1} weaker than the observed. The discrepancy is more pronounced over Kavieng at most of the levels (Fig. 5.1). The maximum wind speeds observed between 5-6 km height over Kapingamarangi is also underestimated in the simulation by about 2 m s^{-1}. Riddle *et al.* (1996) estimated the accuracy of wind profiler wind speed measurements to be about 1-2 m s^{-1}. Thus, the simulated wind speeds are considered to be reasonable.

One of the objectives of TOGA-COARE was to measure and estimate the fluxes over the warm pool at various length scales. Although point measurements yield estimates of surface latent and sensible heat fluxes, their spatial variation cannot be captured. Variability of the fluxes needs to be represented to attain realistic values in GCM studies (Jabouille *et al.*, 1996). For a mesoscale simulation to be realistic, the simulated surface fluxes of heat and moisture must be comparable to the observations. We therefore compare the simulated latent heat and sensible heat fluxes with estimated fluxes obtained using the TAO (Atlas mooring) buoy data.

Computation of sensible and latent heat fluxes is performed using the bulk flux algorithm of Fairall *et al.* (1996b). The algorithm requires the specification of sea surface temperature, the air temperature, relative humidity, wind speed and pressure at the surface as well as the heights for the measurements. Surface pressure is used in the computation of surface air density and varies little over horizontal scales (Lin

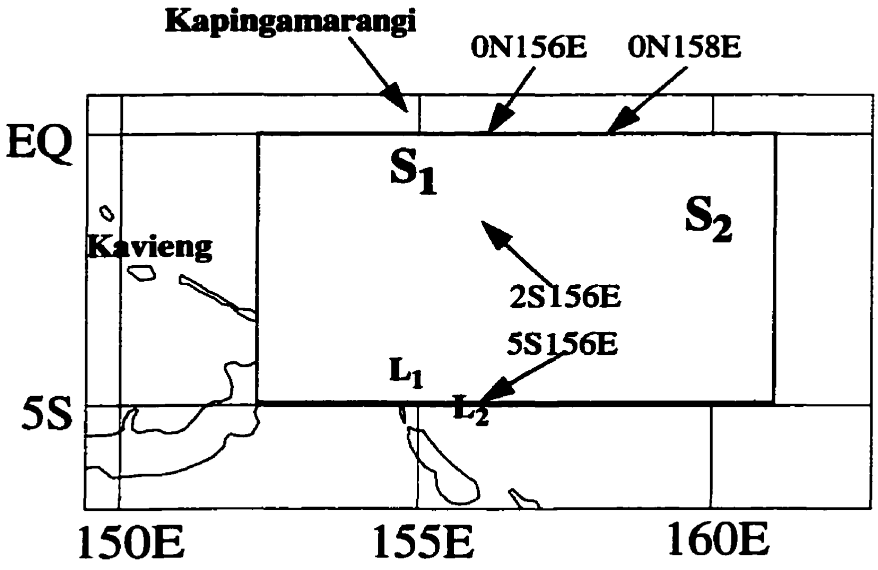

Figure 5.3: Locations of system S_1 and S_2 at 0530 UTC and the systems L_1 and L_2 observed during the mature stage of the MCS. The locations of the 4 TAO buoys used to estimate the surface fluxes of latent and sensible heat are indicated. The shaded region depicts the area over which domain averaging is performed. The ISS wind profiler sites are also indicated.

and Johnson, 1996b). All variables were available from the TAO buoy data except for surface pressure, which is set to the value measured by the IMET buoy system (2°S 156°E). The TAO data situated closest to the MCS were those at 0N156E, 0N158E, 2S156E and 5S156E (Fig. 5.3). The hourly data from these four buoys were input to the bulk flux algorithm to obtain sensible and latent heat fluxes. The TAO buoy at 2S156E was close to the IMET buoy which measured the surface fluxes. The estimated fluxes using the bulk flux algorithm closely match the IMET fluxes (not shown). Thus, we will use the estimated fluxes from TAO buoys for intercomparison.

Flux values at a model grid point represent grid box averages. Since the hourly temperature, sea surface temperature and relative humidity data from the TAO moorings are hourly averages (Mangum *et al.*, 1994), the estimated flux values can be thought of as a line average over a distance of approximately 20 km. Ideally, it would be best to compare flux values at a model grid point with area averages from measurements.

Figures 5.4-5.5 compare the time variation of sensible and latent heat fluxes between the simulation and the TAO data. All grid point values are shifted by 2-3 grid points in the N-S and/or E-W directions. This shift is necessary to account for the differences in the location of deep convection between the model and the observations. Over the duration of the simulation (0500 - 2000 UTC) there is fair agreement between simulated and observed fluxes at the 4 locations indicated. Although the variation of the fluxes with time is similar, there is an apparent delay of 1-1$\frac{1}{2}$ h (peaks shifted to the right), indicating the late onset of deep convection in the model. Sharp increases in both latent and sensible heat fluxes are observed at 0900 and 1500 UTC (2S156E), 1200 UTC (5S156E), 1300 and 1700 UTC (0N156E), and 0900 and 1900 UTC (0N158E), with the exception of sensible heat flux at 1500 UTC (2S156E) where a small rise occurs in the measurements. Sharp increases are adequately captured by the model at 2S156E, 0N158E, and at 1300 UTC at 0N156E. Our simulation indicates that such increases in sensible heat flux result from the combined stronger surface

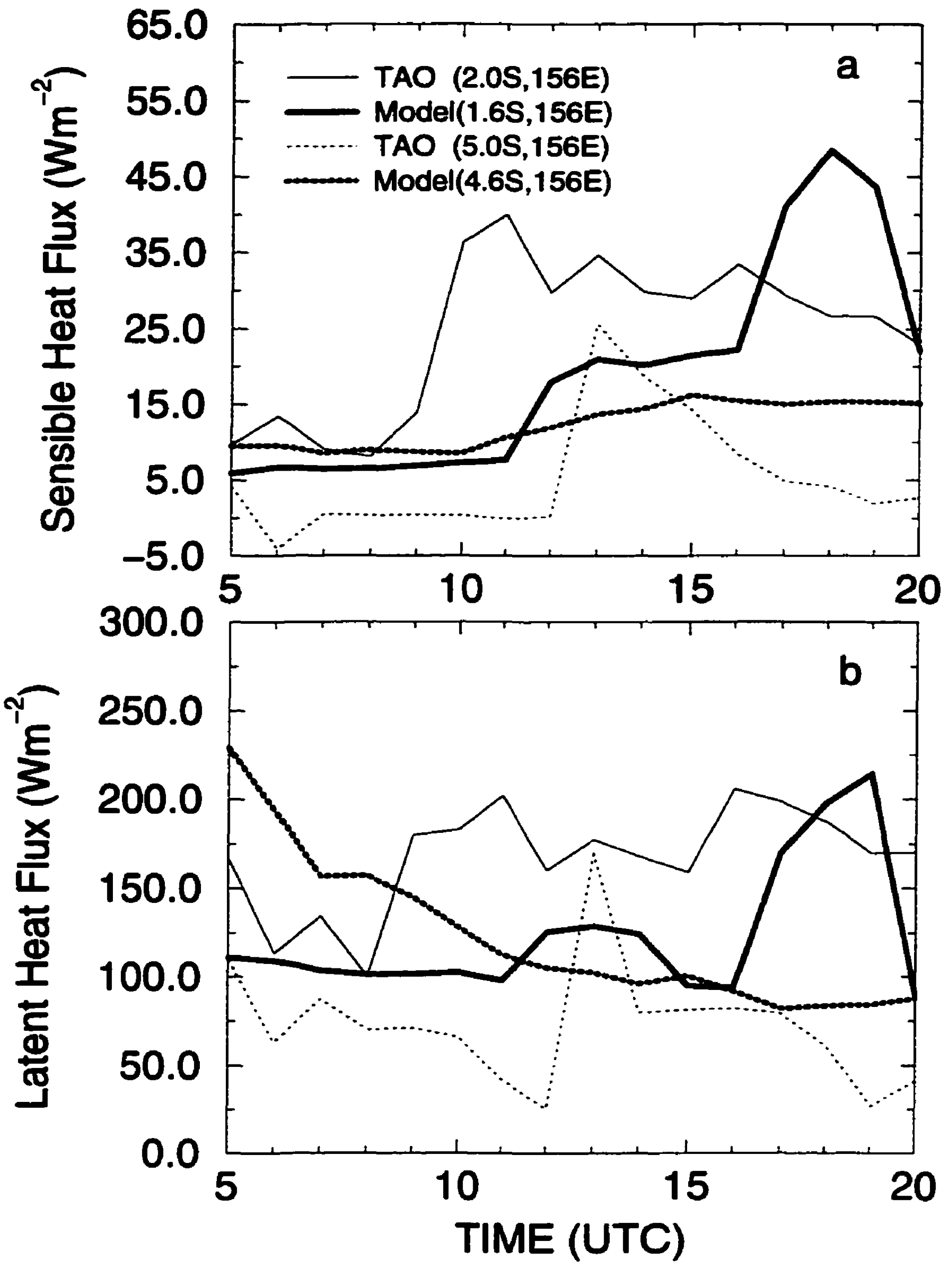

Figure 5.4: Surface fluxes of (a) sensible heat and (b) latent heat at the two locations indicated (Fig. 5.3). Thin lines (solid and dashed) refer to the estimated fluxes obtained from the TAO data. Thick lines (solid and dashed) refer to corresponding simulated fluxes.

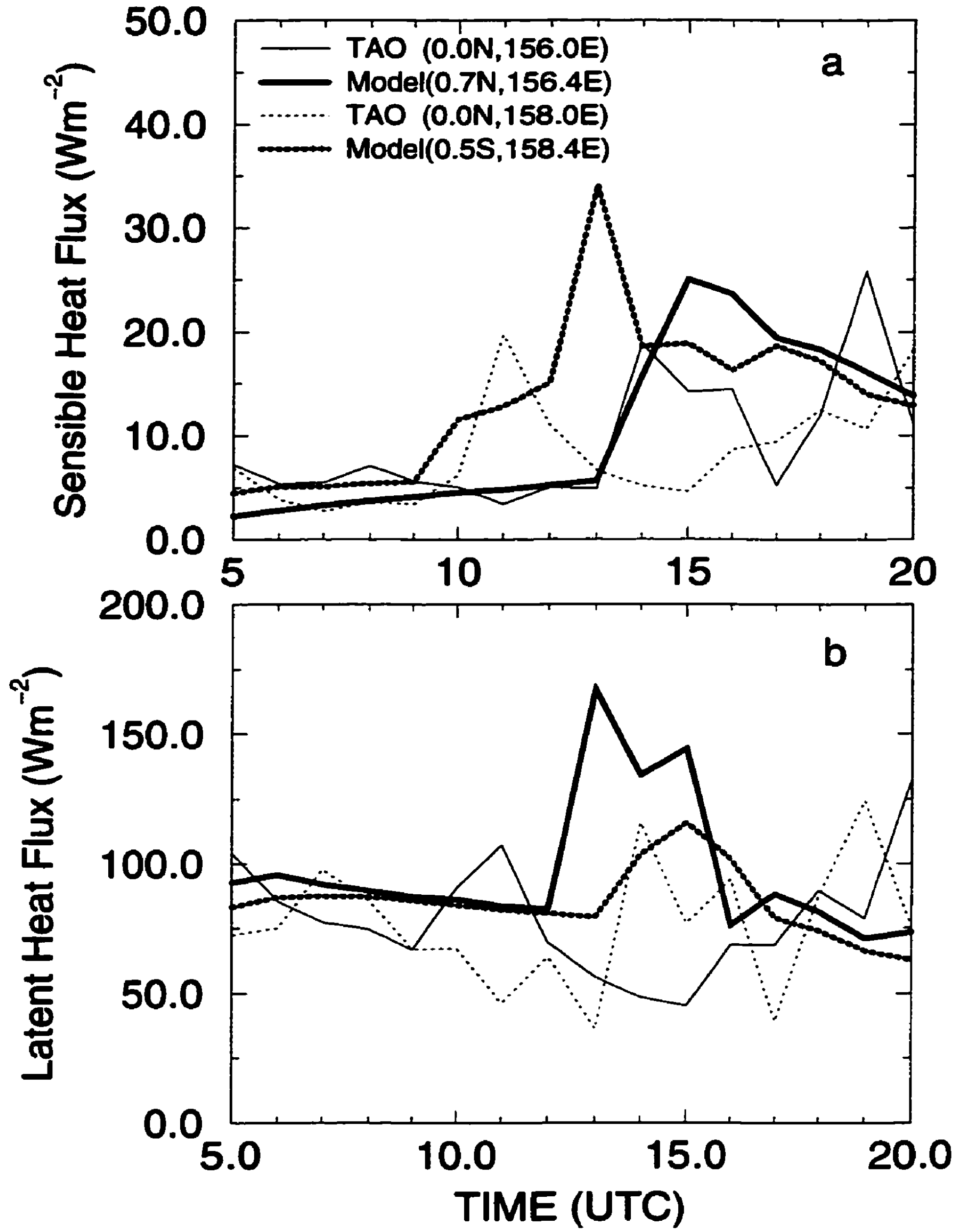

Figure 5.5: As in Fig. 5.4 but for the second pair of stations.

winds and colder surface air temperature associated with convective downdrafts. The increases in latent heat flux occur primarily due to the enhanced surface winds by the downdrafts with surface drying playing a small role (Jabouille *et al.*, 1996). Jabouille *et al.* (1996) reported enhancements of two times for latent heat flux and three times for the sensible flux in areas of deep convection. This is confirmed by the present simulation.

The rapid enhancement in the TAO sensible and latent heat fluxes at 5S156E near 1300 UTC appears to be due to short-lived deep convection. Such small-scale deep convection cannot be captured by the model using the grid size of 20 km. Similarly for 0N156E, only the increase in sensible and latent heat flux at 1300 UTC is captured by the simulation. From TAO-estimated fluxes, deep convection appeared to occur in 2 spells; one between 1300 - 1700 UTC and a short-lived event between 1800 - 1900 UTC. The second event is missed by the simulation but the dissipation of the first event yields a decrease in the fluxes between 1400 - 2000 UTC. Since the second event is short-lived and obviously of small scale, it could not be resolved by the coarse horizontal resolution employed in the model.

In summary, comparisons of the temporal variation of surface fluxes between the simulation and observation are reasonable. During convective periods, the simulated sensible heat flux is enhanced by a factor of three while the simulated latent heat flux is enhanced by a factor of two, confirming results from the study of Jabouille *et al.* (1996). Increase in sensible heat flux arises due to the combined effects of downdrafts cooling and increased surface wind speed associated with the gust front. Increase in the latent heat flux is associated with the drying effects of convective downdrafts and the increase in surface winds associated with gust fronts. In order to obtain realistic increases in latent heat fluxes during convective periods, the convectively generated gust effects need to be incorporated in the surface flux formulation (section 4.2.2). This suggests the necessity of parameterizing of momentum fluxes by cumulus convection to obtain realistic surface wind enhancements due to convective downdrafts.

5.1.2 Against satellite measurements

The hourly GMS infrared imagery available at high spatial resolution ($\approx$ 5 km) is used to validate qualitatively the evolution of the MCS during its growing stage between 0600 - 1700 UTC. Recall that during this stage, the MCS initiates as two subsystems, each undergoes individual development and then merges to form an extensive anvil cloud cover. The anvil cloud cover is seen to increase with time and attains a steady state value during the mature stage (between 1700 - 2000 UTC). Since the source of anvil cloud is deep convection, the cloud coverage gives a reasonable indication of the spread of convective activity over the region (shaded in Fig. 5.3). To ascertain the evolution of the MCS during its growing stage more objectively, the spatial distribution of new convection (or areas where convection has just onset), derived from the GMS imagery, will be compared to the simulated new convection areas.

5.1.2.1 Percentage anvil cloud coverage

Tollerud and Esbensen (1985) classified GATE cloud clusters into different stages (growing, mature and dissipating) on the basis of anvil cloud coverage. An anvil cloud was defined as present whenever the cloud fraction was greater than zero in a layer above 300 hPa. Thus, we choose the temperature at 300 hPa, which is about -30°C or 243 K, as the threshold temperature for defining the presence of an anvil cloud (Fig. 14 in Kain and Fritsch, 1990). That is, wherever the brightness temperature is less than 243 K, an anvil cloud is assumed to be present. For the model simulation, we assume that an anvil cloud occurs when the ice mixing ratio $q_i \geq 0.005$ g kg^{-1} in the 300 - 100 hPa layer. This choice for the layer is consistent with that used by Tollerud and Esbensen (1985). For the threshold value, we noted that ice mixing ratio measured by McFarquhar and Heymsfield (1996, 1997) in tropical cirrus clouds varies with temperature and horizontal scale. The values for ice mixing ratio range from 10^{-1} g kg^{-1} to 10^{-3} g kg^{-1} as temperature changed from -30°C to -70°C. This suggests an average value for q_i in tropical cirrus clouds to be 5×10^{-2} g kg^{-1}. They also noted substantial horizontal variability in q_i with its peak near deep convective cores and a rapid decrease (nearly an order of magnitude) away from the convective cores. This variability occurs on a horizontal scale of less than 100 km. Since over a grid box of 20 km the area occupied by deep convection is relatively small, we estimate the threshold ice mixing ratio associated with cirrus clouds to be about 5×10^{-3} g kg^{-1}.

Figure 5.6 shows the percentage anvil cloudiness over the domain (shaded in Fig. 5.3) as a function of time. It takes about 2 - 3 hours for the model to generate a reasonable amount of ice cloud content. Rapid rise in the coverage occurs between 0900 - 1400 UTC, when the MCS exhibits considerable areal expansion. An almost steady state appears between 1700 - 2000 UTC (i.e., at the mature stage) when the cloud coverage is maximized. Since the modeled anvil clouds is generated by ice detrainment from the KF CPS, the general agreement with GMS derived anvil coverage indicates a realistic evolution of the MCS in the model simulation. The evolution of the simulated MCS during its growing stage will be verified in more detail in the next section against the GMS imagery.

5.1.2.2 Spatial distribution of new convection

Sherwood and Wahrlich (1999) used time series of cloud fraction to determine convective onsets from GMS infrared satellite data. The cloud fraction (C_{208}) was defined as the ratio of the cloudy area with brightness temperature $T_b < 208$ K to the area of a square box 120 km on a side. A convective onset is defined to occur when $C_{208} > 0.05$ at time t but not at any other time within the previous 3 h in the satellite data. A model-simulated convective onset is defined to occur when the total rain rate exceeds 3 mm h^{-1} for the first time within the previous 3 h over at least 5% of a 120 km size box centered over a grid point. The choice of 3 mm h^{-1} as the threshold rain

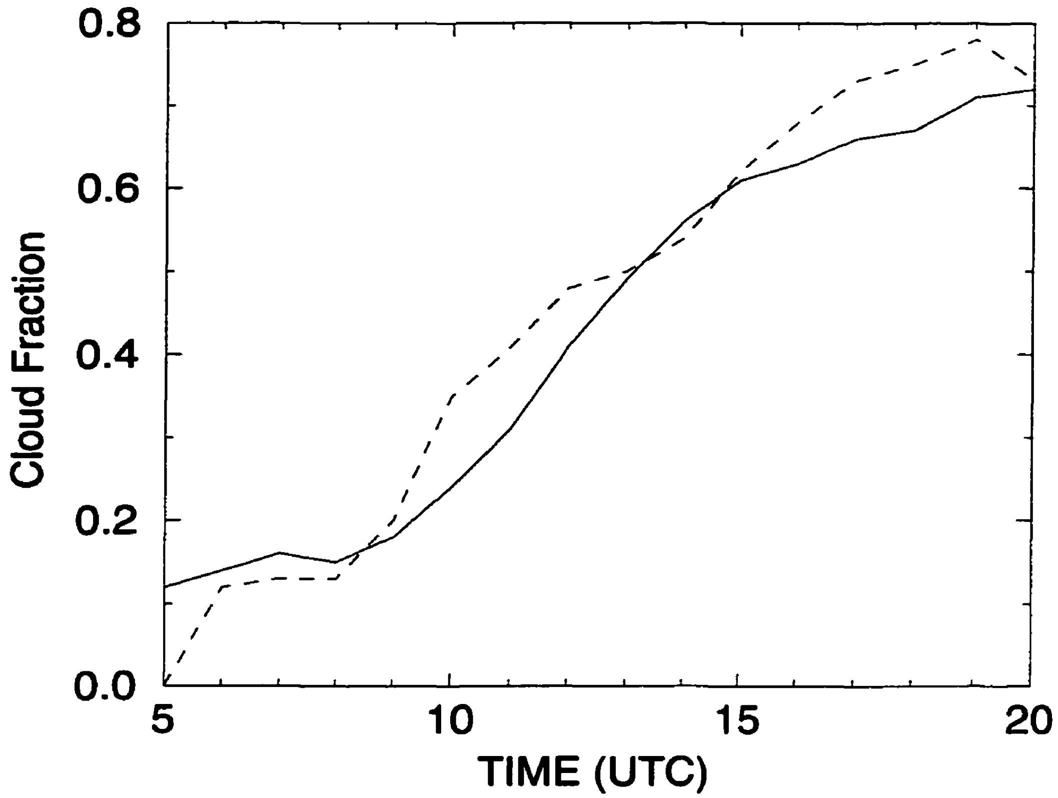

Figure 5.6: Evolution of the fractional anvil cloud cover over the domain (shaded in Fig. 5.3) from hourly GMS infrared imagery (solid) and from hourly model simulation (dashed).

rate is motivated by the infrared brightness temperature versus rain rate relationship suggested by Sheu *et al.* (1996). In that study a mean rain rate of 3 mm h^{-1} is associated with cloud top temperatures of 208 K. This rain rate is also consistent with that used by Nuret and Chong (1998) in their study of moisture budget of an MCS over the warm pool.

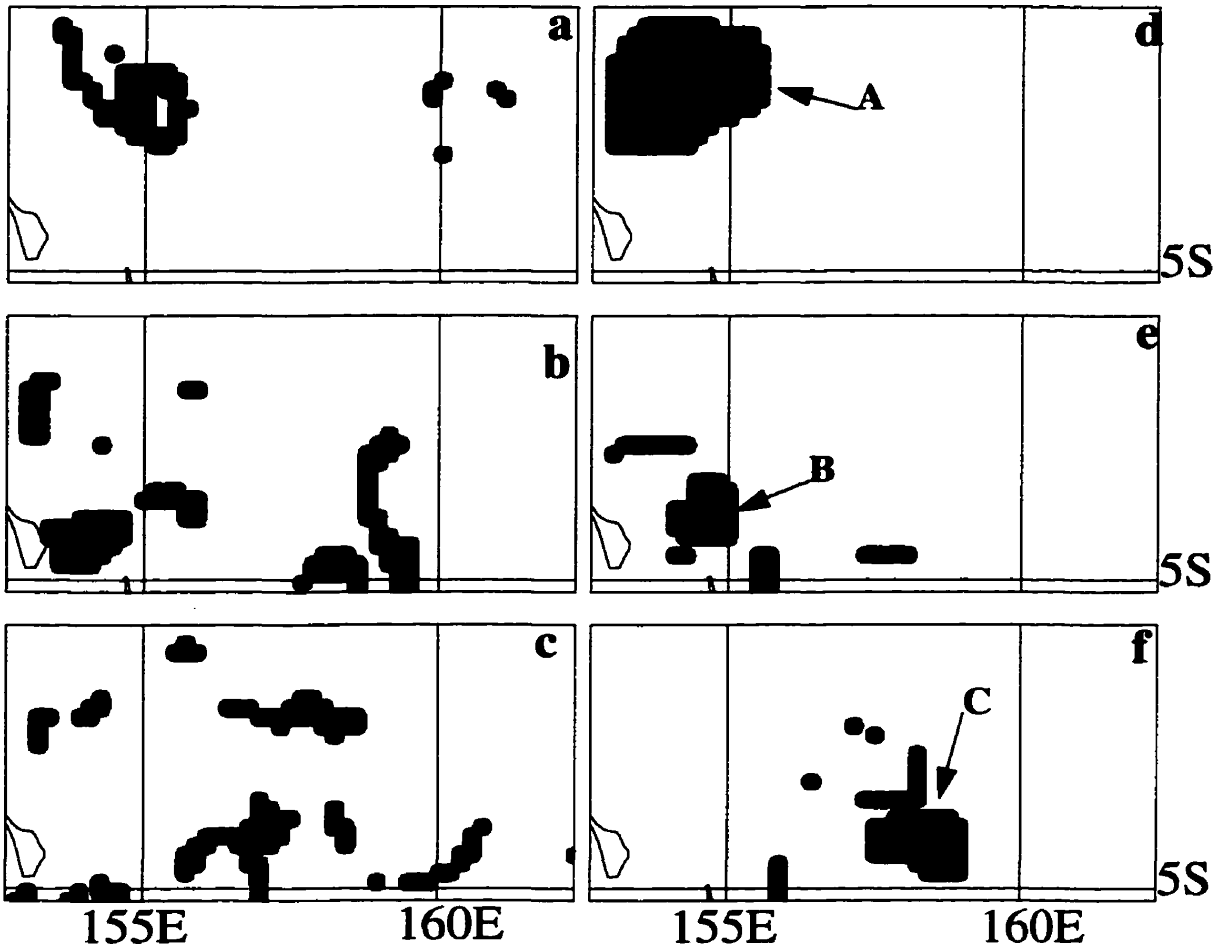

Figure 5.7: New convective onset areas shown by shaded regions for 0730, 1130 and 1430 UTC from GMS infrared imagery (a-c) and for 0600, 1100 and 1400 UTC from model simulation (d-f).

Figure 5.7 compares convective onset areas between the satellite-derived and the modeled precipitation. These areas depict qualitatively the overall evolution of deep convection during the growing stage of the MCS. The simulated patterns of convective onset at 0600 UTC agree reasonably well with the observed. However, simulated onset areas at 1100 UTC fail to capture the southern portion of the S_2 system partly due to the lack of observations in this area in the model initial conditions. Nevertheless, the spatially more expansive system S_1 is in close agreement with observations at all three times shown. The growing stage is marked by three convective onsets over three different regions, located respectively over the areas A(0600 UTC), B(1100 UTC) and C(1400 UTC see Fig. 5.7). These 3 convective onsets are responsible for the merger of the anvil that leads to a spatially extended cold cloud shield during the mature stage. The onset of deep convection in the 3 different regions between 0600 - 1400 UTC is adequately captured by the simulation. Convective onset in the model is governed by the convective trigger function criteria. The factors responsible for the three onsets will be discussed in chapter 6.

5.1.3 Against radar measurements

Airborne Doppler radar measurements by two NOAA P3 aircraft were carried out within this disturbance from 1700 - 2100 UTC during which time the MCS was at the mature stage, as mentioned in Chapter 2. Protat *et al.* (1996, 1998) analyzed the Doppler radar winds and reflectivity fields over a mesoscale domain (M) given in Fig. 3.1. Between 1700 - 2045 UTC, Protat *et al.* (1996) noted the existence of two convective systems L_1 and L_2 over the mesoscale domain located in the western and eastern part of the domain, respectively. They consist of stratiform or weakly convective precipitation (less developed for L_2) in their north-western part. A narrow region of strong precipitation, oriented in a north-east to south-west direction, is located ahead of the stratiform area and lies to its southeast. A transition region, characterized by weak reflectivities, is also observed at the rear of the convective lines of the L_1 and L_2 systems. This 3-hour mesoscale analysis gives an overall description of the MCS at its mature stage.

To facilitate an intercomparison of the simulated mesoscale structures with those reported by Protat *et al.* (1998), the high horizontal resolution (5 km) radar data were coarsened to a horizontal resolution of 20 km. While horizontal resolution compatibility is achieved easily, it is difficult to mimic the sampling strategy used by the airborne Doppler measurements. The system L_1 was sampled between 1700 - 1830 UTC by the aircraft and the system L_2 was sampled between 1915 - 2045 UTC. The maximum range of the radar is 76.8 km making it difficult to sample large areas of the MCS at the same time (Protat, 1999). The modeled total precipitation rate is converted to radar reflectivity using the relation $Z = 323\ R^{1.43}$ as suggested by Short *et al.* (1997). Figure 5.8 compares the simulated reflectivity and wind field at 500 m at 1800 UTC. Note the rotation of the two domains differ by 15 degrees. This added rotation accounts for the more EW alignment of the simulated L_1 and L_2 against the NE-SW alignment observed by the radar.

The simulation captures the overall features found in the radar observations: two convective systems with weak reflectivities to their north-west particularly the orientation of the linear shaped intense precipitation associated with system L_1. The simulated magnitude for L_1 lies between 35 - 40 dBz, while the observed values are 40 - 45 dBz. While the system L_2 is simulated, the strong precipitation coverage is less conspicuous. The wind fields at 500 m height retrieved from the Doppler radar data and model simulation show large differences with the maximum magnitude differing by a factor of two. The lack of parameterization of momentum transport can account for the weaker simulated wind speeds. LeMone *et al.* (1998) suggested the buildup of low-level vertical shear due to enhanced low-level wind speeds associated with convective momentum transport. Bearing in mind that the objective of this study is to simulate the mesoscale features associated with the MCS, the agreement between the simulated and observed radar reflectivity is deemed reasonable given the higher resolution of radar measurements and the coarse horizontal resolution of the simulation.

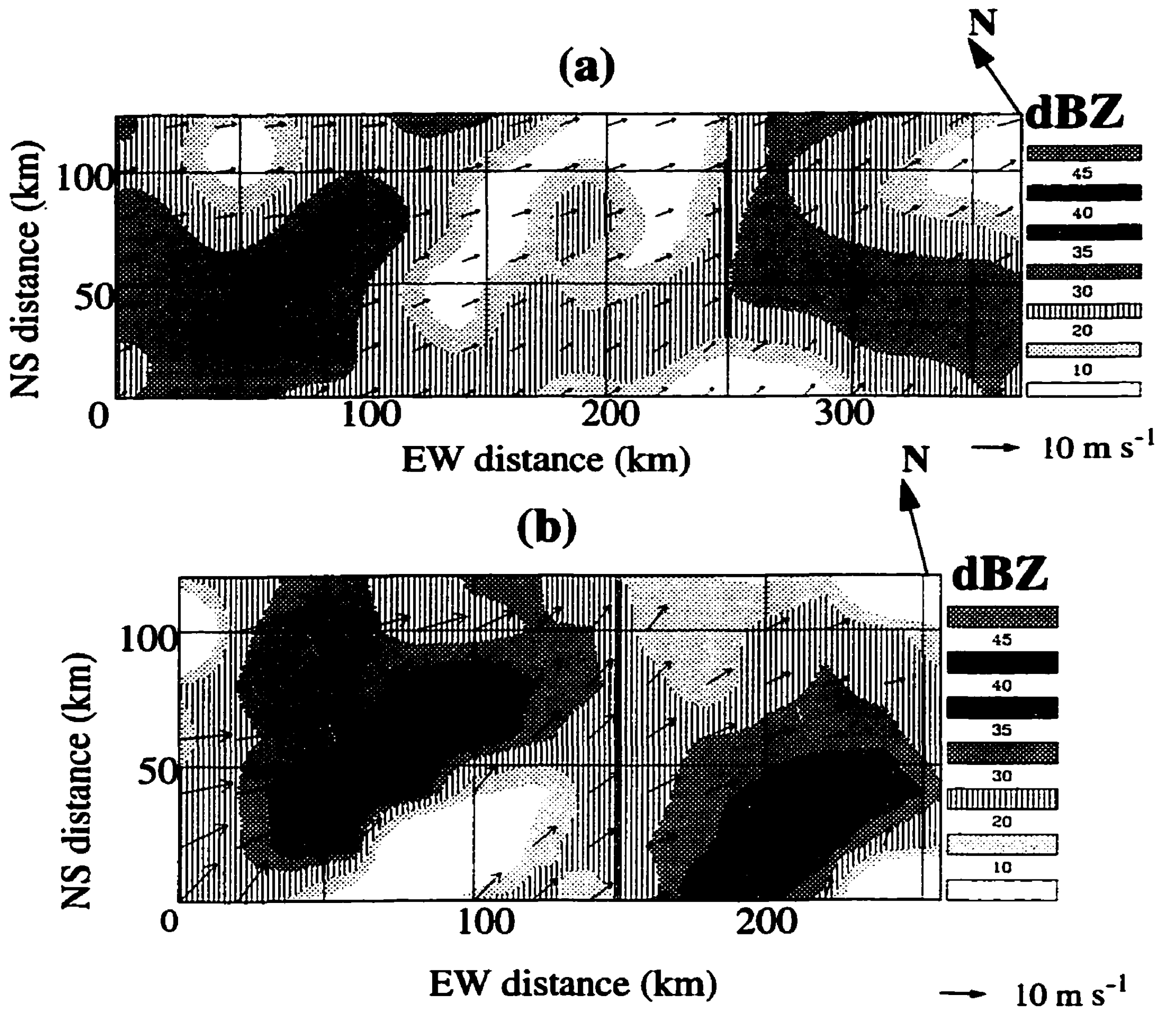

Figure 5.8: (a) Model simulated reflectivity at 1800 UTC along with horizontal winds at 500 m height. (b) Horizontal reflectivity and retrieved Doppler radar winds for the period between 1700 - 2045 UTC at 500 m height obtained from a mesoscale analysis of Protat *et al.* (1998). True north for both the domains are indicated as 'N'. The lower left corner of the domain in (a) and (b) are located at 4.45°S 154.49°E and 4.28°S 154.59°E respectively.

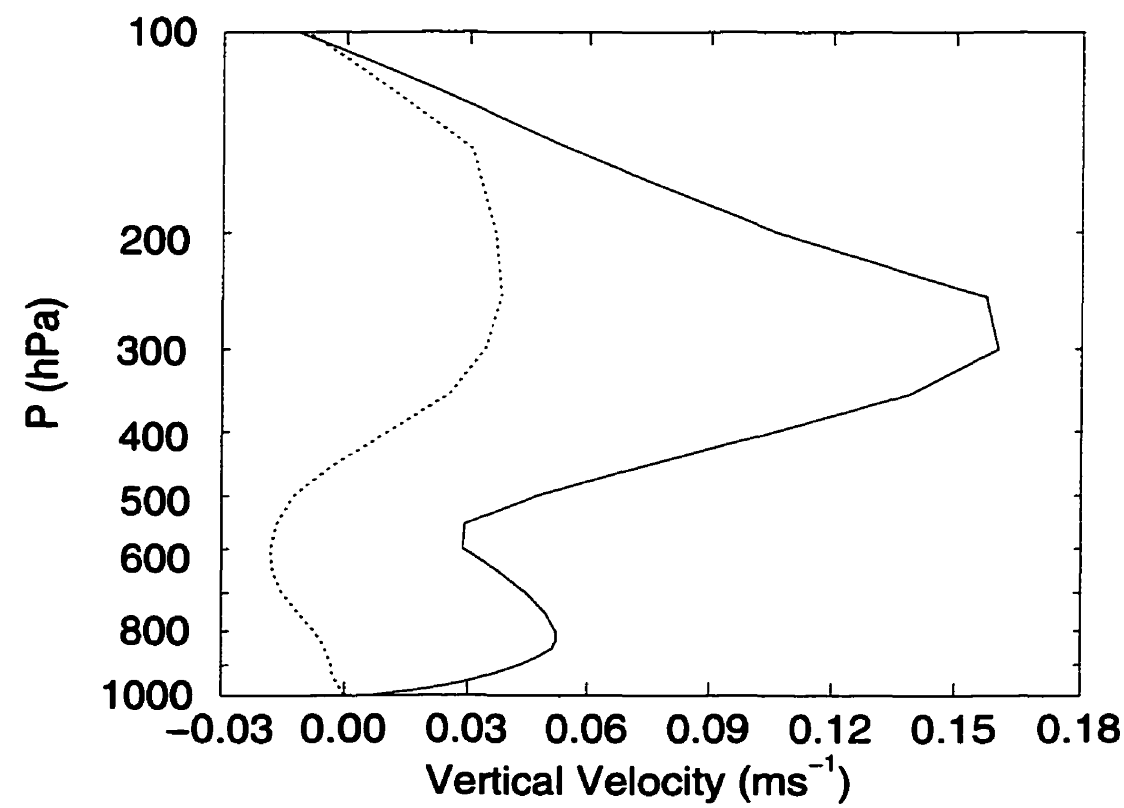

Figure 5.9: Domain-averaged vertical velocity profiles in convective (solid) and stratiform (dashed) regions associated with the systems shown in Fig. 5.8. Convective region is defined by Z > 35 dBz and stratiform region is defined by Z < 30 dBz in Fig. 5.8.

The average vertical motion associated with the deep convective and stratiform precipitation is shown in Fig. 5.9. We assume a simulated reflectivity greater than 35 dBz (less than 30 dBz) as representative of deep convection (stratiform precipitation). The deep convective regions exhibit two maxima consistent with the KF scheme parameterized heating profile for tropical soundings (Kain and Fritsch, 1990). The stratiform precipitation regions exhibit mesoscale subsidence below the freezing level and ascent above. Protat *et al.* (1997) retrieved vertical profiles of horizontal divergence from the Doppler radar 'purl' measurements. Each purl was approximately 5 km in radius and was mostly confined to stratiform regions of the systems. The vertical motion profile indicated subsidence below the 0°C level with mesoscale updrafts above. The peak mesoscale updrafts were located at about 8 km height. The peak vertical motions were -10 cm s^{-1} for the subsidence and 20 - 30 cm s^{-1} for the mesoscale updrafts. The simulated values are one order of magnitude smaller, because of the averaging process and the coarse horizontal resolution of 20 km used in the simulation compared to the 5 km mean radius for the purls used in the aircraft measurements.

We shall briefly explore the mechanisms responsible for the observed structure of the MCS during the mature stage (1700 - 2000 UTC). The 900 hPa streamlines at 1800 UTC along with the locations of the systems L_1 and L_2 are shown in Fig. 5.10. The convective lines L_1 and L_2 seen in the control simulation (Fig. 5.8a) are located in a region of favorable surface potential temperature dropoff (SPTD) and CAPE since 0800 UTC (Fig. 6.2b). These systems occur in two separate confluence zones. One of them is located south of the center of the transequatorial flow and the other one is formed in a region of southerlies and southwesterlies between 5-6°S 156-158°E (Fig. 5.10).

A comparison of the moist CONTROL and DRY simulation shows that the system L_1 observed in the temporal composite radar reflectivity fields is due to mesoscale circulations induced by deep convection. The vertical motion field between 1000

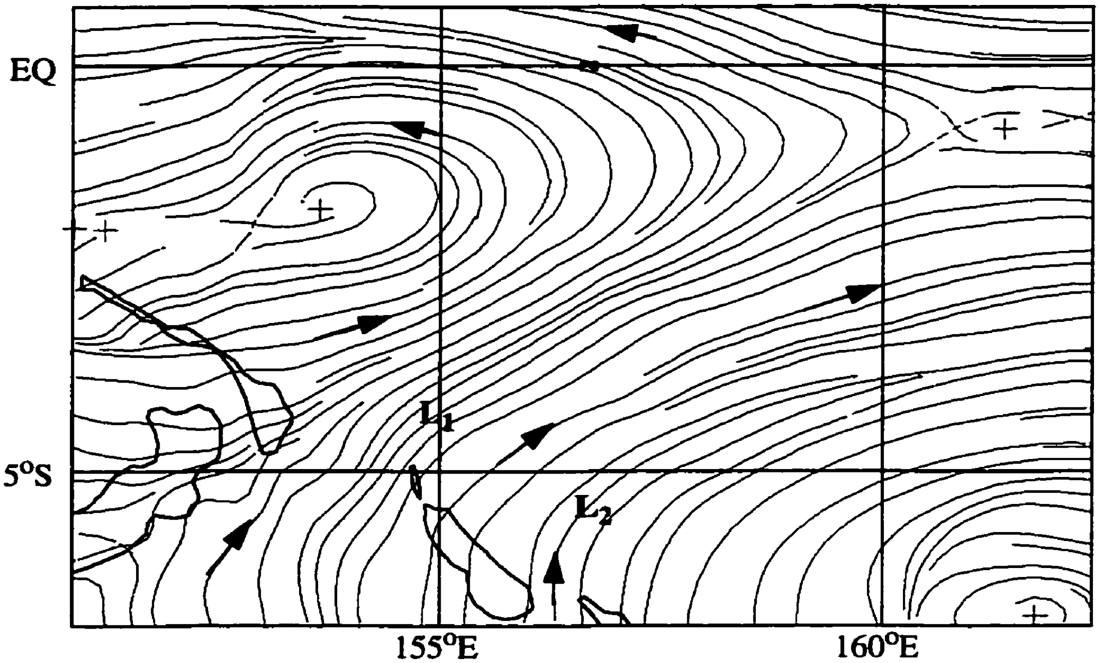

Figure 5.10: The 900 hPa model streamlines at 1800 UTC, with the locations of the convective systems L_1 and L_2 (Fig. 5.8a) during the mature stage of the MCS (1700 - 2000 UTC) indicated. The systems L_1 and L_2 form in two different confluence zones.

UTC and 1600 UTC is downward in the region occupied by L_1 due to the presence of two convective systems north and south of it. A north-south vertical cross section of the vertical velocity through the system L_1 at 1200 UTC is shown in figure 5.11. The occurrence of vertical motion throughout the troposphere to the north and south of L_1 suggests the existence of two convective systems. The compensational subsidence from these two systems maintain subsidence over the region of L_1 precluding its onset at 1200 UTC. The subsidence over the region persists upto 1600 UTC (not shown) when the two systems weaken leading to the formation of convective system L_1.

In summary, the simulated reflectivity matches reasonably the radar reflectivity taken during the mature stage of the MCS. The convective system L_1 is adequately simulated (orientation of the line of maximum precipitation and its intensity). The convective system L_2 is less well captured by the simulation. The simulated wind speeds at 500 m are weaker by a factor of two, indicating the need to parameterize the convective momentum transport process in the model. The profiles of vertical motion in the stratiform regions is consistent with the observed profiles reported by Protat *et al.* (1997). In convective regions, the vertical motion is consistent with the parameterized convective heating profile obtained by Kain and Fritsch (1990) for tropical soundings. Thus, the simulation captures realistically the observed salient features of the MCS during its mature stage. Also during the mature stage, the systems L_1 and L_2 occur in two different confluence zones. A comparison of the DRY and CONTROL simulation reveals that the spatial distribution of precipitation associated with the system L_1 at the mature stage arises due to the large scale vertical motion being driven by mesoscale circulation associated with deep convection in the vicinity. The convective line L_2 forms in the confluence zone between low level southwesterlies and southerlies.

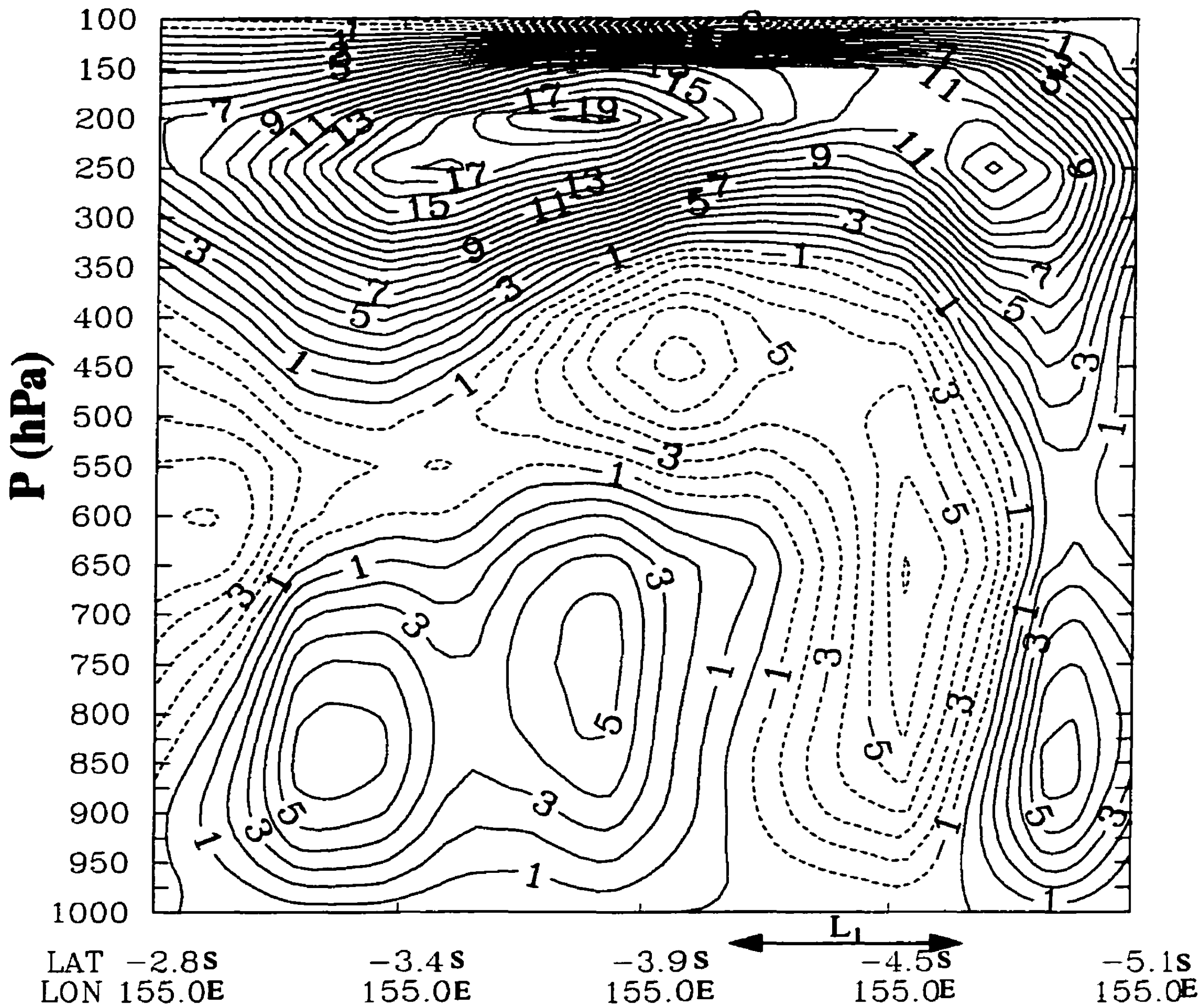

Figure 5.11: A north-south cross section of the vertical motion field (10^{-2} m s^{-1}) at 1200 UTC. The region occupied by the convective line L_1 (see Fig. 5.10) is also shown.

5.2 Sensitivity to convective trigger function

Deep convection is widespread and occurs at many length scales over the western Pacific warm pool region. Forecasting of deep convection for the tropical Pacific region remains a challenging task for meteorologists. The use of traditional stability indices, such as CAPE and the lifted index, often provides little indication about the occurrence of deep convection in these regions (Kodama and Businger, 1998). In fact, the mesoscale mean CAPE sufficient for deep convection exists almost 90% of the time over the warm pool region (Sherwood, 1999). Since the convective initiation in mesoscale models determines the success of a numerical simulation, predictability of deep convection over the warm pool remains a challenge. Previous meso-β scale modeling studies have demonstrated the importance of initial conditions and model physics in the success of simulations. For example, Zhang *et al.* (1988) suggested the use of appropriate combination of implicit and explicit condensation schemes to allow for a more realistic interaction among the various microphysical processes. Studies of Kain and Fritsch (1990) and Stensrud and Fritsch (1994) showed that some numerical simulations are sensitive to convective initiation mechanisms used in mesoscale models. The latter also highlighted the importance of including mesoscale features (moist tongues, cold pools etc,) in the initial conditions to obtain a successful simulation. Refinements to the Fritsch and Chappell (1980) convective trigger function were reported in Rogers and Fritsch (1996). Addition of surface inhomogeneities to the trigger function offered a greater potential to successfully simulate MCSs in a variety of environments. Occurrence of deep convection in mesoscale models depends on initial moisture and temperature fields, the presence of appropriate convective initiation mechanisms and a favorable large scale (grid scale) divergence field. Despite considerable progress in the observations over the continental United States, inferring the correct timing and location of deep convection from resolved scale variables continues to be a challenging task (Rogers and Fritsch, 1996).

In this section, we will examine the sensitivity of the simulated MCS to the convective trigger function. As discussed in section 4.2.1 the trigger function in the KF scheme was improved by assuming a deep column ascent and a threshold value for the surface potential temperature dropoff (see Fig. 4.6, chapter 4). Three numerical experiments, as given in Table 5.1, using various combinations of the original KFT function and the two new criteria are performed

Experiment Index	Remarks
KFT	Original KFT function
KFTW	Original KFT function and deep column ascent
KFTSPTD	Original KFT function and SPTD
CONTROL	Original KFT, deep column ascent and SPTD

Table 5.1: Sensitivity experiments performed with various combinations of the KFT function.

Figure 5.12 shows the time evolution of cloud fraction over the domain (shaded in Fig. 5.3). Experiments KFT and KFTW exhibit a sinusoidal behavior of cloud fraction with time. Recall that the simulated anvil clouds are largely due to detrainment of ice particles from deep convection. This suggests a surge of wide spread deep convective activity during the first few hours resulting in the consumption of CAPE. The surge is followed by a period of little deep convective activity with a minimum during 1300 - 1400 UTC. It appears that the ABL recovers through the deposition of surface fluxes and takes on the order of 12 hours, a result consistent with the Raymond (1995) quasi-equilibrium ABL hypothesis. After the recovery of the ABL, another round of deep convection becomes possible. The cloud fraction in the KFT experiment is larger than that in the KFTW experiment, due to the added stringency in the KFTW experiment by incorporating the criterion of deep column

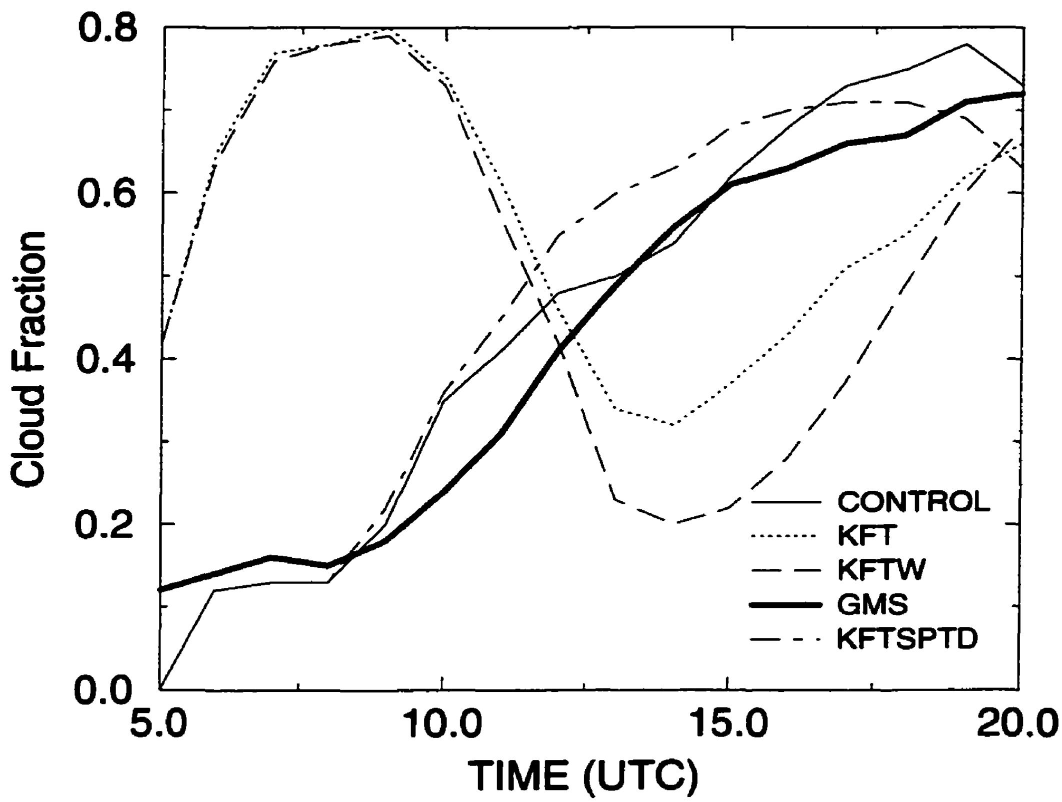

Figure 5.12: Time evolution of the fractional cloud cover over the domain (shaded in Fig. 5.3) for different sensitivity experiments associated with convective trigger function. The thick solid line denotes the fractional cloud cover computed from GMS satellite data.

ascent. The results of the KFT experiment suggest that long-term model integrations starting from the ECMWF analysis and the Kain-Fritsch CPS tend to exhibit such sinusoidal temporal behaviors of deep convection over some regions.

The evolution of the cloud fraction in Experiment KFTSPTD and CONTROL shows similar behavior. For instance, the peak cloud fraction in KFTSPTD occurs around 1600 UTC compared to 1900 UTC in CONTROL. As expected, the cloud fraction is larger in KFTSPTD due to the absence of the deep column ascent criterion. As a result, the mature stage lasts from 1400 to 1900 UTC, in contrast to CONTROL which lasts from 1700 to 2000 UTC. Thus, the original KFT function, complemented by the deep column ascent and SPTD criteria, is responsible for the successful simulation of the lifecycle of the MCS. The SPTD has the biggest impact on the simulation of the lifecycle with the deep column ascent acting to reduce the amount of convective activity during the growing stage to yield a better timing for the onset of the mature stage.

The temporal evolution of the cloud fraction in the KFT and KFTW experiments are unrealistic. Model simulations show widespread convective activity during the first 5 hours over S_1 and S_2, followed by decay and a minimum in convection by 1400 UTC (not shown). The spatial distribution of deep convection during the growing stage of the MCS for CONTROL and KFTSPTD is shown in Fig. 5.13. Small differences in the spatial distribution are evident with the areal spread of convection being relatively larger in the KFTSPTD experiment.

The differences become more evident during the mature stage of the MCS (1700 - 2000 UTC) between the two simulations. The simulated radar reflectivity fields at 1800 UTC for KFTSPTD and CONTROL (Figure 5.14) show that qualitatively, the distribution of reflectivity is similar with weaker intensities in the KFTSPTD experiment. This may be due to the early onset of the mature stage resulting in the inclusion of some features associated with the dissipative stage of the MCS in the

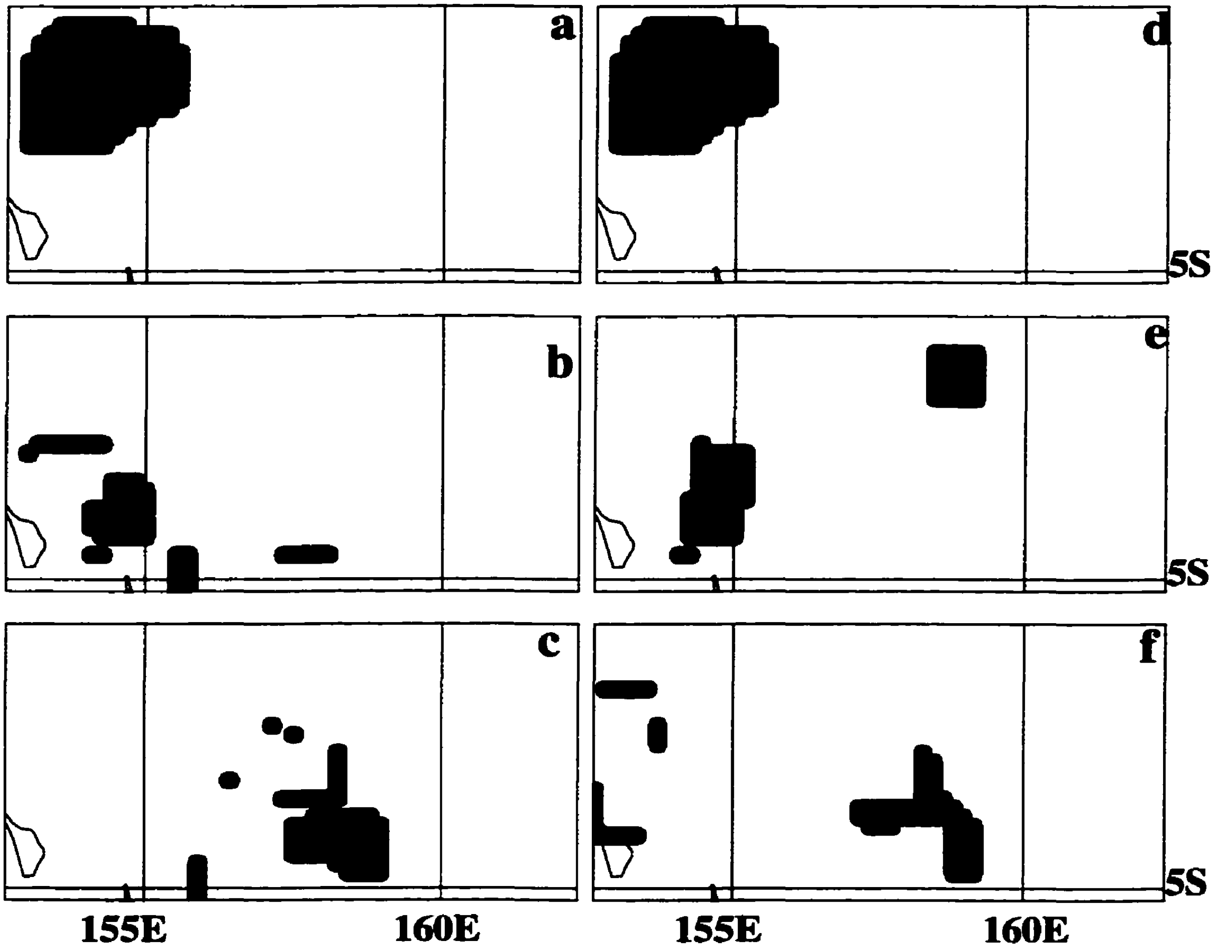

Figure 5.13: New convective onset areas shown by shadings for 0600, 1100 and 1400 UTC from (a-c) CONTROL and (d-f) KFTSPTD. A convective onset is defined to occur when the total rain rate exceeds 3 mm h^{-1} for the first time during the previous 3 h over at least 5% of the area of a box of side 120 km.

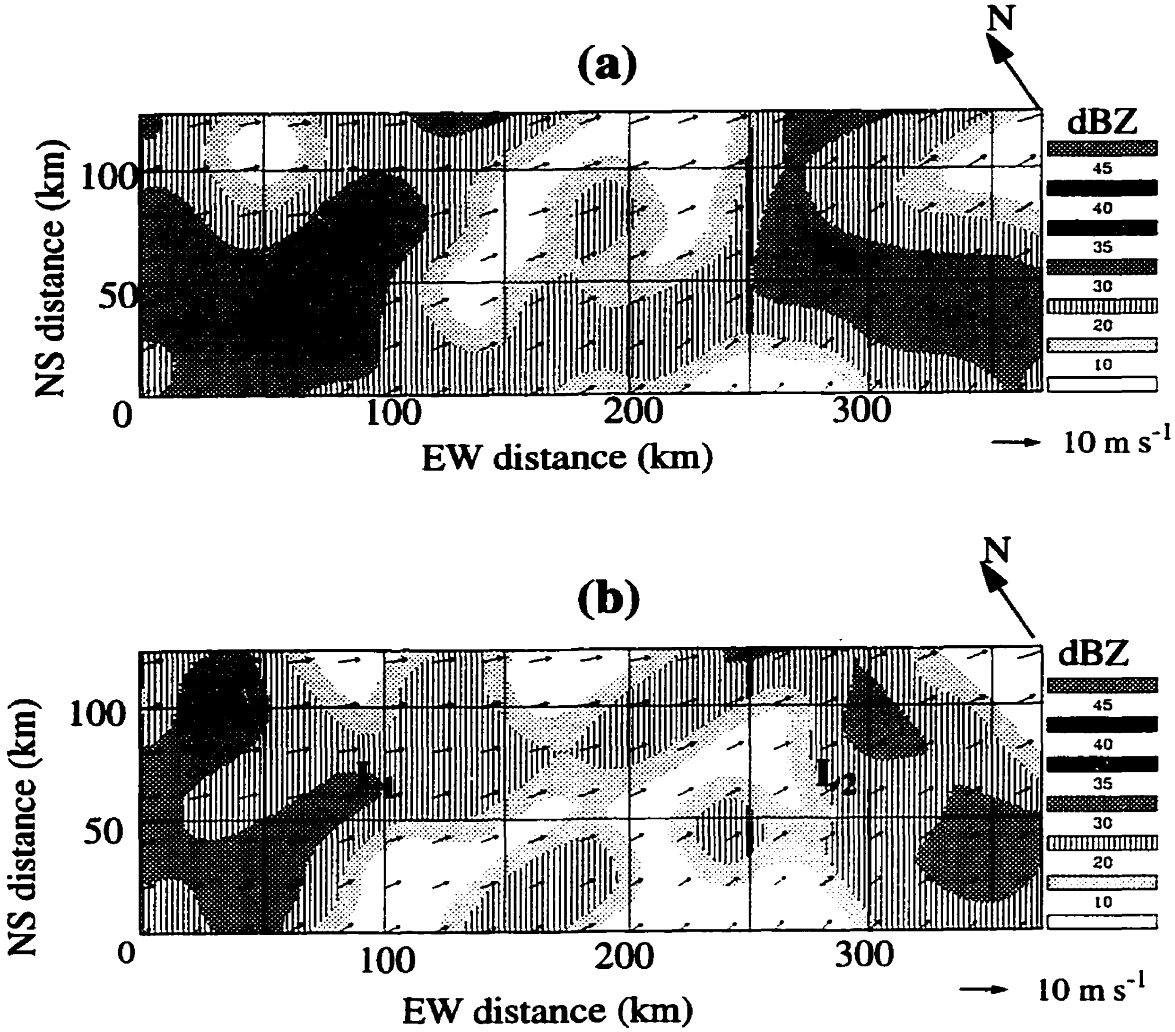

Figure 5.14: Model simulated reflectivity at 1800 UTC along with horizontal winds at 500 m height is shown for (a) the CONTROL simulation and (b) the KFTSPTD trigger function sensitivity experiment. Model reflectivity is computed from total precipitation rate using the relation $Z = 323\ R^{1.43}$. True north for the domain is indicated as 'N'. The lower left corner of the domain is located at 4.45°S 154.49°E.

KFTSPTD experiment.

In summary, sensitivity experiments with various combinations of the KFT function, deep column ascent and SPTD demonstrated that SPTD is largely responsible for the successful prediction of the lifecycle. The deep column ascent results in better timing and location of the MCS during the mature stage suggesting the limited role of ABL eddies in deep convective initiation. Numerical experiments with the original KFT function shows successive maximum and minimum in deep convective activity due to the consumption of CAPE in the first few hours of the simulation. The slow ABL recovery (on the order of 12 hours) leads to the gradual build up of CAPE and another round of deep convection.

Chapter 6

Regulation of convective onsets

6.1 Introduction

The growing and mature stages of the MCS were verified against satellite and radar data in chapter 5. The growing stage was composed of three convective onsets occurring at 0600, 1100 and 1400 UTC (areas A,B and C in Fig. 5.7). During the mature stage, two convective lines oriented in a NE-SW direction were noted. LeMone *et al.* (1998) suggested two possible organizing mechanisms for warm-pool convection. While some convection is organized by the large scale flow (e.g., the ITCZ), others may be self organized in the absence of large scale forcing. One such self organizing mechanism was proposed by Mapes (1993), who suggested that clustering behavior of the warm pool convection arises due to lower tropospheric ascent induced by gravity waves associated with the compensational subsidence in the region heated by an MCS. Chen and Houze (1997) suggested that warm pool convection is regulated by ABL processes. That is the onset of the late afternoon MCSs over the warm pool is due to the diurnal warming of the atmospheric surface layer. Raymond (1995) suggested that deep convection over the warm pool is associated with a near zero convective deficit ($\theta_{et} - \theta_{eb}$). Thus, warm pool convection is regulated by the large scale flow and ABL processes.

In chapter 5, we demonstrated the important role of SPTD in the onset of convection. In this chapter, the causal mechanisms for the timing and location of the three onsets are explored in terms of the large scale vertical motion and SPTD.

6.2 First convective onset (0600 UTC)

Crook (1996) suggested that convective initiation in warm and moist environments is sensitive to SPTD. In Fig. 4.4, we illustrated that there is a large reduction in CIN for a large SPTD, making convective initiation highly probable. In section 4.2.1, we demonstrated that for a threshold value of SPTD, the overlap between the observed area of convective onset and the area enclosed by the SPTD contour is maximized. Thus, a necessary condition for a convective onset in the simulation is that the SPTD exceeds the threshold value.

Figure 6.1a shows the 900 hPa vertical motion at 0400 UTC along with the areas with SPTD > 1.2°C (shaded). The first onset occurs in a region of ascending motion, associated with the transequatorial flow, with moderate values of CAPE (shaded areas in Fig. 6.1b) and the SPTD criterion satisfied (> 1.2°C). Thus, the first onset is characterized by the existence of large-scale ascent, CAPE and favorable SPTD.

6.3 Second convective onset (1100 UTC)

Figure 6.2 shows the vertical motion and horizontal flow at 0800 UTC. The second onset occurs in the confluence zone of westerlies and southwesterlies which is located

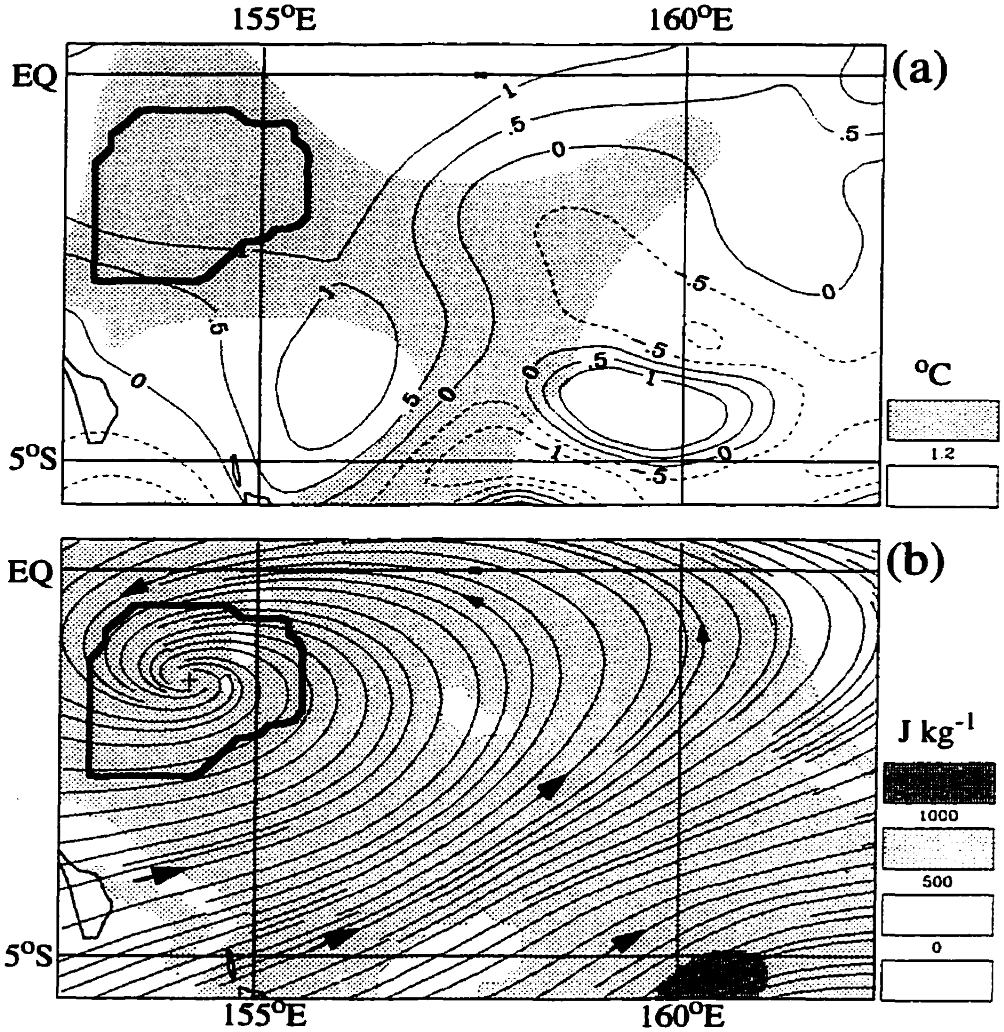

Figure 6.1: (a) The 900 hPa vertical motion at intervals of 0.5×10^{-2} m s^{-1} along with surface potential temperature dropoff (shaded) exceeding 1.2°C and (b) CAPE (J kg^{-1}) and 900 hPa streamlines at 0400 UTC. Thick solid line denotes the area of the first convective onset (0600 UTC).

south of the center of the transequatorial flow (Fig. 6.2b). The onset area is also characterized by moderate CAPE. Even though Fig. 6.1a reveals the existence of ascending motion and moderate CAPE at 0400 UTC, a favorable SPTD does not exist at this time. Thus, the timing of the second onset is regulated by the favorable occurrence of SPTD between 0400 - 0800 UTC.

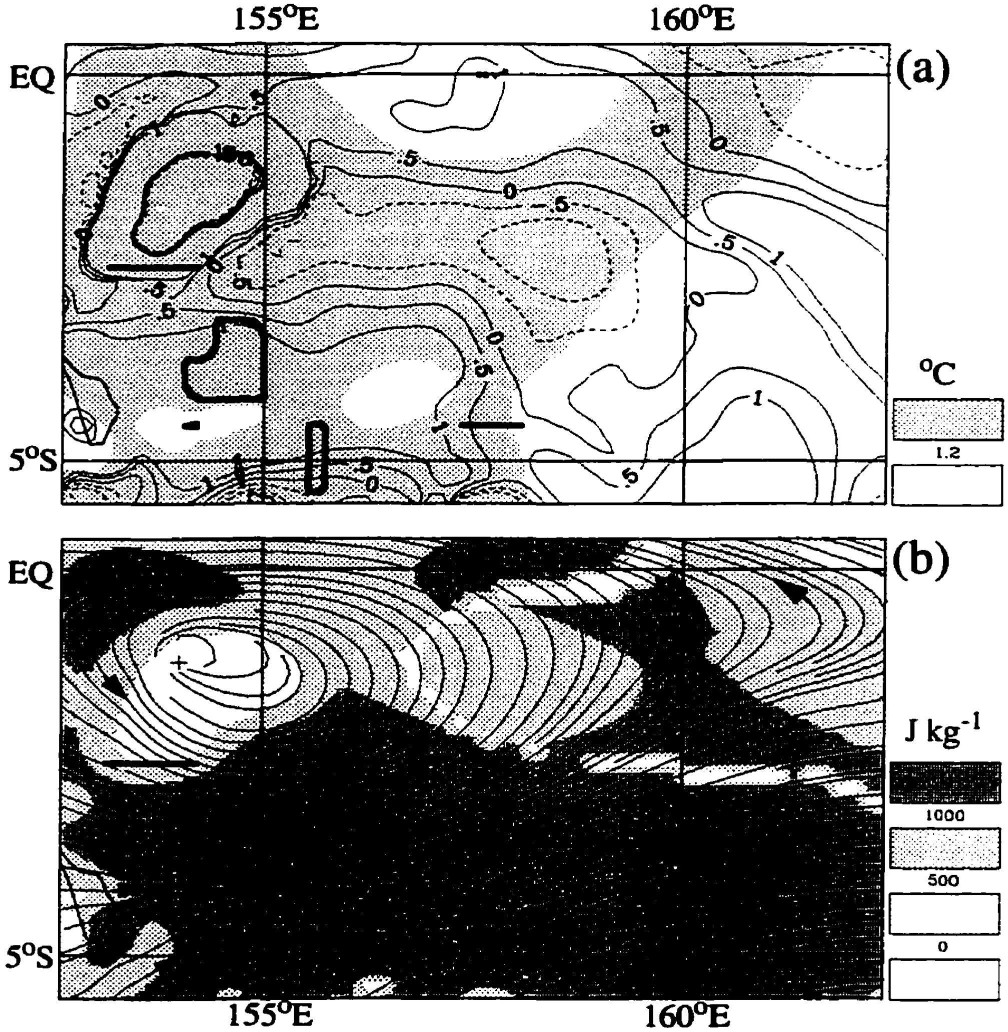

Figure 6.2: (a) The 900 hPa vertical motion at intervals of 0.5×10^{-2} m s^{-1} along with surface potential temperature dropoff (shaded) exceeding 1.2°C and (b) CAPE (J kg^{-1}) and 900 hPa streamlines at 0800 UTC. Thick solid line denotes the area of the second convective onset (1100 UTC).

Recall from section 4.2.1 that SPTD was defined as SPTD $= \theta_{SST} - \overline{\theta_{ABL}}$, where

θ_{SST} and $\overline{\theta_{ABL}}$ are the potential sea surface temperature and the averaged ABL potential temperature, respectively. With little variation of the surface pressure with time and a fixed SST in the simulation, the increase in SPTD is caused by a decrease in the ABL potential temperature. In chapter 7, we will compute the ABL potential temperature budget at 0800 UTC when the heat and moisture budgets of the MCS are determined. The ABL potential temperature budget shows that the decrease in potential temperature arises mainly from the processes of vertical advection of potential temperature and long wave cooling. The magnitudes of the various terms averaged over the ABL and the onset region at 0800 UTC are -0.1 °C day^{-1} (horizontal advection), -7.4 °C day^{-1} (vertical advection), 8.9×10^{-6} °C day^{-1} (solar heating), -1.9°C day^{-1} (longwave cooling), 6.5×10^{-2}°C day^{-1} (vertical diffusion), 1.1°C day^{-1} (deep convection), 5.4×10^{-4} °C day^{-1} (shallow convection) and -0.3°C day^{-1} (explicit microphysics). The cooling of the ABL by vertical advection is caused by large scale ascent associated with the confluence zone (Fig. 6.2). The large scale motion advects low potential temperature air in the ABL upward to increase SPTD which in turn triggers the second convective onset.

6.4 Third convective onset (1400 UTC)

Even though the third onset lies in a region where SPTD exceeds 1.2°C since 0400 UTC, the low level vertical motion becomes favorable only after 1100 UTC (Figs. 6.1a and 6.2a). This suggests that the large-scale vertical motion controls the third convective onset which is responsible for the merger of the entities S_1 and S_2. In this section, we investigate the factors that cause the change in the vertical motion at and after 1100 UTC.

Mapes (1993) has suggested a possible mechanism for the development of ascending motion at the low levels in the region of convective onset. He specified a heating

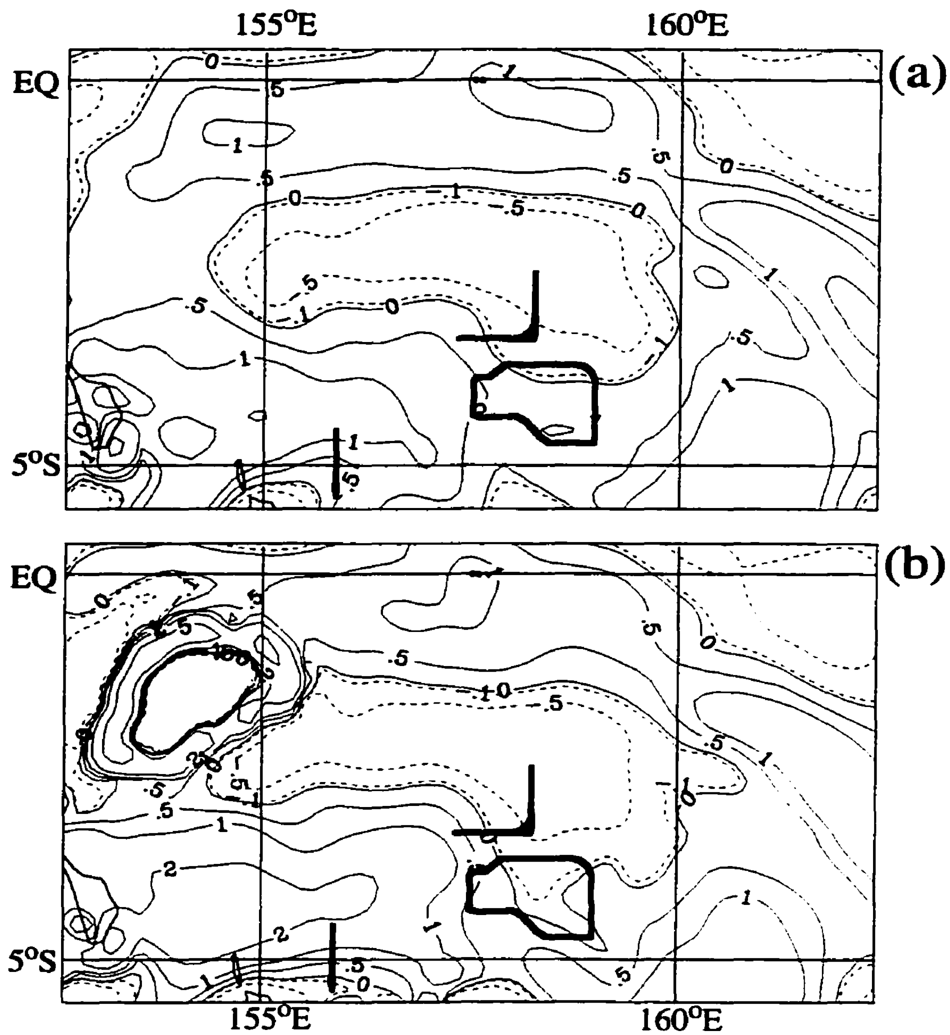

Figure 6.3: The 900 hPa vertical motion at 0800 UTC 15 December 1992 for (a) the DRY simulation and (b) the CONTROL or moist simulation. Dashed (solid) lines represent descending (ascending) motion. Units are 10^{-2} m s^{-1}. Contours -0.5,-0.1,0.0,0.5,1.0,2.0,5.0 are labeled. The area of the third convective onset is indicated in thick solid.

profile similar to that of a tropical MCS and showed that upward displacement occurs in the lowest 4 km in the vicinity of the heat source as a result of gravity waves set off by compensational subsidence associated with deep convection. To test the validity of Mapes hypothesis, we performed a DRY experiment where all condensational heating associated with deep convection and explicit microphysics is turned off. Since deep convection is ruled out in the DRY run, the mechanism for the launching of gravity waves proposed by Mapes is eliminated and therefore the upward motion in the region of convective onset should be absent if the hypothesis were valid.

The vertical velocities at 900 hPa from the CONTROL simulation and the DRY experiment valid at 0800 UTC and 1200 UTC are shown in Fig. 6.3 and Fig. 6.4, respectively. At 0800 UTC, the region of the third convective onset is marked by subsidence in the CONTROL run but there are weak ascending and descending vertical motions occurring in the DRY run. At 1200 UTC, the DRY and the CONTROL runs indicated ascending motion in the onset region. Our results therefore suggest that there might be another process, other than that proposed by Mapes (1993), which is responsible for the development of ascending motions at 1200 UTC.

Several studies have revealed the close connection between tropical convection and the large-scale atmospheric waves. Numaguti (1995) reported the near absence of the 4-6 day and 15-20 day wave activity in the region of S_1 and S_2. Even if these waves were present, their horizontal length scales are too large to explain the mesoscale ascent seen in the region of onset. Takayabu *et al.* (1996) and Chen and Houze (1997) suggested that a quasi-2-day wave can be associated with the warm pool convection. Chen and Houze (1997) noted the existence of 3 well-defined westward propagating 2-day waves between 140-165°E in the vicinity of a latitudinal band (1°N-10°S) for the period 11-15 December. Takayabu *et al.* (1996) identified the quasi-2-day wave from power spectrum analysis of satellite data and linked it to the westward propagating n = 0 and n = 1 inertia-gravity waves. They found that the waves possess a horizontal wavelength of 25-30° and a phase speed of 12-15 ° day^{-1}. The amplitude of the

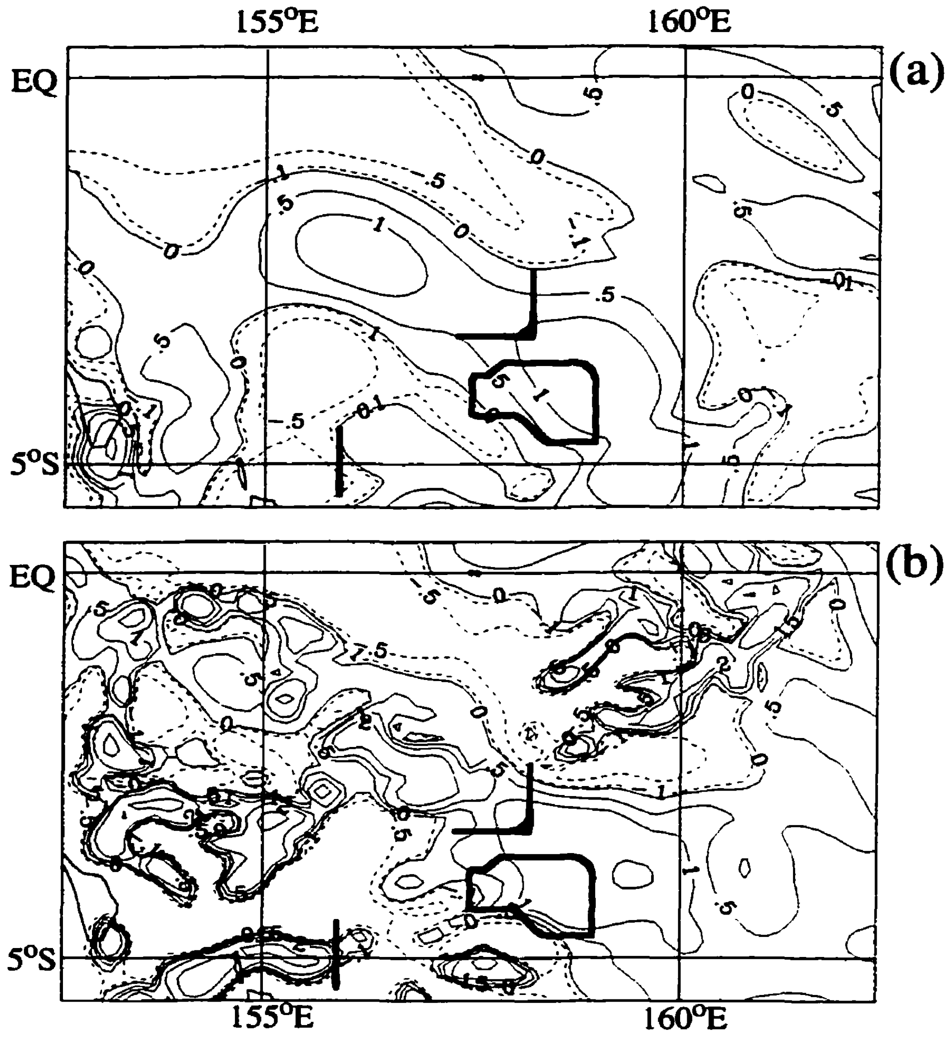

Figure 6.4: Same as Fig. 6.3 except for 1200 UTC 15 December 1992.

wave indicates a maximum at 3°S while the zonal wind components exhibit peak values at 850, 550 and 175 hPa. Vertically, the wind components show an eastward tilt with height. The source of the wave is found to be located around 175 hPa. The composite vertical structures of the zonal, meridional wind components and the horizontal divergence were related to various stages of the lifecycle of an MCS.

Figure 6.5 plots the vertical cross sections of the zonal winds at 0400 UTC from the DRY experiment. The mean value at each level has been subtracted out. It is evident that the zonal wind exhibits an eastward tilt with height around 2.8°S 140.6°E (Fig. 6.5a). A less conspicuous eastward tilt can also be found around 2.8°S 157.4°E. Note that the amplitudes peak at 550 hPa and 175 hPa with magnitudes of 6 m s^{-1}, in good agreement with the values reported in Takayabu *et al.* (1996). The latitude-height section of vertical motion in p-coordinates at 0400 UTC from the DRY experiment is shown in Fig. 6.5b. Corresponding to the two vertical structures in the zonal winds are two regions with strong upward motion (indicated by thick dashed lines in Fig. 6.5b). The horizontal separation between these two structures is around 2000 km and agrees with the wavelength of about 2000-2500 km attributed to the 2-day wave. Thus, the vertical structure and horizontal wavelength associated with the zonal and vertical motion are consistent with the presence of a quasi-2-day wave as reported by Takayabu *et al.* (1996). It maybe mentioned that, although in the DRY experiment all latent heating due to deep convection and explicit microphysics is turned off, the initial conditions are the same as that of the CONTROL and hence contain vertical motion field associated with MCSs present at model initial time (0400 UTC).

To determine the propagation speed and its role in triggering the third convective onset, we plotted in Figs. 6.6 and 6.7 the vertical motion at 0400, 0800 and 1200 UTC along the 2.8°S latitude. At 0400 UTC (Fig. 6.6a) there is subsidence over the third onset region. Although the vertical motion structure moves westward between 0400 - 0800 UTC due to the westward propagation of the quasi-2-day wave, the

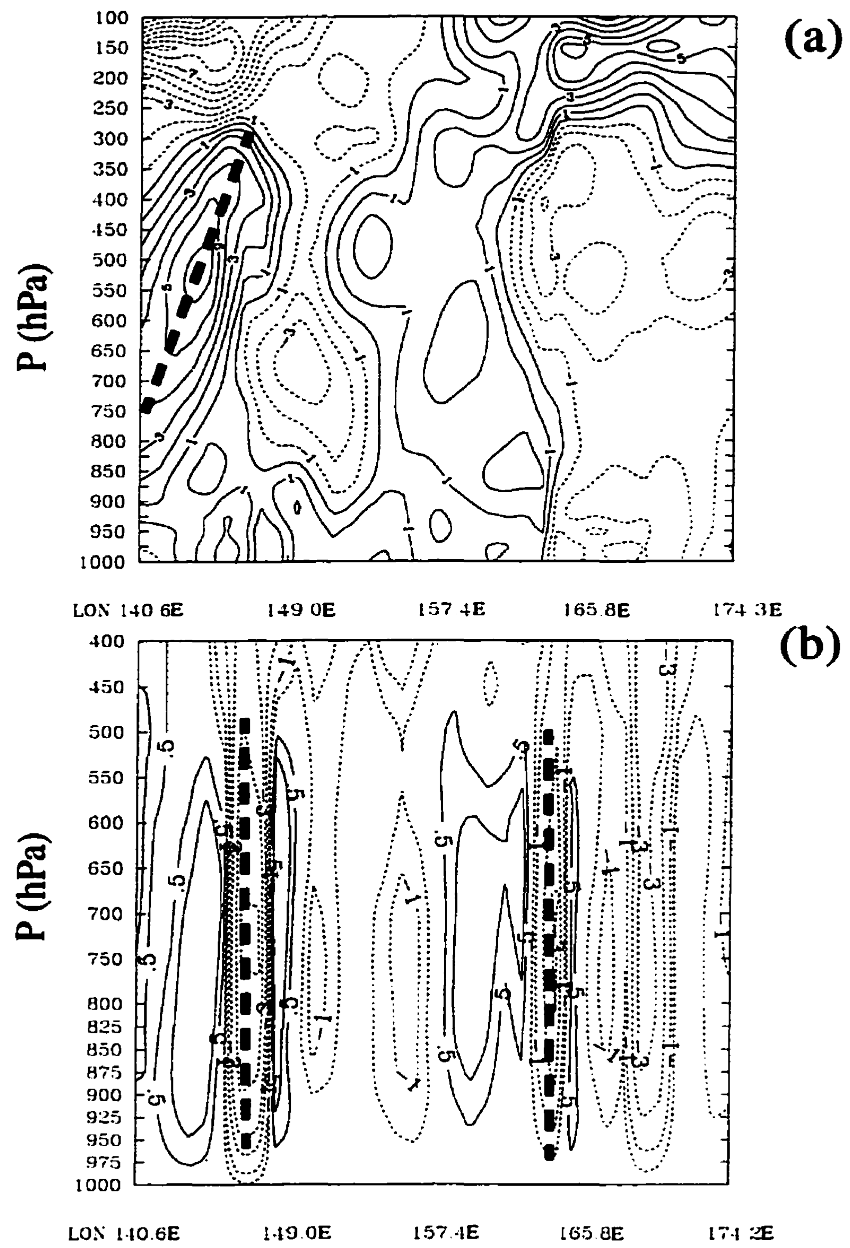

Figure 6.5: Vertical cross section of (a) the zonal wind (m s^{-1}), with the mean at each level subtracted out and (b) the vertical motion (10^{-1} Pa s^{-1}) from DRY simulation valid at 0400 UTC 15 December 1992. The section is taken along 2.8°S latitude from 140.6-174.3°E. The contour interval for the zonal wind is 1 m s^{-1}. Vertical motion contours are -7.0,-5.0,-3.0,-2.0,-1.0,-0.5,0.5,1.0,3.0. The thick dashed lines indicate the vertical structure associated with a quasi-2-day wave.

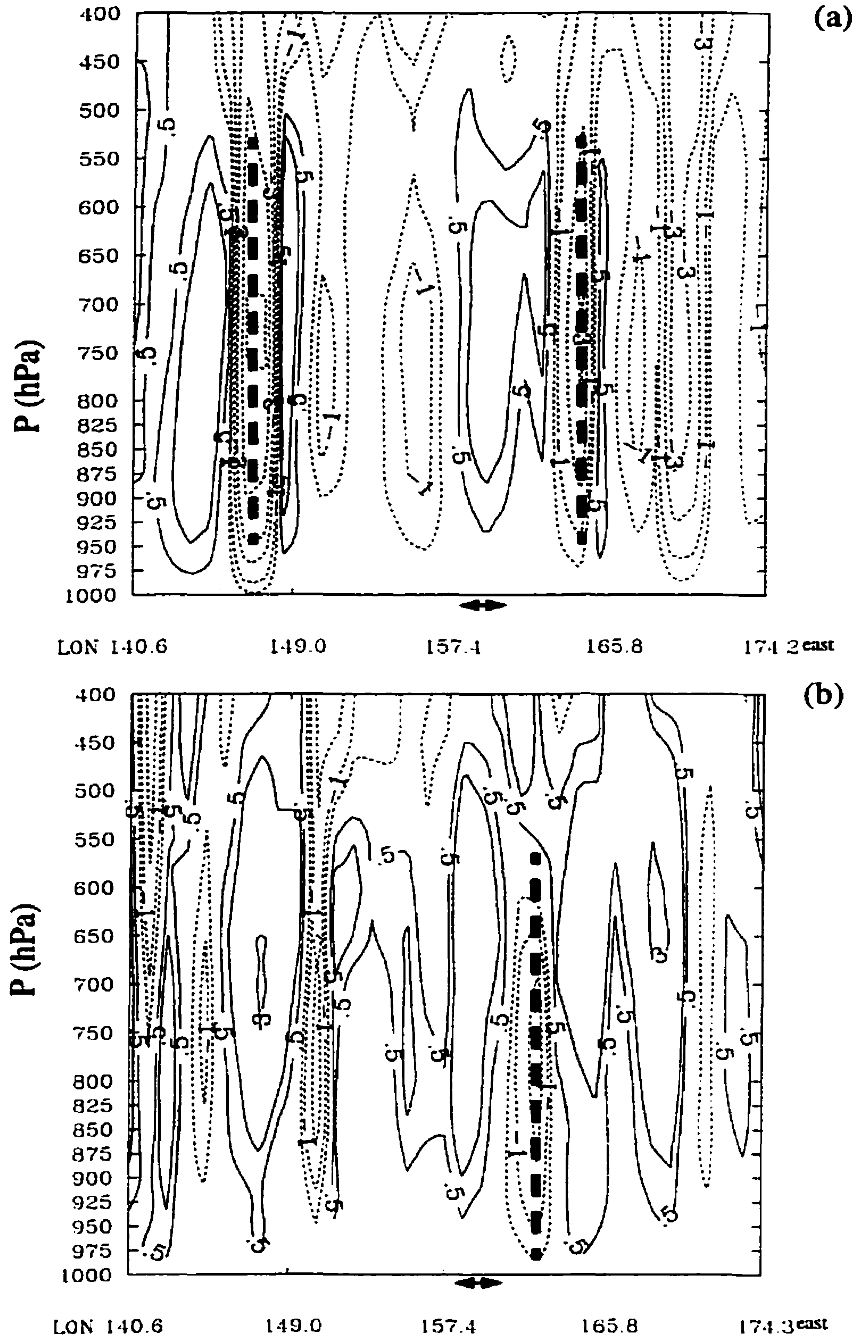

Figure 6.6: Latitude-height section of vertical motion (10^{-1} Pa s^{-1}) taken along 2.8°S latitude from DRY run valid at (a) 0400 UTC and (b) 0800 UTC 15 December 1992. The thick dashed lines indicate the vertical structure associated with a quasi-2-day wave. The region of the third convective onset is also indicated around 157.1°E.

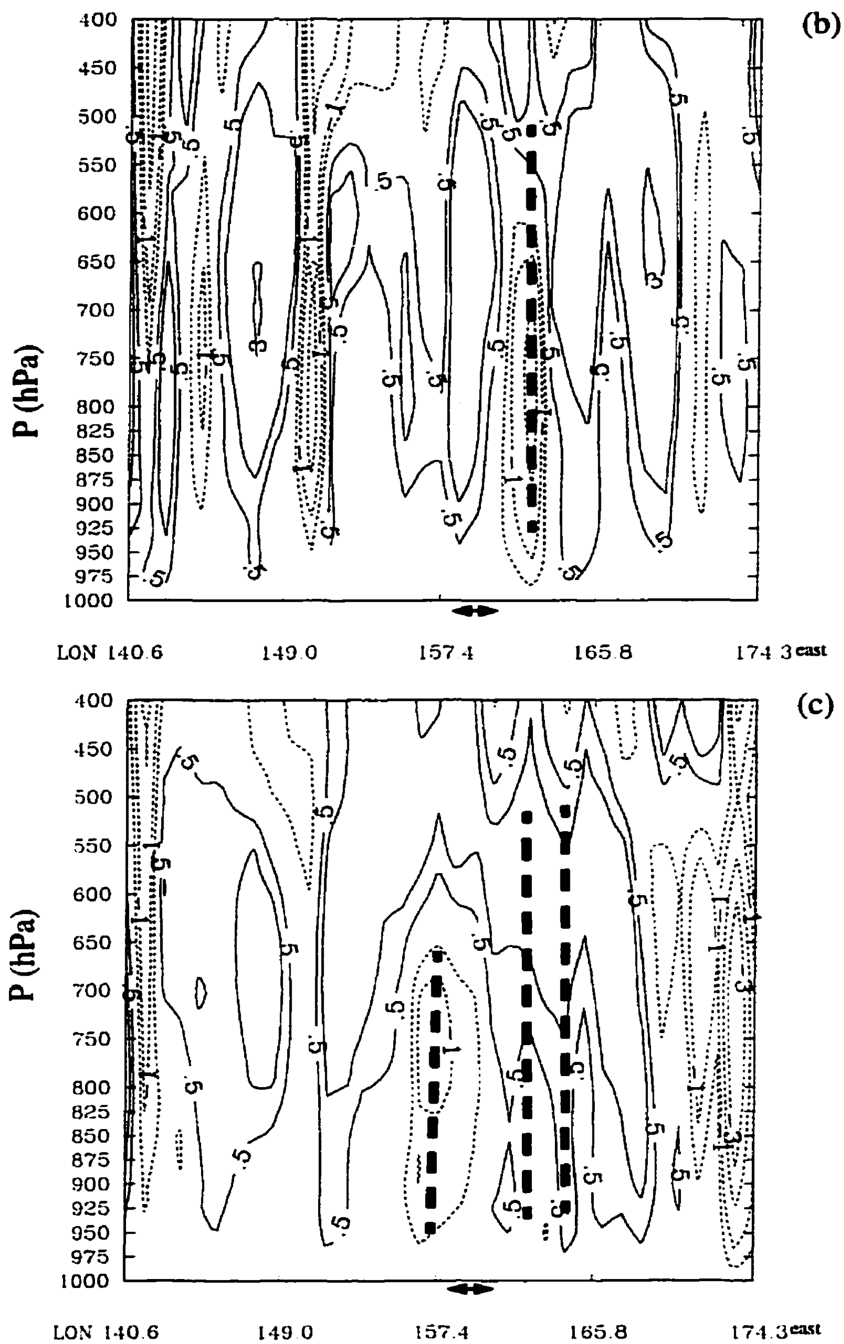

Figure 6.7: Same as Fig. 6.6 except for (b) 0800 UTC and (c) 1200 UTC. The location of the vertical structure associated with the quasi-2-day wave at 0400,0800 and 1200 UTC is indicated in (c).

third onset region still experiences downward motion precluding the onset of deep convection (Fig. 6.6b). However by 1200 UTC, the third onset region exhibits upward motions with further westward propagation of the wave (Fig. 6.7c). Clearly the third convective onset is modulated by the propagation of the quasi-2-day wave. The westward propagation speed inferred from Fig. 6.7c is consistent with a propagation speed of 12-15° day^{-1} reported by Takayabu *et al.* (1996). Thus it may be concluded that there is evidence of the presence of the 2-day wave in the region of the third onset and it regulates the mesoscale vertical motion field to trigger the third convective onset at 1400 UTC.

Thus, the mechanism for lifting at low levels proposed by Mapes (1993) is not responsible for the third convective onset. The merger of S_1 and S_2 is associated with the outbreak of new convection triggered by the build-up of ascending motion caused by the westward propagation of the quasi-2-day wave. Thus the existence of the 2-day wave in near equatorial latitudes enhances the predictability of the MCS by controlling the mesoscale vertical motion field.

6.5 Conclusions

Webster and Lukas (1992) pointed out the need for lifecycle studies of MCSs over the warm pool. Observational studies using airborne Doppler radar data are restricted to the mature and dissipating stages of the lifecycle. Numerical simulations based on realistic or observed initial conditions are severely hampered by the problem of appropriate treatment of deep convection, especially the lack of suitable convective initiation mechanisms in the model for the warm pool environment. In this chapter, the factors responsible for the successful prediction of the lifecycle of the 15 December 1992 TOGA COARE MCS were investigated.

The lifecycle consisted of three convective onsets and the mature stage exhibited two convective lines (L_1 and L_2) with their associated stratiform regions. The first convective onset (0600 UTC, Fig. 6.1) forms in a region of moderate CAPE, large scale ascending motions associated with the transequatorial flow and favorable SPTD (SPTD > 1.2°C). The second onset (1100 UTC, Fig. 6.2) occurs when SPTD exceeds 1.2°C for the first time at 1100 UTC. The increase in SPTD arises due to the cold vertical advection of potential temperature and the long wave cooling of the ABL. The former is caused by the confluence of southwesterlies and westerlies and occurs to the south of the transequatorial flow center. Favorable SPTD exists for the third convective onset (1400 UTC, Fig. 6.3) at the model initial time. However, the large-scale vertical motion only becomes favorable during 1200 - 1400 UTC (i.e. upward in the lowest 400 hPa) due to the westward propagation of the quasi-2-day wave. Vertical sections of the zonal winds and the vertical motion indicate structures consistent with the presence of a quasi-2-day wave at 2.8°S latitude.

Chapter 7

Heat and Moisture Budgets

In this chapter, we will quantify the effects of the MCS on the heat and moisture budget of the atmosphere, and present the surface energy budget. Section 7.1 contains the budget equations and computational procedures. Sections 7.2 - 7.4 describes the results.

7.1 Budget equations

Traditionally, the apparent heat source Q_1 (Yanai *et al.*, 1973) is defined in terms of the dry static energy ($s = c_p T + gz$) as

$$Q_1 \equiv \left(\frac{\partial s}{\partial t} + v \cdot \nabla s + w \frac{\partial s}{\partial z} \right) \tag{7.1}$$

Using the hydrostatic approximation, equation (7.1) becomes

$$Q_1 \equiv C_p \pi \left(\frac{\partial \theta}{\partial t} + v \cdot \nabla \theta + w \frac{\partial \theta}{\partial z} \right) \tag{7.2}$$

where θ is the potential temperature. The source and sink terms for Q_1 can be written as

$$Q_1 \equiv \frac{L_v}{C_p\pi}(c-e) - \frac{1}{\rho}\frac{\partial\left(\rho\overline{w'\theta'}\right)}{\partial z} + Q_R \tag{7.3}$$

where L_v is the latent heat of vaporization of water, C_p is the specific heat of air at constant pressure, c is the rate of condensation /deposition, e is the rate of evaporation / sublimation, ρ is the air density and Q_R is the net radiative heating term. Note that

$$c - e = (c-e)_{KF} + (c-e)_{BM} + (c-e)_{EM} \tag{7.4}$$

and

$$Q_R = Q_{SO} + Q_{IR} \tag{7.5}$$

where KF,BM,EM,SO and IR stand for the Kain-Fritsch CPS, the Betts-Miller CPS, Explicit Microphysics, Solar Radiation and Infrared Radiation, respectively. The vertical diffusion is obtained from the boundary layer scheme. Since the thermodynamic equation in the MC2 model is given by the virtual temperature equation (A.5), we introduce an additional equation for θ in the model, in order to compute Q_1 in (7.2).

Similarly, the apparent moisture sink Q_2 is

$$Q_2 \equiv -\frac{L_v}{C_p}\left(\frac{\partial q_v}{\partial t} + v\cdot\nabla q_v + w\frac{\partial q_v}{\partial z}\right) \tag{7.6}$$

where the source and sink terms are

$$Q_2 \equiv L_v(c-e) + \frac{L_v}{\rho}\frac{\partial}{\partial z}\left(\rho\overline{w'q'}\right) \tag{7.7}$$

To obtain residue-free budgets, each term in equations (7.2) and (7.6) are computed explicitly. We first compute the horizontal advection terms ($v\cdot\nabla\theta$ and $v\cdot\nabla q_v$) using a 2-D semi-Lagrangian advection scheme. We then compute the 3-D horizontal advection term using the 3-D semi-Lagrangian scheme. The difference between these two advection quantities yields the vertical advection term. The right hand sides of these equations (7.3 and 7.7) constitute the source and sink terms and are available from the physics package. To determine the accuracy of the computation, we compare (7.2) against (7.3), and (7.6) against (7.7). It was found that they agree to within 1% at any instant during the 16 h simulation.

The net energy flux into the ocean Q_{net} is given by Grant and Hignett (1998):

$$Q_{net} = (1 - \alpha_s)F_s + \epsilon_s(F_I - \sigma_{SB}{T_s}^4) - H_S - L_v E_s \tag{7.8}$$

where F_S is the downward solar flux, α_s is the surface albedo, ϵ_s is the surface emissivity of the ocean (set to 0.94), F_I is the downward infrared radiation flux, T_s is the sea surface temperature, σ_{SB} is the Stefan-Boltzmann constant, H_S is the sensible heat flux and $L_v E_s$ is the latent heat flux.

7.2 Heat and moisture budgets of the MCS

The time variation of $Q_1 - Q_R$ and Q_2, averaged over a domain (152.5 - 161°E and 0 - 5°S, shaded in Fig. 5.3), are plotted in Figures 7.1a and 7.2a, respectively. When the spin-up period of 0600 - 0900 UTC is excluded, the $Q_1 - Q_R$ and Q_2 profiles indicate upper (300 hPa) and lower (925 hPa) level heating and drying. Between 450 - 700 hPa, cooling and moistening occurs. Moistening of the ABL takes place throughout the simulation period (Fig. 7.2a).

Figures 7.1a and 7.2a indicate that the lower and upper level drying and heating, as well as the midlevel moistening and cooling intensify between 0900 - 1700 UTC, attaining maximum values during 1700 - 2000 UTC. The intensification of the upper and lower level heating and midlevel cooling with time is associated with an increase in the area occupied by deep convection, as is evident in an increase in anvil cloud coverage when the MCS evolves (see Fig. 5.6). Lewis (1975) analyzed data collected during the mature stage of a squall line. He noted the occurrence of the lower and upper level heating and drying peaks, with cooling and moistening between 600 - 700 hPa. His heating peaks at 800 hPa and 250 hPa were 40°C day^{-1} and 60°C day^{-1}, respectively. His cooling peak at 650 hPa was -10°C day^{-1}. The drying peak at 800 hPa was 70°C day^{-1}. Two moistening peaks occur at 550 hPa and 700 hPa respectively, each with a magnitude of -10°C day^{-1}. Nitta (1977) estimated the Q_1 and Q_2 profiles for a GATE tropical cloud cluster. During its dissipation stage, he noted heating and drying peaks at 900 and 350 hPa and moistening and cooling in the 500 - 600 hPa layer. The magnitude of heating at 900 and 350 hPa were 2.5°C day^{-1} and 1.0°C day^{-1}, respectively. The magnitude of cooling at 550 hPa was 5°C day^{-1}. The peak drying occurred at 850 and 300 hPa with magnitudes of 5°C day^{-1} and 2.0°C day^{-1}, respectively. A maximum midlevel moistening of 5°C day^{-1} at 650 hPa was also noted. Nuret and Chong (1998) reported the heat and moisture budgets of an MCS that occurred over the warm pool during TOGA-COARE. While their Q_1 profile exhibited heating throughout the troposphere, the Q_2 profile indicated significant moistening below the freezing level. Thus, our simulated magnitudes for the heating peaks at 925 and 300 hPa of 3°C day^{-1} and 12°C day^{-1} respectively are consistent with the results of Nitta (1977) and Nuret and Chong (1998). The finding of midlevel moistening and cooling is also consistent with those of Lewis (1975), Nitta (1977) and Nuret and Chong (1998).

To explain the Q_1 profile (Fig. 7.1a), the contribution of deep convection, explicit microphysics, and the ABL process are shown in Figs. 7.1b - d respectively. Since the MCS evolves during the nighttime, the contribution from solar radiation is absent for the most part (not shown). The contribution due to shallow convection during the growing and mature stages is relatively small (not shown). The major contributors to the heating profile are deep convection, explicit microphysics and the ABL processes (Fig. 7.1b, c and d respectively). The ABL processes are associated with the vertical transfer of sensible heat from the ocean surface and are confined to the

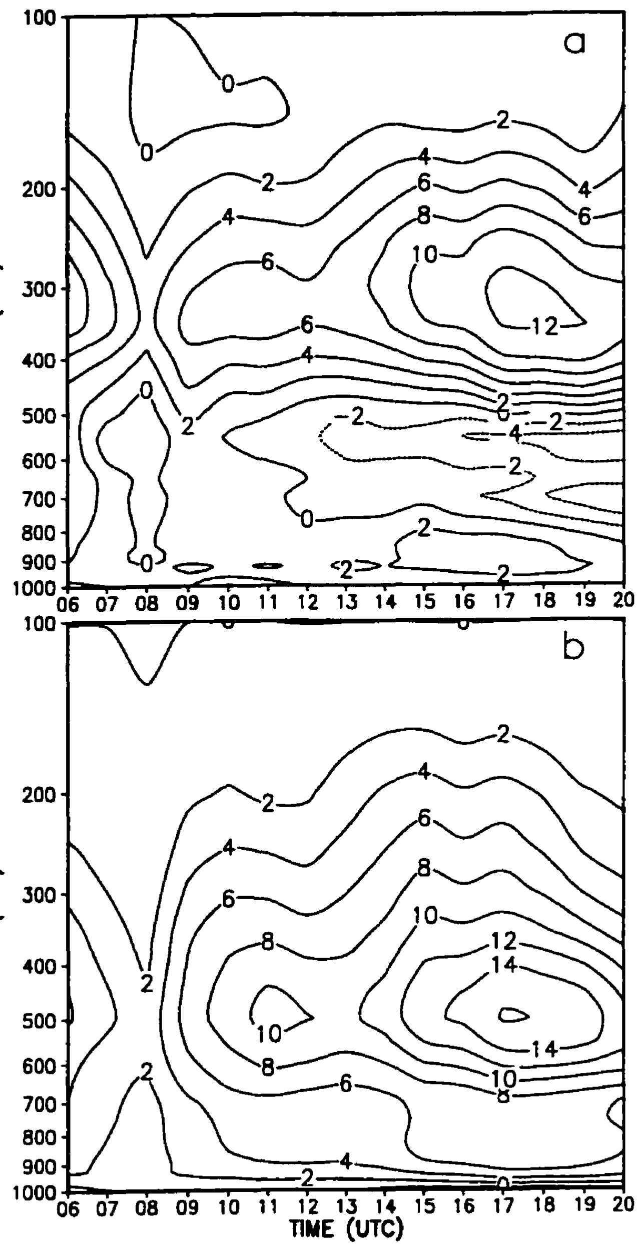

Figure 7.1: Time-height section of the domain averaged (shaded in Fig. 5.3) (a) apparent heating source, (b) heating rates due to deep convection from the KF CPS, (c) the explicit microphysics and (d) ABL vertical diffusion. The heating rates are expressed in K day^{-1}.

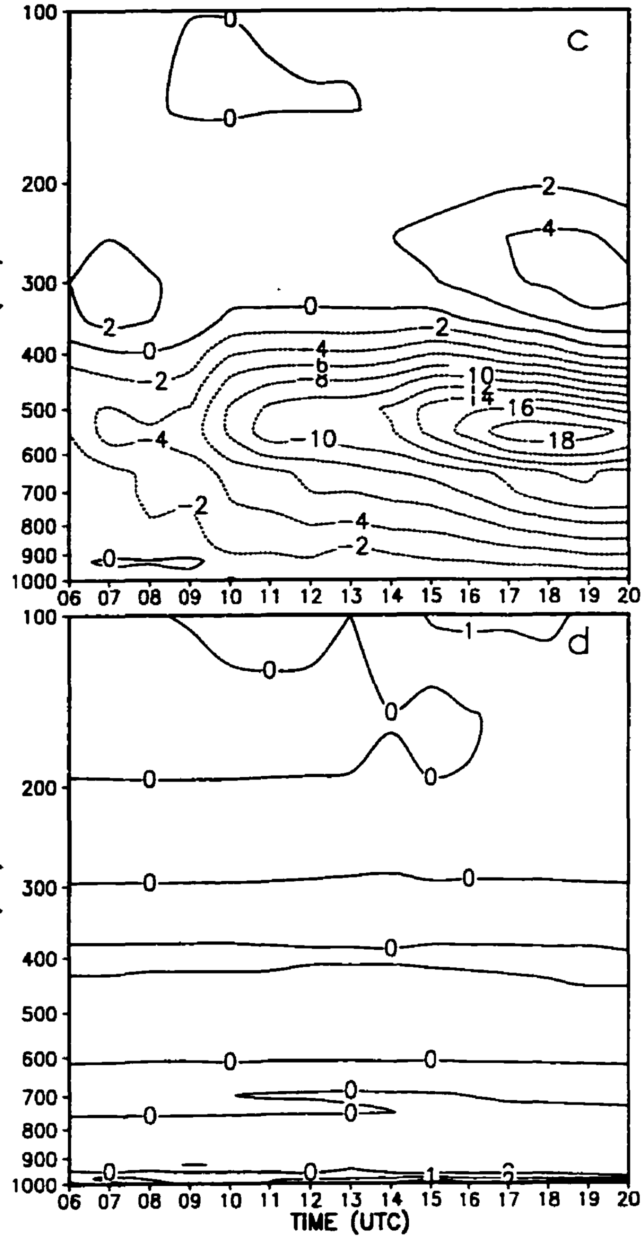

Figure 7.1: Continued.

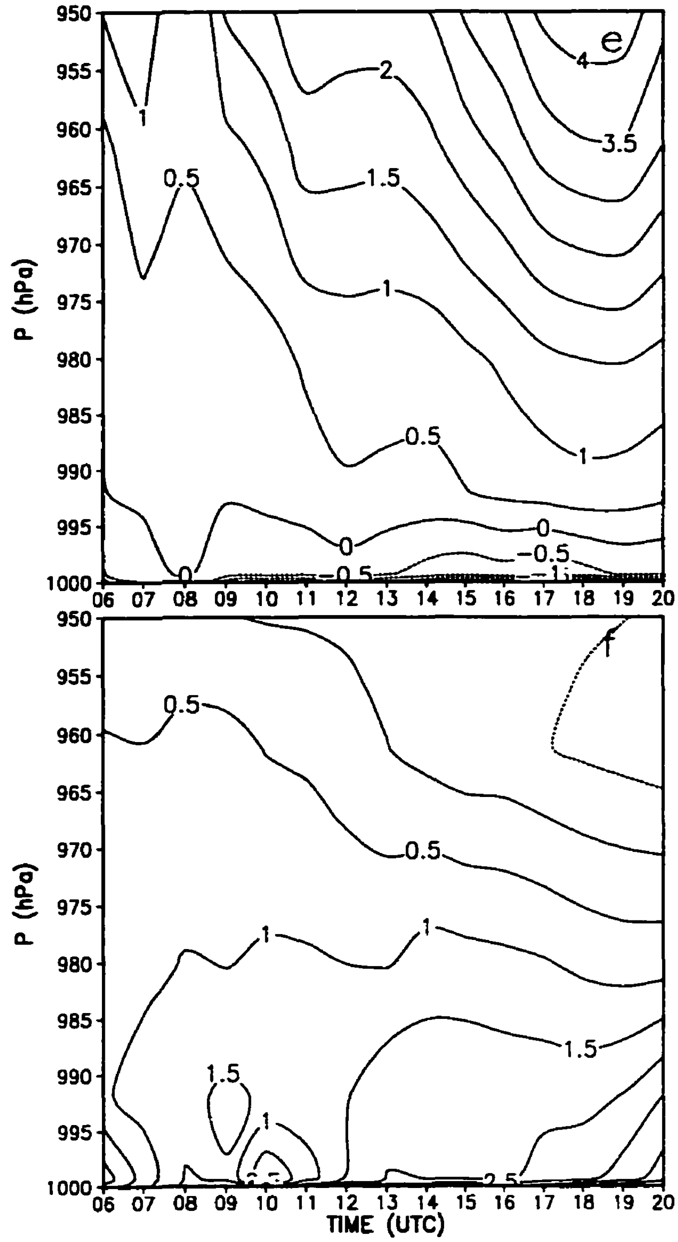

Figure 7.1: Same as Fig. 7.1 (b) and (d) but for the heating rates (K day^{-1}) in the atmospheric boundary layer. That is, the heating rates for deep convection and atmospheric boundary layer diffusion process are shown in (e) and (f) respectively.

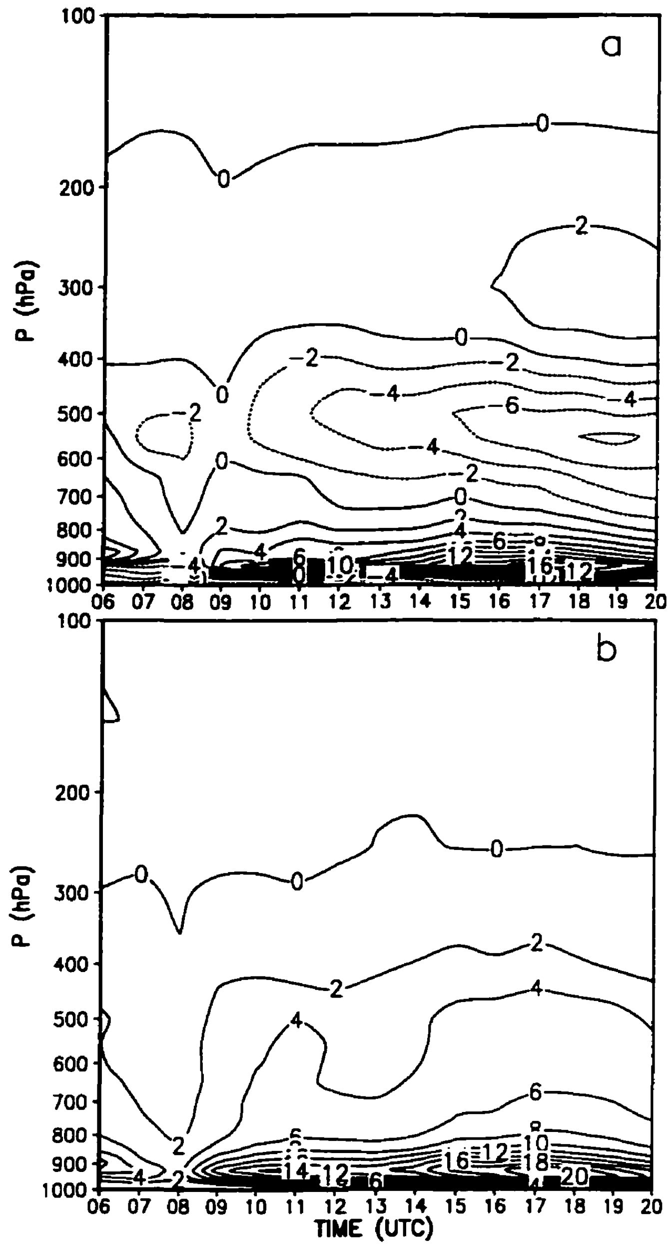

Figure 7.2: Time-height section of the domain average (shaded in Fig. 5.3) (a) apparent moisture sink contributions to it from (b) deep convection (KF CPS), (c) the explicit microphysics, (d) atmospheric boundary layer diffusion process and (e) the shallow convection (BM shallow CPS). The heating rates are expressed in K day^{-1}.

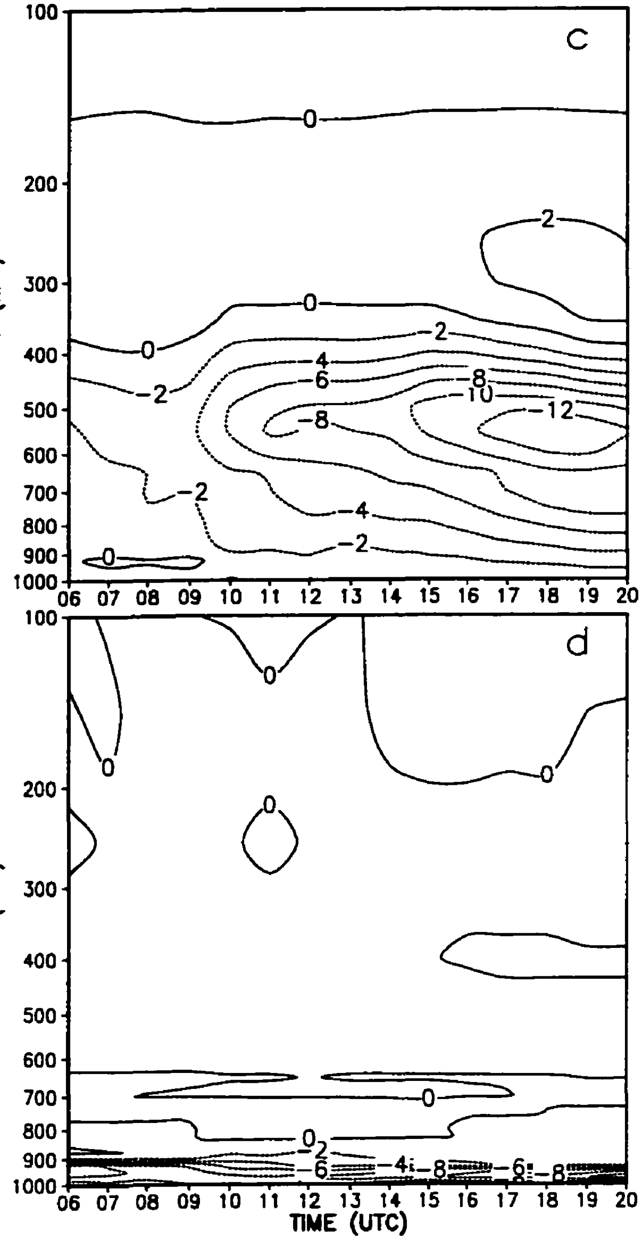

Figure 7.2: Continued.

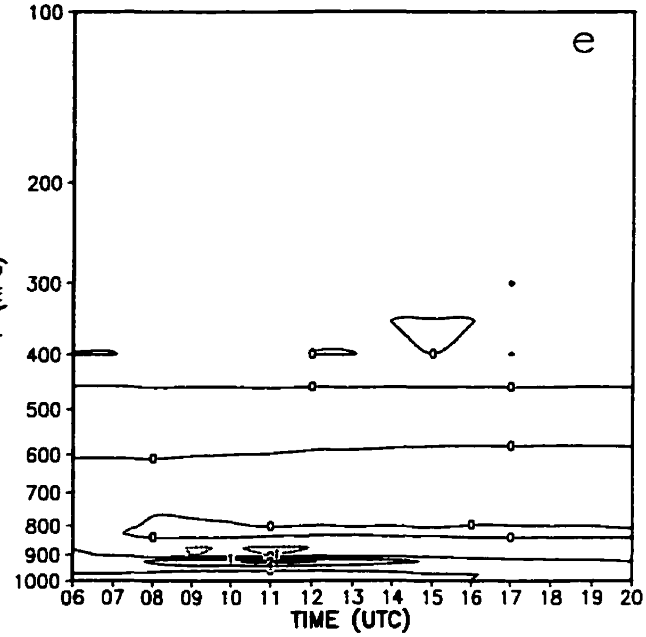

Figure 7.2: Continued.

lowest 50 hPa layer. A magnified view of the 1000 - 950 hPa layer (Figures 7.1 e and f) indicates that the cold pool from deep convection intensifies with time (1400 - 2000 UTC). Consequently, there is enhanced transport of sensible heat flux into the ABL. Above the ABL, the heating profile is dominated by deep convective and the explicit microphysical processes. The heating peak in Q_1 at 300 hPa is caused by deep convective heating (Fig. 7.1b) and the latent heat from vapor deposition on ice particles detrained from the convective clouds (Fig. 7.1c). The 925 hPa heating peak arises due to deep convective heating which is offset somewhat by cooling from the evaporation of rain and cloud droplets. The midlevel (500 - 700 hPa) cooling arises from the sublimation of ice particles (detrained from convective clouds) above the freezing level ($\approx$600 hPa) and the evaporation of rain and cloud droplets below. Clearly, most of this cooling is offset by the heating effects of deep convection. The difference in the levels of maximum deep convective heating (500 hPa) and maximum sublimation/ evaporational cooling (600 hPa) resulted in a double cooling peak structure (550 hPa and 700 hPa) in Q_1 during the mature stage of the MCS (1700 - 2000 UTC, Fig. 7.1a).

The various physical processes contributing to the Q_2 profile (Fig. 7.2a) are deep convection, explicit microphysics, ABL process, and shallow convection (Fig. 7.2b - e). The ABL moistening is associated with the vertical transport of surface vapor flux from the ocean surface (Fig. 7.2d). The drying between 700 - 925 hPa is caused mainly by the drying effects of deep convection (Fig. 7.2b). The location of the peak drying occurs just above the ABL in agreement with the results of Kain and Fritsch (1990). Also during the growing stage (0600 - 1700 UTC), some drying due to shallow convection is evident (Fig. 7.2e). Although the drying effects are relatively small compared to those of deep convection, it is significant in the sense that it provides a suitable mechanism to prevent the development of any grid scale CISK-like instability. Moistening in the 400 - 700 hPa layer is caused by the sublimation of ice particles above the freezing level and evaporation of rain drops below the freezing level. The upper level drying peak during the mature phase (1700 - 2000 UTC) results from the process of vapor deposition on ice crystals detrained at the convective cloud tops.

In passing, we mention that Houze (1989) found that the heating profiles in the stratiform regions of MCSs are similar over different locations in the world. However, the Q_1 profile in convective regions were found to vary from place to place. In the WPR, the observed peak in convective heating is located around 500 hPa. Kain and Fritsch (1990), using the KF CPS, found a similar peak in the Australian monsoon region during AMEX. Our result over the warm pool (Fig. 7.1b) also indicates a heating peak around 500 hPa.

7.3 Heat and moisture budgets of the MPF

In chapter 1, we defined the MCS as composed of one or more mesoscale precipitation features. The heat and moisture budgets of the MCS presented in section 7.2 represent averages over a length scale on the order of a thousand kilometers. In this section, we focus on individual MPFs and present the budgets averaged over the areas of convective onset discussed in Chapter 5.

The apparent heat source ($Q_1 - Q_R$) and the apparent moisture sink (Q_2) profiles, averaged over the area occupied by convective onset 2 and onset 3 (see Chapter 5 for details) are depicted in Figs. 7.3 and 7.4, respectively. In comparison to Fig. 7.1a and Fig. 7.2a, the vertical distribution of the profiles indicates similar characteristics although the magnitudes are larger for the MPFs. Of interest is that for onset 2 (Fig. 7.3a), the peak in the apparent heat source around 300 hPa occurs both at 1100 UTC and 1800 UTC. It appears that after convection breaks out at 1100 UTC, the ABL needs some time to recover before another round of convection can take place.

The ABL recovery process for onset 2 is revealed in Fig. 7.5. The figure plots the vertical eddy diffusion terms in Q_1 and Q_2 (second term in Eqns. 7.3 and 7.7), averaged over the area of convective onset. Before 1000 UTC, there is warming and moistening in the ABL. When deep convection first breaks out shortly after 1000 UTC, cooling occurs below 990 hPa in response to the cold downdraft in the KF CPS. The moistening also decreases as a result of compensating subsidence. After the first round of convection dissipates, vertical diffusion of heat and moisture from the ocean surface gradually restores. There is warming from 1200 - 1700 UTC in the 1000 - 950 hPa after 1100 UTC. The ABL therefore recovers from the first round of convection and is ready to support the second round of convection around 1800 UTC. The recovery time of about 7 - 8 h is consistent with the findings of Raymond (1995) who reported a recovery time on the order of half a day.

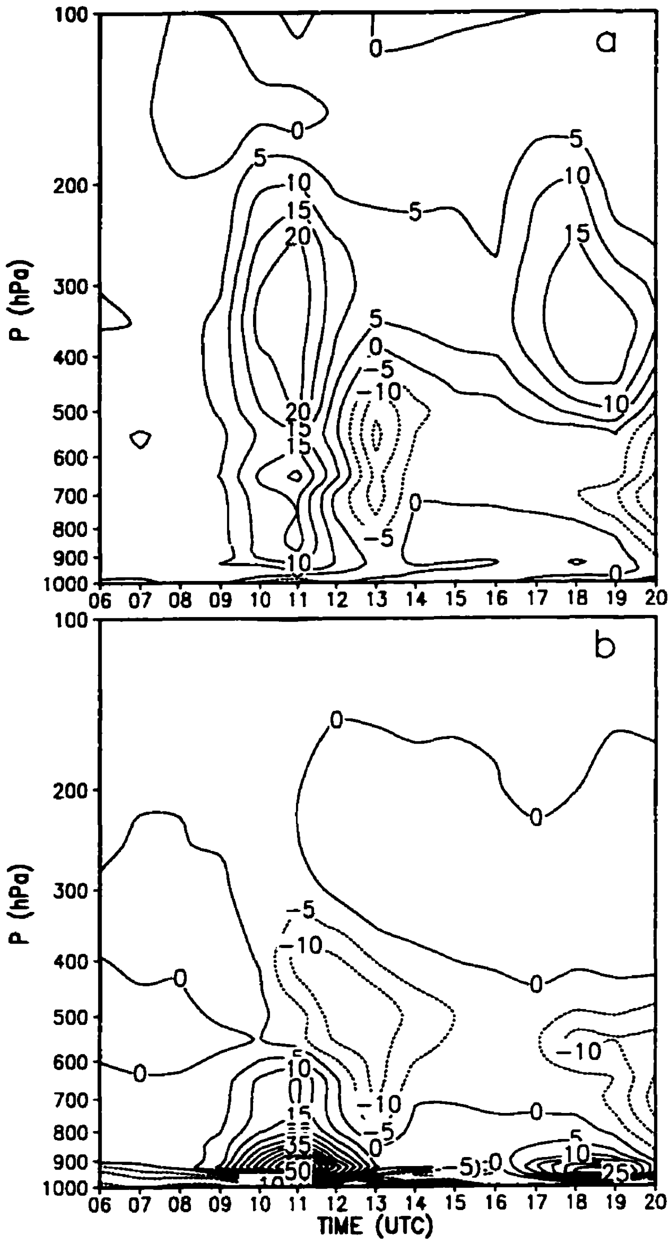

Figure 7.3: Time-height section of the domain average (over the second onset area or area B in Fig. 5.7) apparent heating source (a) and apparent moisture sink (b). The heating rates are in units of K day^{-1}.

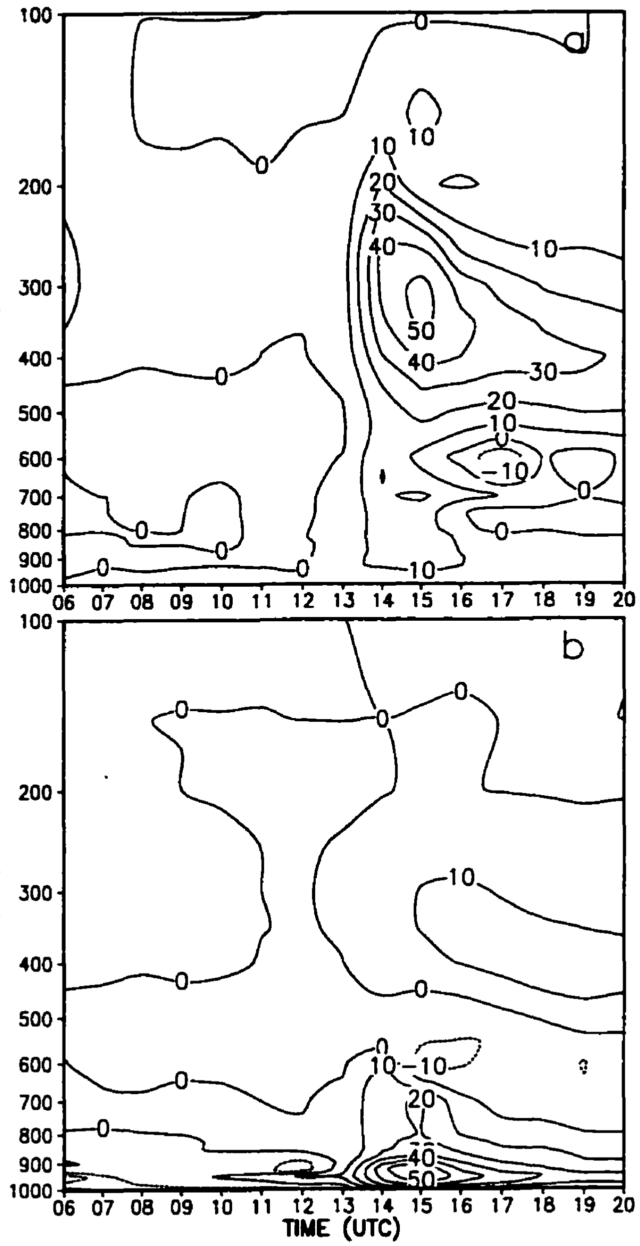

Figure 7.4: Time-height section of the domain average (over the third onset area or area C in Fig. 5.7) apparent heating source (a) and apparent moisture sink (b). The heating rates are in units of K day^{-1}.

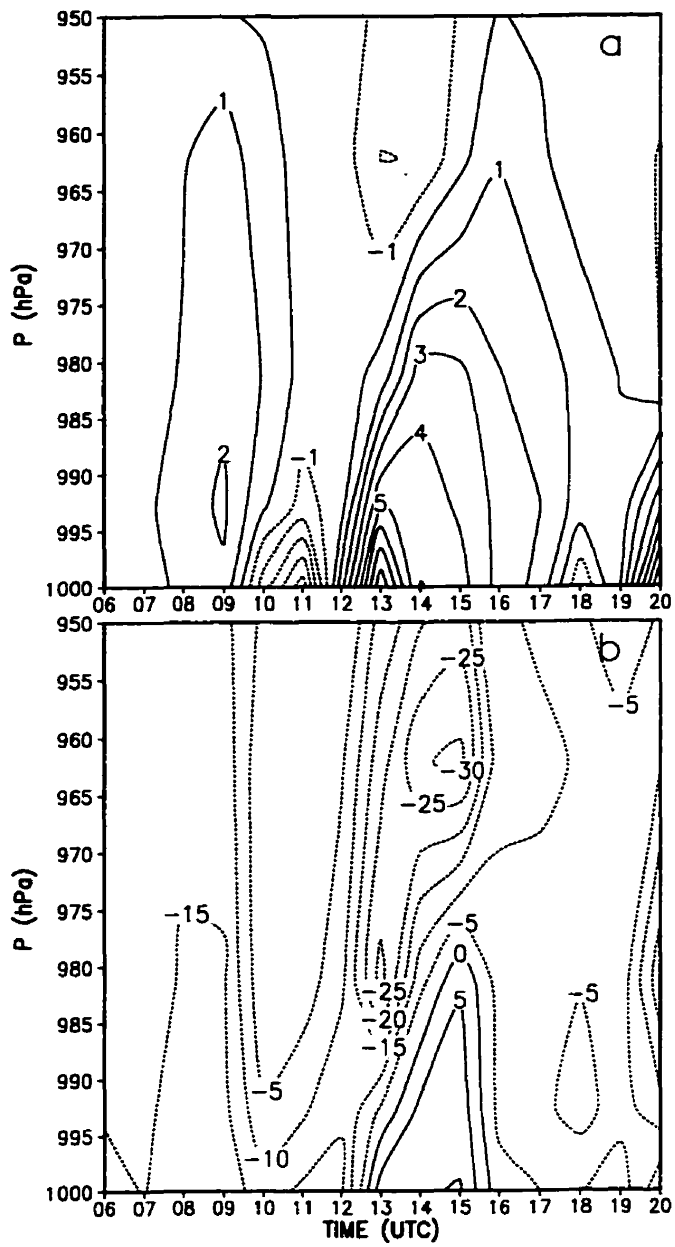

Figure 7.5: Time-height section of the domain-average (over the second onset area or area B in Fig. 5.7) contribution to (a) $Q_1 - Q_R$ and (b) Q_2 by ABL diffusion processes. The rates are in units of K day^{-1}.

7.4 Surface energy balance

The residual ocean flux term (Q_{net}) is computed from the terms on the right hand side of equation (7.8). The areal average of the various terms in the surface energy balance (SEB) is performed over the domain (shaded in Fig. 5.3) and for the period 0800 - 2000 UTC (section 7.4.1). In section 7.4.2, the effects of deep convection on the SEB is demonstrated by computing areal averages over the second and third onset regions.

7.4.1 Surface energy balance of the MCS

The evolution of the area averaged components of the SEB and Q_{net} is shown in Fig. 7.6. Since it is night time locally, the contribution to the SEB by solar radiation is not shown. The two major contributors to Q_{net} in the presence of the MCS are the latent heat flux and the net longwave radiative fluxes (IR down - IR up). The sensible heat flux contribution is relatively small. The constancy with time of the IR up radiative flux is a result of keeping the SST fixed throughout the simulation. A gradual decrease of the latent heat flux occurs because the surface wind speed decreases with time (not shown). Consequently, there is a corresponding reduction in Q_{net}. Young *et al.* (1992) computed the average diurnal cycles of Q_{net} from measurements taken during a pilot cruise over the warm pool. The average value of Q_{net} during the night time varied between 150 - 200 W m^{-2}, and is consistent with our results shown in Fig. 7.6. Thus the model produces ocean residual flux values which compare favorably with observations despite the fact that the SST is fixed in our simulation.

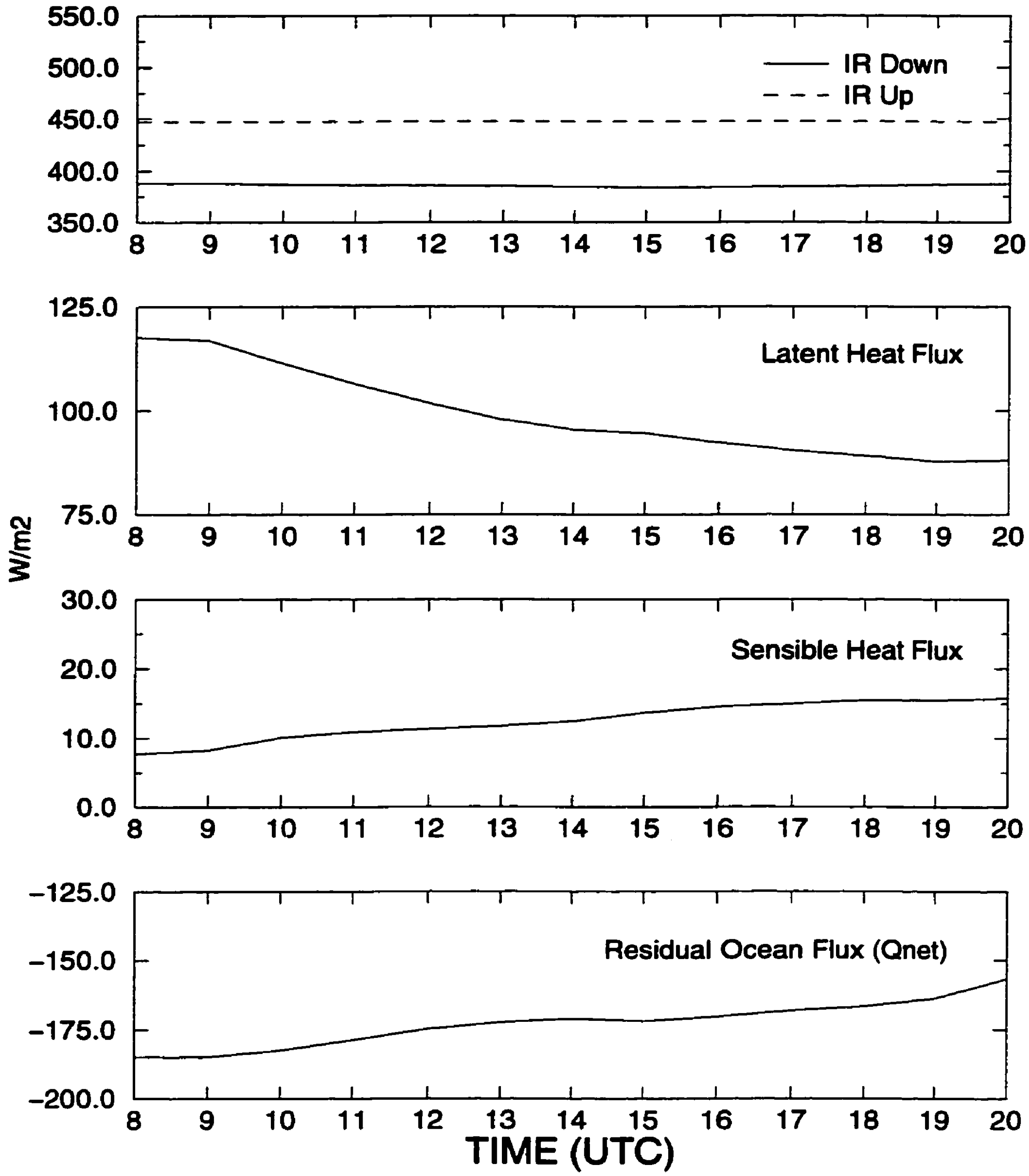

Figure 7.6: The areal averaged (shaded in Fig. 5.3) components of the surface energy balance for the period 0800 - 2000 UTC. The units are W m^{-2}.

7.4.2 Surface energy balance during convective onsets

Young *et al.* (1992) noted that deep convection has a profound impact on most of the SEB components. The cloud cover associated with the convective disturbance reduces the surface solar insolation leading to day-to-day variability in Q_{net}. The surface fluxes of latent and sensible heat increase in the presence of a convective disturbance, due to the convective drying and cooling along with the enhanced surface wind speed from the convective downdrafts.

As mentioned previously, convective onsets are determined using the technique proposed by Sherwood and Wahrlich (1999). These onset regions are associated with MPFs. The MPFs are composed of convective and stratiform precipitation areas (Leary and Houze, 1979). Jabouille *et al.* (1996) demonstrated that the increase in surface fluxes of sensible and latent heat is confined to the gust fronts associated with the outflow from the convective downdrafts. This introduces spatial variability in the horizontal distribution of the surface fluxes. Thus, to demonstrate the impact of deep convection on the various components of the SEB, the various terms in the SEB equation are averaged over the convective areas in the onset region, defined by a threshold reflectivity $Z > 35$ dBz (see section 5.1.3). For the periods when convective activity is absent over the onset regions, the averaging is performed over the entire onset region. This is considered representative given that in the absence of convection, there is little horizontal variability in the distribution of the surface fluxes over the onset area.

Figures 7.7 and 7.8 show the various components of SEB over the second and third convective onset regions, respectively. Figure 7.7d shows that Q_{net} or the loss of energy from the ocean is increased around 1100 and 1700 UTC. At these times the region experiences two separate convective outbreaks, consistent with our findings for the heat and moisture budgets for the MPF (Fig. 7.3). The increased loss from the ocean is mainly due to enhanced surface fluxes of latent and sensible heat (Fig. 7.7b and c). Although longwave downwelling radiation (Fig. 7.7a) also exhibits hour-to-hour variability, the amplitude is much less than the latent and sensible heat fluxes. Again the constancy in the upwelling longwave radiation (Fig. 7.7a) is due to the fixed SST used in the simulation. In short, the residual ocean fluxes are increased around the onset time due to increases in the surface fluxes of latent and sensible heat. An increase of 5-10% at onset time (1100 UTC) occurs relative to the value at 1000 UTC.

The picture is similar for the third onset (Fig. 7.8). We may therefore conclude that the enhanced surface fluxes result in an increased loss of energy from the ocean (1400 UTC). However, the magnitude of the increase for this onset is around 21% compared to the 5-10% observed for the second onset. This difference in magnitude is due to the relatively larger increase in the surface fluxes of the sensible and latent heat for the third onset (Fig. 7.8b and c). The maximum areal average rain rate for the second onset is 2.5 mm h^{-1} (1200 UTC) compared to 4.0 mm h^{-1} for the third onset (1600 UTC). This suggests that the larger energy loss from the ocean during the third onset is associated with stronger convection in this region.

In summary, the SEB is computed during the occurrence of the MCS as well as for the two convective onsets. Despite the fact that the SST is fixed in our simulation, the computed residual ocean flux values compare reasonably well with observed values reported for the warm pool region by Young *et al.* (1992). The latent heat flux and the net longwave radiative fluxes are the two major contributors to the residual ocean flux. Increases in the residual ocean fluxes are noted for the two onsets. These increases arise due to enhanced fluxes of latent and sensible heat which occur in association with deep convection. Little variations with time is evident in the downwelling longwave radiative flux. Stronger convection over the third onset region leads to a larger residual ocean flux relative to the second onset region.

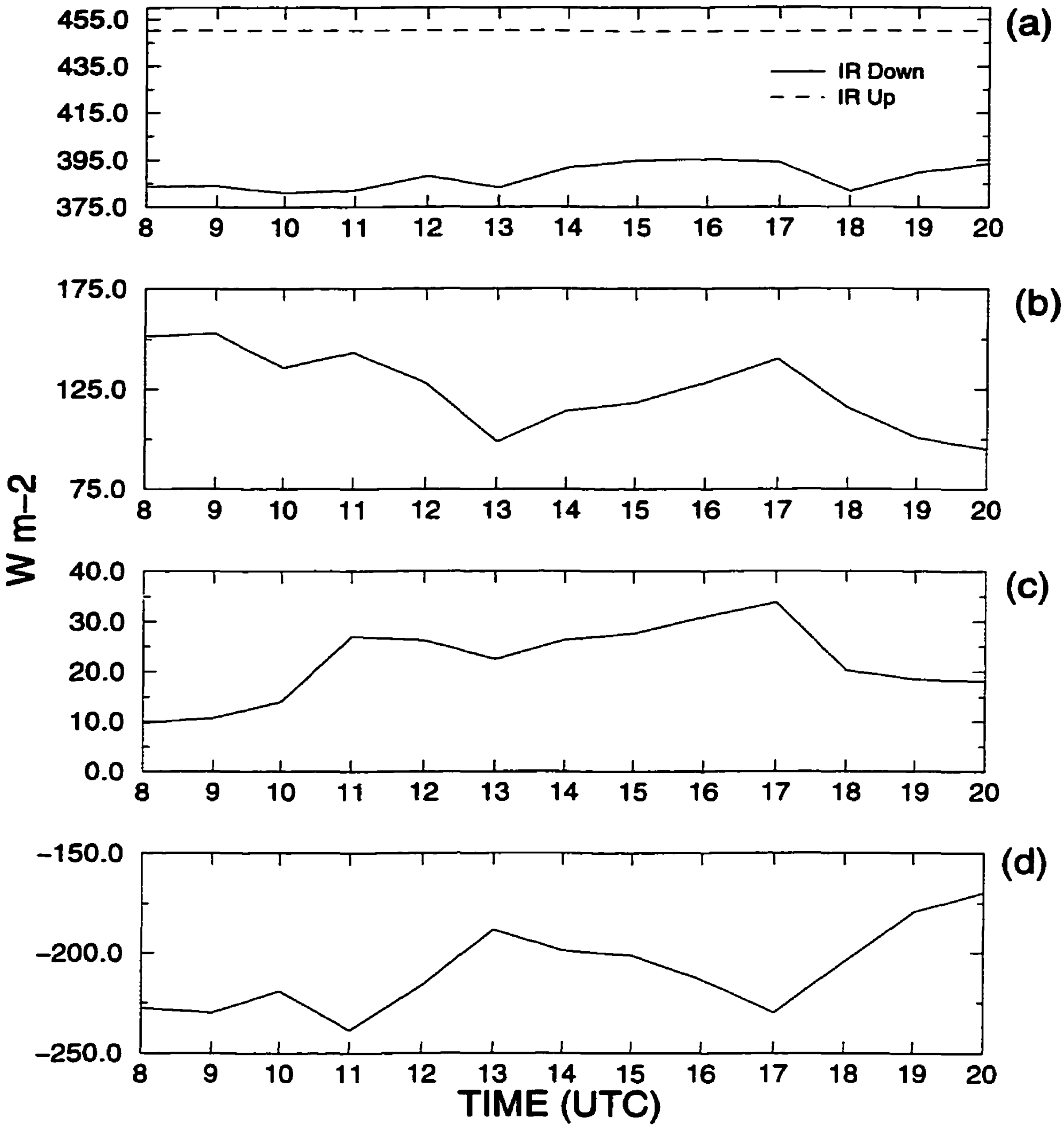

Figure 7.7: The upwelling and downwelling longwave radiative fluxes (a), the latent heat flux (b), the sensible heat flux and (c) the residual ocean flux (Q_{net}) (d) in units of W m^{-2} for the second convective onset region (area B in Fig. 5.7).

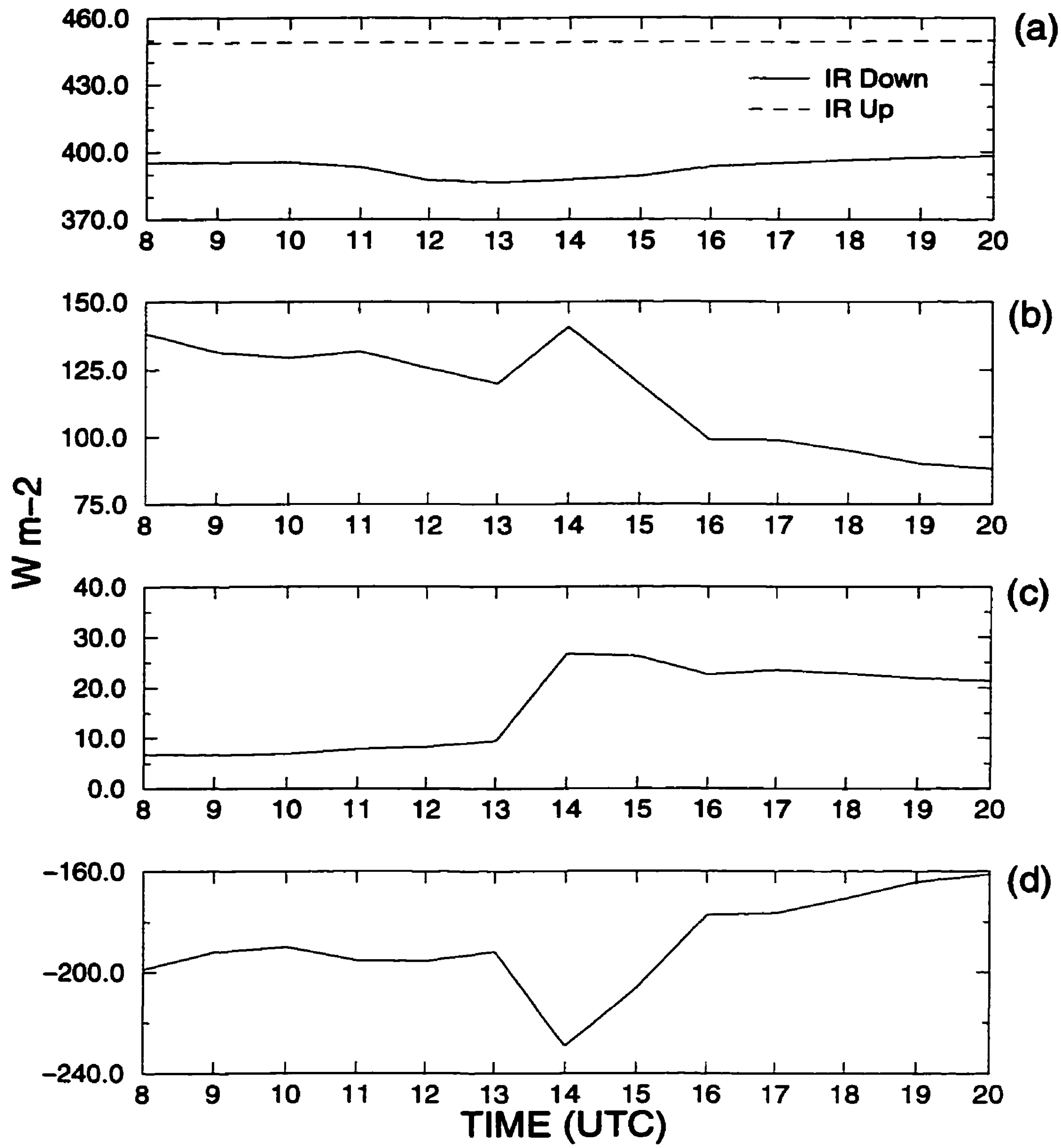

Figure 7.8: Same as Fig. 7.7 but for the third onset region.

Chapter 8

Summary and conclusions

In this thesis, a 16-h meso-β scale (horizontal resolution 20 km) numerical study of the lifecycle of the 15 December 1992 MCS was performed to (a) Simulate realistically the growing and mature stages of the lifecycle of the MCS; (b) Determine the mechanisms that regulate the convective onsets during the lifecycle of the MCS; (c) Study the characteristics of the heat and moisture budgets of the MCS and the associated mesoscale precipitation features and (d) Document the effects of deep convection on the surface energy balance of the underlying ocean.

The MCS under investigation occurred during the Australian monsoon season and two weeks prior to the peak westerly wind bursts. The satellite infrared imagery shows that the growing stage (0530 - 1700 UTC) was marked by the initiation of two entities (S_1 and S_2), which developed individually before merging into a spatially extensive MCS. The mature stage (1700 - 2000 UTC), observed by airborne Doppler radar, shows the presence of two lines (L_1,L_2) of deep convection with their associated stratiform regions to their rear. The region in between L_1 and L_2 showed minimum reflectivity. The stratiform regions exhibited descending motions below 3 km and ascending motion aloft. The decay of the MCS occurred around 2100 UTC when the area-averaged brightness temperature increases rapidly.

To attain a realistic simulation of the lifecycle, we found it necessary to improve the initial moisture field in the ECMWF analysis and refine physical representations in the MC2 model. The initial moisture field improvements address two deficiencies in the ECWMF data: excessive low-level moisture and very dry midlevels. These improvements were confined to locations far away from the MCS and therefore is unlikely to have any impact on the lifecycle of the MCS. In the vicinity of the MCS, low level moistening is introduced at the model initial time (0000 UTC) to reflect diurnal warming of the SST. This change gives rise to higher CAPE at the model initial time and leads to stronger convection in the region occupied by S_1 and S_2.

The refinement of the model physical processes includes subgrid-scale deep convection, surface fluxes and the interaction of solar radiation with ice clouds. Since the MCS evolves nocturnally, solar radiative effects are absent. The convective processes are improved by implementing two additional criteria to the trigger function and the incorporation of a detrainment process for convective rain into the KF CPS. A gustiness parameter for weak surface wind situations and convective gust effects were added to the surface flux scheme.

The model results are compared with measurement from wind profilers and surface fluxes estimated from the TAO buoy data. The model-simulated wind profiles between 0400 - 2000 UTC are verified against wind profiler measurements at Kavieng and Kapingamarangi. The simulated winds agree to within 1-2 m s^{-1} with the observed. The backing of the winds above 700 hPa between 0600 - 1000 UTC over Kavieng is also captured by the model and was associated with the westward migration of the transequatorial flow. The model-simulated surface fluxes of latent and sensible heat compare fairly with the estimated fluxes from the buoy data. During deep convection, maximum enhancements of 3 times for the sensible heat flux and 2 times for the latent heat fluxes are noted, in agreement with the findings of Jabouille *et al.* (1996). The increase in sensible heat flux is caused by the combined effects of cooling due to convective downdrafts and the increased surface wind speed associated with the gust front. Likewise, the increase in the latent heat flux is related to the drying effects of convection and the increase in surface wind speed associated with the gust fronts. The enhancement of the fluxes is only evident after convective gust effects were incorporated into the surface flux scheme. This result suggests the need to parameterize convective momentum transport to obtain realistic surface wind enhancements by convective downdrafts.

The simulated MCS was verified against satellite data during the growing stage. Good agreement was found in the evolution of the simulated anvil cloud fraction. Since most of the anvil cloud originates from the detrainment of ice particles from deep convection, the good agreement with the observations indicates a realistic evolution of deep convection in the model. Similar to the observations, the growing stage was composed of three convective onsets occurring at 0600, 1100 and 1400 UTC. The onsets were governed by the existence of upward vertical motions, moderate CAPE and a favorable surface potential temperature dropoff (SPTD, section 4.2.1). The first convective onset occurs in a region characterized by the existence of CAPE, a favorable SPTD and large-scale ascent associated with the transequatorial flow. The second onset, although located in a region of CAPE and vertical motion associated with a confluence zone, is basically governed by the development of a favorable SPTD from the vertical advection of low potential temperature air in the ABL in the confluence zone. The third onset lies in a region of moderate CAPE and favorable SPTD. It is regulated by the evolution of the large-scale vertical motion controlled by the presence of a quasi-2-day wave.

The convectively generated mesoscale forcing associated with the third onset is responsible for the merger of the entities S_1 and S_2. To test the hypothesis of Mapes (1993) that such mergers are caused by gravity waves emanating from deep convection, a DRY simulation was performed. It was found that the evolution of the low-level vertical motion preceding the third onset was similar in both the DRY and CONTROL simulations, suggesting that the Mapes mechanism was not operative.

The simulated mature stage of the MCS lifecycle was verified against Doppler radar data. The model-simulated maximum reflectivity was between 35-40 dBz against the observed maximum values of 40-45 dBz. The two convective lines L_1 and L_2 observed during the mature stage are well simulated by the model. The lines formed in two separate confluence zones. The orientation and strength of L_1 is reproduced by the model. Although L_2 is less well simulated in intensity and structure, the horizontal distribution of surface precipitation matches the observed. A comparison of the simulated 500-m wind speeds with those retrieved from the Doppler radar data reveals that the model winds are underestimated by about 50%. This is due to the lack of momentum transport by cumulus convection in the KF CPS. A comparison of the DRY and CONTROL simulations suggests that the formation of L_1 is controlled by mesoscale circulations induced by deep convection in its vicinity.

The model simulated lifecycle is realistic with a reasonable reproduction of the growing and mature stages. Much of the success in the numerical simulation depends on incorporation of suitable trigger mechanisms for deep convection in the KF CPS. The sensitivity of the simulated results to the two additional criteria introduced into the Kain-Fritsch Trigger (KFT) function was tested. A comparison of the simulation with the original KFT function and the SPTD criterion with the CONTROL simulation indicates that SPTD was largely responsible for the successful prediction of the lifecycle of the MCS. However, inclusion of the deep column ascent criterion yields a better timing for the onset of the mature stage (at 1700 UTC). Thus, a combination of the original KFT function with SPTD and the deep column ascent criteria for convective initiation in the model is necessary to successfully simulate the lifecycle of the MCS.

The impact of the MCS on the larger-scale environment is studied through the heat and moisture budgets. The areal-averaged heat and moisture budgets for the MCS and the embedded MPFs were characterized by two heating and drying peaks (300 hPa and 925 hPa) with cooling and moistening occurring at midlevels (450 - 700 hPa). The low-level heating and drying were associated with deep convection while the upper level heating and drying were the result of deep convection and the vapor deposition process on ice crystals. The midlevel cooling and moistening arose due to sublimation of ice crystals above the freezing level and evaporation/melting of rain/ice below the freezing level. These results were consistent with the previous findings by Nitta (1977), Lewis (1975) and Nuret and Chong (1998). As the MCS evolved, the magnitudes of the heating and moistening increased due to the increase in the area occupied by deep convection. Following the convective onsets, the ABL eddy processes restored the ABL to a state to support again deep convection. The recovery time of nearly 8 h is consistent with the findings of Raymond (1995). These eddy processes represent a response to the cooling and drying effects of deep convection and caused an increase in the transfer of sensible and latent heat from the ocean surface.

The impact of deep convection on the surface energy balance (SEB) was also investigated. The SEB components were computed during the occurrence of the MCS and for the second and third convective onsets. Despite the fact that the SST was fixed in our simulation, the computed residual ocean flux (energy lost by the ocean) values compared reasonably well with observed values reported for the warm pool region by Young *et al.* (1992). The latent heat flux and the net longwave radiation were the two largest components in the SEB for the MCS and the two onsets. During the two onsets, the net longwave radiative flux remained essentially unchanged but the latent and sensible heat fluxes increased. The enhanced surface fluxes during the onsets increased the residual ocean fluxes, particularly over the region occupied by the third convective onset.

In conclusion, while this study attempted to fill the gap that exists in the literature on the lifecycle of the warm pool MCSs, clearly much remains to be done if all the remaining goals of COARE are to be attained. Godrey *et al.* (1998) in their COARE interim report suggested the need to produce high resolution surface flux maps and wind fields to force ocean models that seek to replicate the response of the upper ocean. During COARE, observations from a variety of platforms were gathered and the assimilation of these observations using fine resolution NWP models remains. This study suggested that appropriate specification of the initial moisture field and suitable convective trigger mechanisms can help in the attainment of these goals. Given the diverse modes of convective organization observed over the warm pool, future studies should include other case studies.

Regulation of warm pool convection has been associated with low-level convergence and/or viewed as a response to the large-scale destabilization of the environment (Raymond, 1995). Studies during GATE and TOGA COARE also noted the importance of boundary layer processes on the control of convection (Garstang and Betts, 1974; Raymond, 1995). On timescale of half a day, warm pool convection is regulated by boundary layer equivalent potential temperature budget. In the present study, the mechanisms that regulate convective onsets over the warm pool were shown to depend on three factors: the large-scale ascent, CAPE and favorable SPTD. These factors provide possible precursors for the onset of deep convection over the western Pacific region and new convective initiation mechanisms to be included in numerical weather prediction models.

Jabouille *et al.* (1996) quantified the convective effects on the surface fluxes of sensible and latent heat for deep convection organized as squall lines. Godrey *et al.* (1998) questioned the validity of the representativeness of the results given the diverse modes of convective organization. Grant and Hignett (1998) noted the lack of measurements of the SEB components during the occurrence of MCSs. In the present study, we documented the deep convective effects associated with the MCS and the embedded MPFs on the surface fluxes and our results are consistent with those reported by Jabouille *et al.* (1996). One of the drawbacks of the simulation was that the SST is fixed. Clearly future modeling studies of the SEB should allow for a two-way interaction between the lower atmosphere and the sea surface in order to realistically simulate the convective effects on the surface exchange processes.

Appendix A

Model Description

A.1 Introduction

The Mesoscale Compressible Community model (MC2) is based on the fully elastic non-hydrostatic model of Tanguay *et al.* (1990). The model employs efficient numerics and allows simulation of weather phenomena over a wide range of scales (Benoit *et al.*, 1997; Robert, 1993). The dynamical and physical aspects of the model will be described, separately. The modified model equations, its numerics and the various steps involved in its forward integration in time will be presented. A brief description of the physics package used and a detailed description of the cumulus parameterization for deep and shallow convection are presented. As described in Chapter 4, some physical processes have been modified for the present simulation. The readers are referred to Chapter 4 for details of these modifications.

A.2 Model equations

The Euler equations for a gaseous flow on a rotating sphere expressed in a conformal projection are:

$$\frac{dU}{dt} = fV - K\frac{\partial S}{\partial X} - RT\frac{\partial q}{\partial X} + F_x \tag{A.1}$$

$$\frac{dV}{dt} = -fU - K\frac{\partial S}{\partial Y} - RT\frac{\partial q}{\partial Y} + F_y \tag{A.2}$$

$$\frac{dw}{dt} = -g - RT\frac{\partial q}{\partial z} + F_z \tag{A.3}$$

$$(1-\alpha)\frac{dq}{dt} = -S\left(\frac{\partial U}{\partial X} + \frac{\partial V}{\partial Y}\right) - \frac{\partial w}{\partial z} + \frac{L}{T} \tag{A.4}$$

$$\frac{dT}{dt} = \alpha T\frac{dq}{dt} + L \tag{A.5}$$

$$\frac{dq_v}{dt} = E \tag{A.6}$$

$$\frac{dq_c}{dt} = S_C \tag{A.7}$$

$$\frac{dq_r}{dt} = S_R \tag{A.8}$$

$$\frac{dq_i}{dt} = S_I \tag{A.9}$$

Eqns. (A.1)-(A.9) represent the modified version of the original system of equations proposed by Tanguay *et al.* (1990). The original system of equations comprised of (A.1)-(A.7) with T representing temperature.

The variables are:

X, Y : coordinate distances on a conformal projection surface (e.g. polar stereographic or Mercator)

U : X - component of the map wind

V : Y - component of the map wind

w : z - component of wind

q_v : water vapor mixing ratio $(\frac{kg}{kg})$

q_c : cloud liquid water mixing ratio $(\frac{kg}{kg})$

q_r : rain mixing ratio $(\frac{kg}{kg})$

q_i : ice mixing ratio $(\frac{kg}{kg})$

q : $\ln\left(\frac{p}{p_o}\right)$, where p is the pressure and $p_o(10^5$ Pa) is a constant

T : virtual temperature, the subscript is dropped for convenience

K : $\left(\frac{U^2+V^2}{2}\right)$ is the specific pseudo kinetic energy

S : m^2 , the metric projection term

m : $\left(\frac{1+\sin\phi_o}{1+\sin\phi}\right)$, for a polar stereographic (PS) projection and $\frac{\cos\phi_o}{\cos\phi}$ for Mercator projection(MP)

ϕ_o is the reference latitude set to 60° for PS and 0° for MP and ϕ is the latitude.

f : Coriolis parameter.

Physical forcings :

F_x, F_y, F_z : sources and sinks of momentum along X,Y, and z directions.

L : Heat sources and sinks in the thermodynamic equation.

E, S_C, S_R, S_I : sources and sinks for water vapor, cloud liquid water, rainwater and ice respectively.

Constants :

g : Acceleration due to gravity.

R : gas constant for dry air.

α : $\frac{R}{C_p}$,where C_p is the specific heat of air at constant pressure.

The total derivative in conformal coordinates is defined as

$$\frac{d}{dt} = \frac{\partial}{\partial t} + S\left(U\frac{\partial}{\partial X} + V\frac{\partial}{\partial Y}\right) + w\frac{\partial}{\partial z} \tag{A.10}$$

where (U, V) are defined in terms of (u, v), the winds with respect to a local Cartesian coordinate system as :

$$\begin{pmatrix} U \\ V \end{pmatrix} = \frac{1}{m}\begin{pmatrix} -\sin\lambda & -\cos\lambda \\ \cos\lambda & -\sin\lambda \end{pmatrix}\begin{pmatrix} u \\ v \end{pmatrix} \tag{A.11}$$

where λ is the longitude.

The actual vertical coordinate used, Z, is a variant of the terrain following Gal-Chen coordinate(ζ), defined as

$$\zeta(X, Y, z) = \left(\frac{z - h_o}{H - h_o}\right) H \tag{A.12}$$

By defining Z$[\zeta(X, Y, z)]$, a variable resolution can be used in the vertical, h_o is the height of the topography, and H is the height of the model top.

The use of virtual temperature in equations (A.1) - (A.5) implies the that effect of moisture is included in the computation of air density. To cast the thermodynamic Eq. (A.5) in terms of virtual temperature, we used the approximation as in (Belair, 1996):

$$\frac{R}{C_p} = \frac{R_d}{C_{pd}}(1 - 0.2q_v) \approx \frac{R_d}{C_{pd}} \tag{A.13}$$

where $R = R_d(1 + 0.6q_v)$ and $C_p = C_{pd}(1 + 0.9q_v)$. For $q_v \leq 40$ g kg^{-1} the error of approximating R/C_p by R_d/C_{pd} is $\leq 1\%$.

The term L in the equation (A.5) represents the temperature tendency due to physical processes like convection, large scale condensation, radiation and atmospheric boundary layer processes.

A.3 Numerical Aspects

The MC2 model is a nested grid point model and derives its lateral boundary conditions from a previous model run or the large scale analysis. The Davies (1976) relaxation boundary condition is imposed. Such an approach for a nested grid point regional forecast model was illustrated in the study by Yakimiw and Robert (1990). The model permits vertical nesting below the model lid. The boundary condition uses an attenuation function, varying between 0 and 1 in the sponge (nesting) zone, and is a quadratic function of the vertical coordinate Z.

The terms responsible for gravitational and acoustic oscillations are treated semi-implicitly. To facilitate this, an isothermal basic state atmosphere in hydrostatic equilibrium is defined. The variables q and T are partitioned into a basic and a perturbation part (q', T'). The basic state is given by:

$$T_* = 273.16°K \tag{A.14}$$

$$q_*(z) = q_\circ - \frac{gz}{RT_*} \tag{A.15}$$

where $q_\circ = \ln(p_\circ)$.

Implicit treatment then consists of time averaging over the Lagrangian displacement of the terms associated with gravitational and acoustic oscillations. The time average is off centered as suggested by Tanguay *et al.* (1992). This eliminates problems of numerical instability due to topography. In MC2, spurious resonance that may develop in mountainous regions for Courant numbers larger than unity are mitigated by the application of spatially-averaged Eulerian treatment of topography proposed by Ritchie and Tanguay (1996). It means the explicit appearance of the horizontal derivatives of the topography on the right hand side of the continuity equation and thermodynamic equation. These derivatives are computed in an Eulerian framework. (e.g in the $\frac{\partial T'}{\partial t}$ and $\frac{\partial q'}{\partial t}$ equations for perturbation temperature and perturbation pressure respectively, the term $F_1U + F_2V$, where

$$F_1 = \frac{1}{g_{OH}}\frac{\partial h_0}{\partial X} \text{ and } F_2 = \frac{1}{g_{OH}}\frac{\partial h_0}{\partial Y}$$

appears explicitly. These metric terms are treated using centered finite differences and constitute an explicit treatment of the mountains).

Time discretization is attained by the use of a second-order time difference scheme along the Lagrangian trajectory. The non-linear terms on the right hand sides of the system are evaluated at time t as a spatial average of values at the two extremities of the Lagrangian displacement. The temporal and spatial discretization of the equations leads to a coupled system. Solving the system for the variable q' yields a Helmholtz equation. The Helmholtz equation is solved using the alternating-direction implicit method (Peaceman and Rachford, 1955). With q' known at the next time step, all the dependent variables are updated as follows. In the first step, the tendencies due to physical processes (e.g. ABL transport, convection, condensation and radiation) are set to zero and the Helmholtz equation for perturbation pressure is solved. The dependent variables are then updated. In the second step, the respective tendencies due to all physical processes are applied through process splitting technique by invoking the RPN[1] physics package (Mailhot, 1994). In the third step, horizontal diffusion (Jakimow *et al.*, 1992) is applied to all the fields (prognostic) followed by the application of the Robert time filter (Asselin, 1972). The flow chart of the time integration process is shown schematically in Fig. A.1

A.4 Model Physics

Model physics constitutes the representation of physical processes unresolved by finite grid size. Invoking the RPN package returns time tendencies of the dependent

[1]Recherche en Prévision Numérique

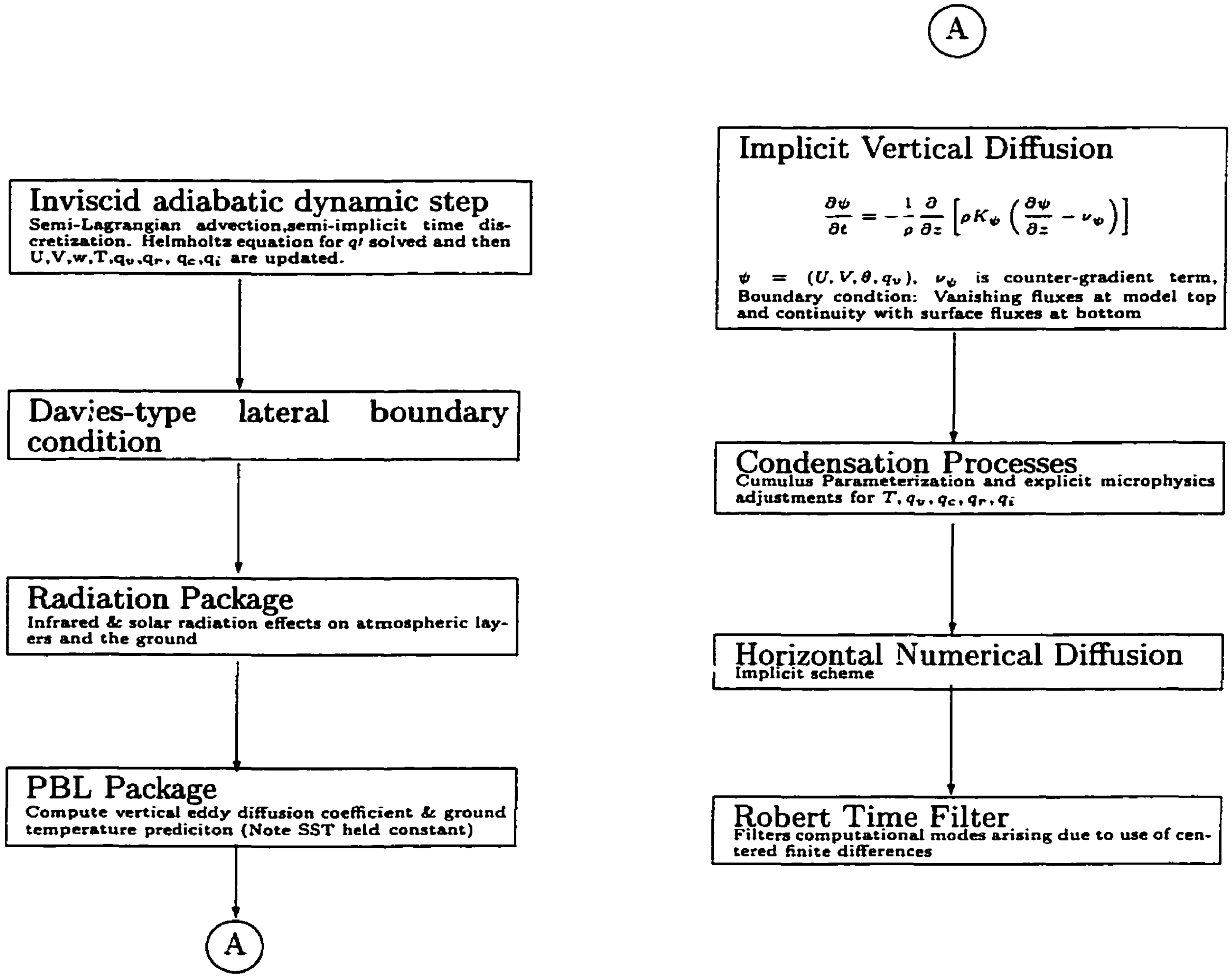

Figure A.1: The flow chart of MC2 model illustrating the time integration process.

variables $(U, V, T^2, q_v, q_c, q_r, q_i)$ associated with different physical processes. These processes include atmospheric surface layer (ASL) exchanges, atmospheric boundary layer (ABL) turbulent transfer (also referred to as vertical diffusion), ground temperature prediction to capture the diurnal cycle, solar and infrared radiation heating, cooling and their interaction with clouds, deep and shallow convective processes, the drag effects due to the breaking of orographically excited gravity waves (or the gravity wave drag) and explicit prognosis of cloud liquid water, rain mixing ratio and ice mixing ratios (or the explicit microphysics). In this section, the salient features of each process will be described.

A.4.1 Atmospheric boundary layer process

The ABL transport, developed by Benoit *et al.* (1989), is treated in terms of an eddy vertical diffusion. The surface fluxes of heat and moisture provide the lower boundary condition and the turbulent fluxes vanish at the model top.

$$\frac{\partial \psi}{\partial t} = -\frac{1}{\rho}\frac{\partial}{\partial z}\left[\rho K_{\psi}\left(\frac{\partial \psi}{\partial z} - \nu_{\psi}\right)\right] \tag{A.16}$$

$$K_{\psi} = \frac{c\lambda\sqrt{E}}{\phi_{\psi}} \tag{A.17}$$

where

$\psi = (U, V, q_v, \theta)$

ρ = density of air

ν_{ψ} = counter gradient term

c is a constant set to 0.5 and λ is the mixing length.

The ABL depth is determined on the basis of the θ_v profile. The vertical diffusion coefficient (K_{ψ}) is a function of the turbulent kinetic energy (E) and the stability of the ABL (ϕ_{ψ}), defined in terms of the gradient Richardson number.

[2]Hereafter refers to temperature

Surface layer fluxes of heat, moisture and momentum are expressed in the form

$$-\overline{w'\psi'} = c_\psi u_* (\psi_a - \psi_s) \qquad \text{(A.18)}$$

where ψ' can be perturbations in T, q_v, U and V. u_* is the frictional velocity and the subscripts a, s refer to atmosphere and surface, respectively. The transfer coefficient c_ψ is a function of stability and roughness length z_o.

Turbulent mixing in the free atmosphere may arise in regions of strong vertical wind shear. These situations are addressed in the vertical diffusion scheme whose diffusion coefficient is dependent on the gradient Richardson number.

A.4.2 Infrared radiation

The infrared radiation scheme is based on a broad-band model proposed originally by Garand (1983) and improved by Garand and Mailhot (1990). The scheme takes into account the radiative effects of water vapor, carbon-dioxide, ozone and clouds. The broad-band model is comprised of four spectral bands. The four bands are defined as 1000-700, 580-640, 640-700 and 700-760 cm^{-1}. It may be mentioned that water vapor is concurrently active along with CO_2 and O_3 in all the 4-bands.

Precomputed transmission functions are used for computational efficiency. The variation of the absorption coefficient with temperature is taken into account in the scheme. The transmission function is simplified by the application of the strong line approximation. Specifically, the approximation leads to a definition of absorber mass that is band independent. However, Garand (1983) showed errors in absorber mass for weak absorption bands. The strong line approximation reduces the absorber mass in the weak absorption bands, resulting in erroneous transmission through these bands. Correction in the absorber mass is effected by an empirical fit for each band between the true absorber mass and the strong line approximation absorber mass. The corrections are applied to O_3 and H_2O.

Anomalous absorption of infrared radiation is associated with the presence of water vapor in the 8-13 μm atmospheric window region. This effect is referred to as the 'e - type' absorption, because the effect is directly proportional to the partial pressure of water vapor. As Garand (1983) showed, this effect is especially important in yielding lower IR cooling rates in warm humid regions such as the tropics and is expected to be predominant close to the surface where the highest water vapor mixing ratios occurs. This effect is parameterized in the present scheme.

In the presence of clouds, the transmission of IR radiation between model levels is reduced. The reduction is expressed in terms of cloud transmission through a layer defined as (1-ϵC) where ϵ is the cloud emissivity and C is the cloud fraction. ϵ is assumed to be independent of the frequency and is set to a value of 0.95 except at temperatures below 200 K and above the σ = 0.1 level where it is set to 0.50. Maximum overlap is assumed for adjacent cloudy layers (i.e. cloud fraction is the maximum value that occurs in these adjacent layers). Random overlap is assumed for cloud layers separated by clear ones.

A.4.3 Solar radiation

Transfer of solar radiation through the earth's atmosphere undergoes scattering by air molecules, aerosols and cloud drops. Solar radiation is absorbed by gases (water vapor, CO_2 and ozone) and cloud droplets. The process of atmospheric absorption and scattering of solar radiation is parameterized following Fouquart and Bonnel (1980). The scheme also accounts for the interaction between scattering and molecular band absorption.

The absorption of solar radiation in the atmosphere is primarily due to water vapor and ozone. Carbon-dioxide absorption is significant in the upper troposphere. The gaseous absorption are expressed in terms of transmission functions and appear as Pade approximation coefficients. The coefficients are specified separately for each gas. The absorption of solar radiation by liquid water is very small in the visible part of the spectrum but can be significant in the near infrared region. Since 30% of the incoming solar flux lies in the 1-4 μm range, cloud droplet absorption is expected to be significant. This is represented in terms of an equivalent single scattering albedo expressed as a function of optical thickness (τ) using an empirical relationship for $0 \leq \tau \leq 20$.

Rayleigh scattering by air molecules contributes a significant part to the planetary albedo. The reflectivity(R) and transmissivity(T_r) of each air-layer is approximated by $R = \frac{0.5\tau_a}{\mu_o + \tau_a}$ and $T_r = 1 - R$, respectively, where τ_a is the optical depth of the atmosphere (typically $\tau_a \approx 0.06$) and μ_o is the cosine of the solar zenith angle. Multiple reflections between successive layers are taken into account. It is well known that the presence of clouds increases the albedo. The cloud reflectivity and transmissivity are computed on the basis of the cloud optical thickness and scattering phase function. The cloud optical depth is defined as $\tau_{cld} = \frac{3}{2}\frac{LWC}{\rho r_e}$, where LWC is the total liquid water content in the column, ρ is the density of air and r_e the effective radius of cloud droplets. The LWC is computed by a method suggested by Betts and Harshavardhan (1987) and $r_e = 10\mu m$ for ice particles. Thus, clouds are characterized by single scattering albedo, asymmetry parameter and cloud optical depth. The reflectivity and transmissivity are computed as a function of solar zenith angle using the Delta Eddington approximation. The scheme yields a large transmitted flux for optically thin clouds.

In the infrared region (1 - 4μm) of the solar spectrum, there exists numerous absorption bands of water vapor and carbon-dioxide. Thus, absorption occurs along with scattering. This interaction between scattering and absorption reduces to a problem of determining the exact amount of absorber along the light path. This is determined by the method of distribution of photon paths (Fouquart and Bonnel, 1980).

A.4.4 Deep and shallow convection

Deep and shallow convective processes occurring in the real atmosphere are usually unresolved by grids employed in most numerical weather prediction (NWP) models. Thus, the effects of convection have to be parameterized in terms of resolved-scale variables. A variety of cumulus parameterization schemes (CPS) have been developed for different horizontal grid resolutions. For instance, large-scale NWP models with grid sizes around 50-100 km often employ the Kuo, Betts-Miller (BM) or the Arakawa-Schubert (AS) schemes. At the mesoscale, models with grid sizes around 20-25 km may employ the Fritsch-Chappel (FC) and Kain-Fritsch (KF) schemes.

A.4.4.1 Betts-Miller scheme

In the Betts-Miller scheme, the sub-grid scale effects of convective clouds are represented by adjusting temperature and moisture profiles to the observed quasi-equilibrium structures for deep convection and to a mixing line structure for shallow convection. Quasi-equilibrium between the cloud field and the large-scale forcing forms the basis of representing deep convection in the BM scheme. Quasi-equilibrium means that the convective cloud field constrains the thermal and moisture structure of the atmosphere against the destabilizing influence of the large scale flow. The concept has been found to be valid on large spatial and temporal scales. The effects of shallow convection is viewed as a mixing process between the surface layer air and the free atmosphere.

Observational basis for deep convection

The thermodynamics of the BM scheme is based on the saturation point formulation as reported in Betts (1982). The saturation point (sp) is defined as the temperature and pressure (T^*, p^*) at the lifting condensation level (LCL). The subsaturation parameter P is the difference between air parcel saturation level pressure and the actual pressure level i.e. $P = p^* - p$. Betts (1986) observed that temperature profiles below the freezing level in deep convection is parallel to the θ_{ESV} isopleth, where θ_{ESV} is defined as a constant virtual equivalent potential temperature. This led to the proposal that the reference lapse rate in the lower-troposphere is moist virtual adiabatic rather than the widely accepted moist adiabat. Since the slope of the θ_{ESV} isopleth is 0.9 times that of the moist adiabat, the air parcel buoyancy reduction due to cloud water content is accounted for. This reference structure in the presence of deep convection is universal as reported by Betts (1986) for the cases of hurricanes, GATE slow and fast moving squall lines and Venezuela convective episodes. Thus, the reference structure below 600 hPa or the freezing level is the θ_{ESV} with θ_{ES} constrained to a minimum at 600 hPa. Above 600 hPa the observed thermal profile increases to cloud top θ_{ES} value. Considerable variability is associated with the observed moisture structure. Despite this a reference moisture profile is specified in the scheme.

Observational basis for shallow convection:

A shallow cumulus cloud field is regarded as a mixing process between the surface layer air and the free atmosphere. This mixing is characterized by a mixing line. Thus when two air parcels mix in the vertical, the *sp* of every possible mixture lies on the mixing line joining the *sps* of the two parcels. This mixing line structure for shallow cumulus convection was highlighted by Betts (1982) by plotting *sps* between 900-700 hPa and the *sps* were found to lie close to the line joining the *sps*. This evidence was presented for the undisturbed trade wind region and tropical land stations.

Reference profiles for deep convection:

The scheme involves a lagged adjustment of the resolvable-scale T and q_v profile towards a reference quasi-equilibrium structure in the presence of grid-scale radiative and advective processes. The reference T, q_v profiles for deep convection are based on the observation that θ_{ES} (at cloud base) decreases with height upto the freezing level (while being parallel to the θ_{ESV} isopleth) and increasing to θ_{ES} of the environment near the cloud top. The first guess temperature profiles are constructed using

$$\theta_{ES}(p) = \theta_{ES}(B) + \alpha V\left(p - p_B\right) \text{ for } p_B > p > p_M \tag{A.19}$$

where V is the vertical lapse rate of θ_{ESV}, α is the weighting factor set to 1.5 based on the GATE data set and

$$\theta_{ES}(p) = \theta_{ES}(M) + \left(\theta_{ES}(T) - \theta_{ES}(M)\right)\left(\frac{p - p_T}{p_M - p_T}\right) \text{ for } p_T < p < p_M \tag{A.20}$$

where $\theta_{ES}(T)$ is the environmental saturated equivalent potential temperature at cloud top and $\theta_{ES}(M)$ is the minimum saturated equivalent potential temperature at the freezing level.

The moisture profile is found by specifying the $P = p^* - p$ parameter at three levels (i.e., at the cloud base $P_B = -3875$ Pa, at the freezing level $P_M = -5875$ Pa and at the cloud top $P_T = -1875$ Pa) with linear gradients in between. While the temperature profiles show greater universality, the observed moisture profiles exhibit considerable variability. The above pre-specified profile defined by P_B, P_F and P_T corresponds to a mean profile observed in the tropics. (In the present simulation the average moisture structure is representative of the GATE region squall lines.)

The first guess temperature and moisture profiles are corrected to satisfy the total enthalpy constraint

$$\int_{p_0}^{p_T} \left(k_r - \overline{k}\right) dp = 0 \tag{A.21}$$

where $k_r = C_p T_R + L q_R$ and T_R, q_R are the first guess reference temperature and specific humidity, respectively. $\overline{k} = C_p \overline{T} + L \overline{q}$, $\overline{T}, \overline{q}$ are the grid mean temperature and specific humidity, before the onset of deep convection.

Reference profiles for shallow convection

The first guess profiles for temperature and specific humidity are constructed from properties of the air at the cloud base (pressure p_B) and air above the cloud top (pressure p_T^+). Equal quantities of air from p_B and p_T^+ are mixed and the corresponding sp (i.e., level 1) determined. The slope of the mixing line is found as

$$M = \frac{\theta_E(1) - \theta_E(B)}{P_{SL}(1) - P_{SL}(B)} \tag{A.22}$$

where B corresponds to the cloud base and P_{SL} is the pressure at saturation levels (i.e., for parcels from cloud base B and the air mixture between p_B and p_T^+). The temperature profile (reference) is parallel to the mixing line and is given by

$$\theta_{ES}(p) = \theta_{ES}(B) + M(p - p_B) \tag{A.23}$$

$\theta_{ES}(p)$ is inverted to yield T and p, which with the subsaturation parameter (at level 1) gives sp and q_v.

The first guess reference T and q_v profiles are corrected to satisfy the following energy constraints:

$$\int_{p_B}^{p_{T+1}} C_p \left(T_R - \overline{T}\right) dp = \int_{p_B}^{p_{T+1}} L \left(q_R - \overline{q}\right) dp = 0 \tag{A.24}$$

Adjustment time τ:

The adjustment time (τ) in the scheme is set such that the atmosphere nearly saturates on the grid scale in the presence of a convective disturbance. According to Betts and Miller (1993), in the T106 resolution ($\approx$ 1.125°) model, τ for deep convection and for shallow convection is 2 h. Betts (1997) expressed τ as a function of horizontal scales. He found τ to lie between 40-80 min for the T106 resolution model. For Δx = 60 km, τ lies between 20-40 min. In the present simulation we employ τ = 55 min for deep and shallow convection at Δx = 60 km resolution.

A.4.4.2 Kain-Fritsch scheme:

The KF scheme was designed primarily to facilitate numerical simulation for grid sizes of about 20-30 km. At these grid sizes the cumulus parameterization problem is reduced to the incorporation of the effects of convective clouds. Thus, if cumulus convection is parameterized, the resolvable scales are assumed to develop mesoscale heat, mass, moisture and momentum transports. The fundamental closure assumption employed in the KF scheme is the removal of CAPE in a grid element by convection in one advective time period. The various components in the KF scheme include an entraining-detraining plume model of convective updrafts, convective downdrafts, the convective trigger function responsible for initiating the scheme at a grid point, precipitation formation process, determination of the convective time scale τ (the adjustment time) and hydrometeor generation and their feedback to resolvable scales. The various components will be briefly summarized in this section.

The updraft model:

As horizontal resolution approaches meso-γ scales (2-20 km), convection in each grid box may be characterized by a single type of cloud. Therefore, the KF scheme employs a one-dimensional entraining- detraining plume (ODEDP) model to represent updrafts. In 1-D plume models of updrafts the heating rate is proportional to the product of mass flux and the static stability as shown by Frank and Cohen (1985).

In the ODEDP model, mixing occurs between cloudy and clear environmental air near the cloud periphery resulting in mixtures of clear and cloudy air. It is assumed that negatively buoyant mixtures detrain and positively buoyant mixtures entrain. This mechanism allows cloud parcels to interact with the environment. The rate at which environmental air mixes with the updraft air (the entrainment rate) is given by Kain and Fritsch (1990) as

$$\delta M_e \ (\mathrm{kg\ s^{-1}}) \ = M_{uo}\left(-0.03\frac{\delta p}{R}\right) \tag{A.25}$$

where M_{uo} is the updraft mass flux rate at cloud base, δp is the pressure interval between model levels and R is the plume radius. The constant 0.03 has units of m $\mathrm{Pa^{-1}}$. The above relation implies that a purely entraining plume with an initial radius of 1500 m would double its mass flux after ascending 500 hPa.

Mixing at the cloud periphery results in mixtures containing various proportions of clear and cloudy air. The partitioning of these mixed-parcels into entraining and detraining components is determined by specifying a Gaussian distribution for the frequency of occurrence of various mixtures. Conservation of θ_e and total water substance is assumed during mixing.

The downdraft model:

In the KF scheme, the downdrafts are driven by the negative buoyancy arising due to the evaporation of cloud and rain drops falling from the updraft. The downdrafts originate at the level of free sink (LFS), which is defined as the level where equal amounts of updraft and environmental air, when brought to saturation gives a temperature less than the environmental temperature. The LFS occurs typically around 500 hPa. The downdraft is assumed to sink with an initial downward velocity of 1 m $\mathrm{s^{-1}}$, with the velocity at lower levels given by the buoyancy equation. The downdraft descends with a constant relative humidity of 100% in the cloud layer and 90% below cloud base until the level where it attains positive buoyancy. The thermodynamic structure is given by the conservation of θ_e (adjusted for melting). The downdraft mass flux is set to the maximum transfer of mass from the updraft that can be maintained at a specified constant relative humidity and over the estimated depth (between the surface and LFS) for the given available liquid water.

Precipitation formation process:

As the updraft parcel ascends, in each cloud layer, the condensate produced depends on the decrease in updraft saturation mixing ratio. Some of the condensate evaporates due to entrainment of environmental air. The condensate left after evaporation to maintain saturation of the updraft parcel is the total cloud liquid water content (q_c^{KF}).

Below the freezing level between -5 to -15°C, a linear transition in θ_e with respect to water to θ_e with respect to ice is employed by varying the latent heat of condensation and fusion and the mixing ratio as

$$L = (1 - \gamma)\, L_v + \gamma L_s \tag{A.26}$$

and

$$\gamma = (1 - \gamma)\, r_{sl} + \gamma r_{si} \tag{A.27}$$

in accordance with the degree of glaciation 'γ'. The symbols L_v and L_s are the magnitudes of latent heating for the vaporization and sublimation processes, respectively; r_{sl} and r_{si} are the saturation vapor pressures over liquid water and over ice, respectively. Also a fraction of liquid condensate is converted to ice (q_i^{KF}) in accordance with 'γ'. Below -15° C, all condensate freezes.

Precipitation is assumed to form continuously from cloud condensate (q_c^{KF}, q_i^{KF}) by autoconversion. The remaining condensate constitutes the water loading on the updraft. Precipitation efficiency is determined as an average of two estimates; one depending on the wind shear in the cloudy region (Fritsch and Chappell, 1980) and another depending on the height of the cloud base (Zhang and Fritsch, 1986) above the surface.

Convective time scale:

The convective adjustments computed in the KF scheme (i.e. tendencies of temperature, water vapor mixing ratio, cloud, rain and ice mixing ratios) are applied over the convective time scale τ. The time scale τ is estimated as the time it would take for the cloud to be advected across a grid element Δx. Thus, $\tau = \frac{\Delta x}{\overline{U}}$, where $\overline{U}$ is the mean wind speed over the cloud depth. A one hour and a 30-min upper and lower limits are imposed, respectively. As pointed out in Fritsch and Kain (1993) these limits on τ may be unrealistic in situations where the mean wind speed over the cloud layer is very weak or very strong.

The convective effects of cumulus clouds are represented by the following equations in the KF scheme:

$$\frac{\partial T}{\partial t} = \underbrace{-\tilde{w}\left(\Gamma + \frac{\partial T}{\partial z}\right)}_{A} + \underbrace{\frac{M_{ud}}{\tilde{M}}\left(T_u - T\right)}_{B} + \underbrace{\frac{M_{dd}}{\tilde{M}}\left(T_d - T\right)}_{C} - \underbrace{\frac{M_{ud}}{\tilde{M}}\frac{r_c L}{C_p}}_{D} \tag{A.28}$$

and

$$\frac{\partial q_v}{\partial t} = \underbrace{-\tilde{w}\left(\Gamma + \frac{\partial q_v}{\partial z}\right)}_{A} + \underbrace{\frac{M_{ud}}{\tilde{M}}\left(r_u - q_v\right)}_{B} + \underbrace{\frac{M_{dd}}{\tilde{M}}\left(r_d - q_v\right)}_{C} - \underbrace{\frac{M_{ud}}{\tilde{M}} r_c}_{D} \tag{A.29}$$

where r_u, r_d represent the updraft and downdraft water vapor mixing ratios, respectively, at a given level; M_{ud} and M_{dd} are the detrainment rates from the updraft and downdraft (in units of kg s^{-1}), respectively. The effective mass of environmental air represented by each model layer and the compensating subsidence are denoted by $\tilde{M}$ and $\tilde{w}$, respectively. The terms A,B,C,D respectively denote the vertical advection of T or q_v by compensating environmental vertical motions (A), the effects of detrainment of updraft (B) and downdraft (C) mass into the environment, and the evaporation/sublimation of detrained condensate in the environment (D).

The cloud base in the KF scheme is determined by mixing the lowest 60 hPa and raising it to its LCL. The cloud top is defined as the level where the updraft velocity first becomes negative. It is higher than the equilibrium temperature level obtained from applying the pseudo-adiabat to a temperature sounding. This permits overshooting cloud tops to be captured by the scheme.

Hydrometeor feedback to resolvable scales:

The KF scheme incorporates detrainment of hydrometeors q_c^{KF} and q_i^{KF}, which results in moistening of layers above 600 hPa (Kain and Fritsch, 1990). The time tendency of cloud liquid water and ice content are, respectively given by:

$$\frac{\Delta q_c}{\Delta t} = \frac{-\delta_u q_{cu}}{\Delta p} \tag{A.30}$$

$$\frac{\Delta q_i}{\Delta t} = \frac{-\delta_u q_{iu}}{\Delta p} \tag{A.31}$$

where the detrainment rate of updrafts is given by

$$\delta_u = -\frac{M_{ud} g}{(\Delta x)^2}$$

where g is the earth's gravitational acceleration. q_{cu} and q_{iu} are the mean updraft cloud liquid water and ice mixing ratios, respectively. The right hand side of Eqns. (A.30) - (A.31) constitutes a source term for the explicit microphysics scheme, and Δp is the pressure interval between model levels.

Trigger function:

The function to determine when and where deep convection would occur in a mesoscale model is referred to as the trigger function. In the KF scheme, beginning with the lowest 60 hPa layer, the LCL for a mixed-layer parcel with layer mean virtual temperature and mixing ratio is determined. At the LCL, the parcel is checked for buoyancy using

$$T_U^S - T_{LCL} + \Delta T = \begin{cases} > 0 \text{ buoyant} \\ < 0 \text{ stable} \end{cases} \tag{A.32}$$

where T_U^S is the saturated updraft virtual temperature at the LCL, T_{LCL} is the virtual temperature at the LCL, $\Delta T = C_1(w)^{\frac{1}{3}}$, where $C_1 = 4.54$ a dimensional constant with units of K $(\mathrm{m})^{-\frac{1}{3}}$, and w is the grid scale vertical velocity. ΔT is the temperature perturbation caused by the large scale ascent in the mesoscale model at the LCL.

If the mixed parcel from the lowest 60 hPa is found stable, then the next 60 hPa layer above the previous level is mixed, lifted and checked for buoyancy. This process is repeated upto 300 hPa from the surface. If the parcel is found to be stable in the lowest 300 hPa, then convection does not occur. If the parcel is buoyant, then updraft calculation commences.

A.4.5 Explicit Microphysics

Simulation of mesoscale precipitation systems yielded best results when a CPS is jointly used with explicit microphysics (Zhang *et al.*, 1988; Molinari and Dudek, 1992). It was found that this combination allowed for a broader scale interaction between parameterized convection and the large scale environment. Molinari and Dudek (1992) emphasized the use of such 'hybrid approach' at grid sizes of around 20 km. In the present study, the explicit microphysics scheme of Kong and Yau (1997) is employed. The various microphysical processes and their interaction are briefly described below. The addition of water loading on the grid-scale vertical motion and the treatment of sedimentation of rain and ice are also described.

The schematic A.2 shows the various microphysical processes. The symbols used

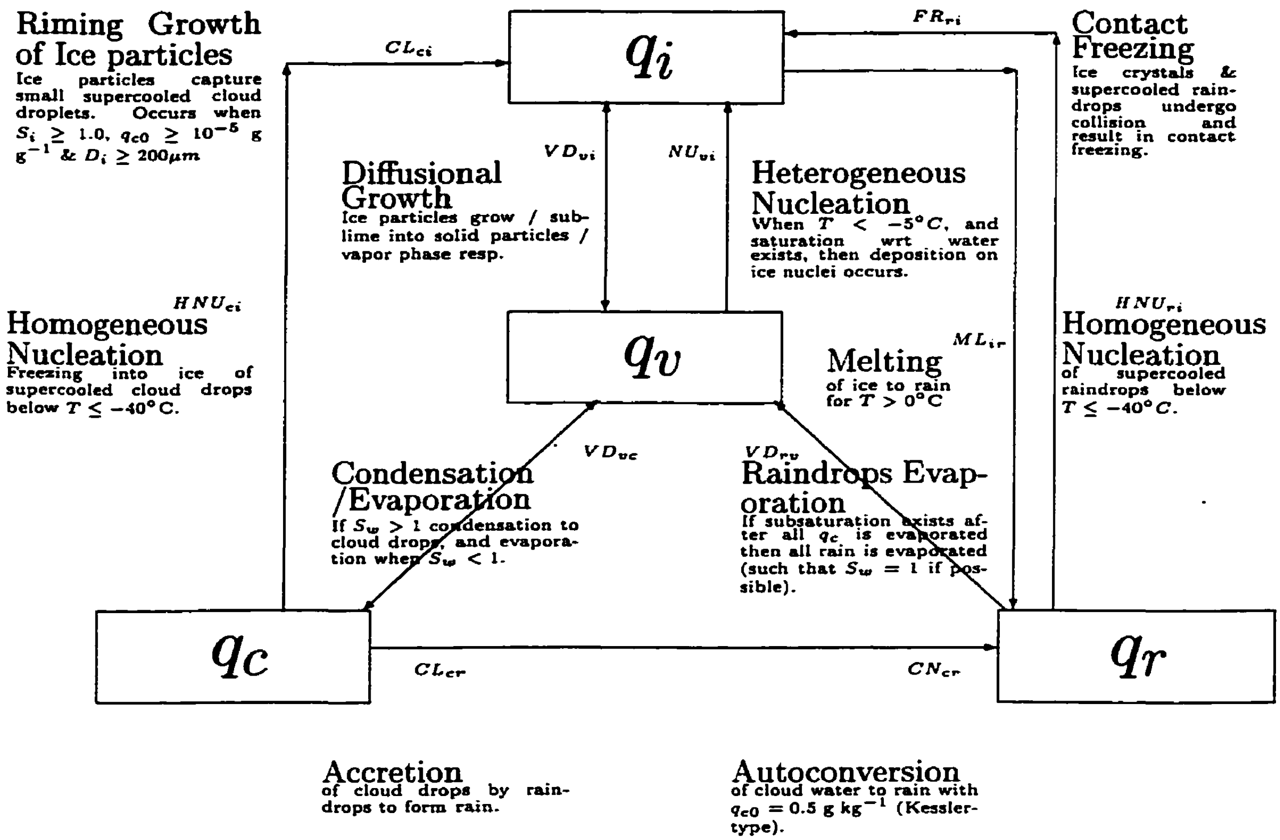

Figure A.2: The microphysical processes in the explicit scheme in the schematic are explained in Table A.1

Symbols	Meaning
CL_{ci}	Growth of ice particles by riming
CL_{cr}	Accretion of cloud drops by raindrops
CN_{cr}	Autoconversion of cloud drops to rain
FR_{ri}	Accretion of supercooled raindrops by ice crystals
HNU_{ci}	Homogeneous freezing of cloud drops
HNU_{ri}	Homogeneous freezing of rain drops
ML_{ir}	Melting of ice particles to rain
NU_{vi}	Deposition nucleation on active ice nuclei
VD_{rv}	Evaporation of rain to vapor
VD_{vc}	Condensation of vapor to cloud drops
VD_{vi}	Deposition of vapor to ice
S_i, S_w	Supersaturation wrt ice and water
D_i	Average diameter of ice particles
q_{c0}	Minimum mass of cloud liquid water content

Table A.1: Symbols used in Fig. A.2 and in the explicit microphysics equations.

From equations (A.6) - (A.9)

$$\frac{dq_v}{dt} = E = -VD_{vc} + VD_{rv} - VD_{vi} - NU_{vi} \tag{A.33}$$

$$\frac{dq_c}{dt} = S_C = VD_{vc} - CL_{cr} - CN_{cr} - CL_{ci} - HNU_{ci} \tag{A.34}$$

$$\frac{dq_r}{dt} = S_R = P_R + CL_{cr} + CN_{cr} - VD_{rv} - HNU_{ri} - FR_{ri} + ML_{ir} \tag{A.35}$$

$$\frac{dq_i}{dt} = S_I = P_I + VD_{vi} + NU_{vi} + HNU_{ci} + HNU_{ri} + CL_{ci} + FR_{ic} - ML_{ir} \quad \text{(A.36)}$$

where P_R, P_I are the precipitation (sedimentation) terms of rain and ice, respectively.

The microphysical terms shown above are associated with latent heating in the thermodynamic equation with the form

$$\begin{aligned} Q &= \frac{dT}{dt} \\ &= \frac{L_v}{C_p}(VD_{vc} - VD_{rv}) \\ &+ \frac{L_f}{C_p}(HNU_{ci} + HNU_{ri} + FR_{ri} + CL_{ci} - ML_{ir}) \\ &+ \frac{L_s}{C_p}(NU_{vi} + VD_{vi}) \end{aligned} \quad \text{(A.37)}$$

where L_v, L_f are the latent heat of condensation and fusion, respectively, with $L_s = L_v + L_f$.

When latent heat release in updrafts is intense, grid-scale conditional instability of the second kind (CISK)-like instability is likely to result. This may be reduced by inclusion of water loading effects associated with cloud hydrometeors. Thus, the drag force due to hydrometeors loading $-gq_t$ is included in Eq. (A.3) (not shown) where $q_t = q_c + q_r + q_i$.

Since the MC2 physics package uses pressure as the vertical coordinate, the sedimentation terms P_R, P_I are written as

$$P_x = -g\frac{\partial \rho V_x q_x}{\partial p} \quad \text{(A.38)}$$

where the subscript x denotes R or I. Since the fall speed of rain can reach several metres per second with grid scale vertical velocity being typically on the order of cm s^{-1} in mesoscale models, the use of a large time step in model integration can render the hydrometeor fields noisy and numerical instabilities may result. To address this problem, time splitting is applied for the sedimentation terms, where the small time step is given by

$$\Delta\tau = \frac{\Delta p}{9.8\rho V_r}$$

where Δp is the pressure interval between the lowest two model levels where the vertical resolution is the highest, V_r is the fall speed of rain obtained by choosing a maximum q_r value of 10 g kg^{-1} and ρ is the air density.

A.4.6 Surface energy balance

The surface skin temperature and soil moisture fraction (volume of water per unit volume of soil) are modeled using the scheme of Benoit *et al.* (1989). The model for soil temperature and moisture fraction represents the heat and water balance at the air-soil interface. The balance includes solar and infrared fluxes, sensible and latent heat fluxes, precipitation mass flux and heat and water diffusion into the soil. The balance is cast in the force-restore framework suggested by Deardorff (1978).

References

Asselin, R.A. (1972). Frequency filter for time integrations. *Mon. Wea. Rev.*, 100:487–490.

Belair, S. (1996). *Personal Communication.*

Benoit, R, J. Cote, and J. Mailhot (1989). Inclusion of a TKE boundary layer parameterization in the Canadian regional finite-element model. *Mon. Wea. Rev.*, 117:1726–1750.

Benoit, R., M. Desgagne, P. Pellerin, S. Pellerin, Y. Chartier, and S. Desjardins (1997). The Canadian MC2: A semi-implicit semi-Lagrangian wide-band atmospheric model suited for fine-scale process studies and simulation. *Mon. Wea. Rev.*, 125:2382–2415.

Bergeron, G., R. Laprise, D. Caya, A. Robert, M. Giguere, R. Benoit, and Y. Chartier (1994). Formulation of the Mesoscale Compressible Community MC2 model. Cooperative Center for Research in Mesometeorology. pages 1–165.

Betts, A. K. and M.J. Miller (1993). The Betts-Miller scheme, Chapter 9. In *The representation of cumulus convection in numerical models of the atmosphere*, (Eds. K.A. Emanuel and D.J. Raymond),Meteo. Mon., pages 107–121. American Meteorological Society.

Betts, A.K. (1982). Cloud thermodynamic models in saturation point coordinates. *J. Atmos. Sci.*, 39:2182–2191.

Betts, A.K. (1986). A new convective adjustment scheme. Part I: Observational and theoretical basis. *Quart. J. Roy. Meteor. Soc.*, 112:667–691.

Betts, A.K. (1997). The parameterization of deep convection. In Smith, R.K. , editor, *The physics and parameterization of moist atmospheric convection*, pages 255–279. Kluwer Academic Publishers.

Betts, A.K. and Harshavardhan (1987). Thermodynamic constraint on the cloud liquid water feedback in climate models. *J. Geophys. Res.*, 92:8483–8485.

Brown, R.G. and C. Zhang (1997). Variability of midtropospheric moisture and its effect on cloud-height distribution during TOGA COARE. *J. Atmos. Sci.*, 54:2760–2774.

Chen, S.S. and R. A. Houze (1997). Diurnal variation and life-cycle of deep convective systems over the tropical Pacific warm pool. *Quart. J. Roy. Meteor. Soc.*, 123:357–388.

Chong, M. and D. Hauser (1990). A tropical squall line observed during the COPT81 experiment in west Africa. Part III: Heat and moisture budgets. *Mon. Wea. Rev.*, 118:1696–1706.

Cooper, D.I., W.E. Eichinger, S. Barr, W. Cottingame, M.V. Hynes, C.F. Keller, C.F. Lebeda, and D.A. Poling (1996). High-resolution properties of the equatorial Pacific marine atmospheric boundary layer from lidar and radiosonde observations. *J. Atmos. Sci.*, 53:2054–2075.

Crook, N.A. (1996). Sensitivity of moist convection forced by boundary layer processes to low-level thermodynamic fields. *Mon. Wea. Rev.*, 124:1767–1785.

Davies, H.C. (1976). A lateral boundary formulation for multi-level prediction models. *Quart. J. Roy. Meteor. Soc.*, 102:405–418.

Deardorff, J.W. (1978). Efficient prediction of ground surface temperature and moisture with inclusion of a layer of vegetation. *J. Geophys. Res.*, 83:1889–1903.

Ebert, E.E. and J.A. Curry (1992). A parameterization of ice cloud optical properties for climate models. *J. Geophys. Res.*, 97:3831–3836.

Fairall, C.W., E. F. Bradley, J. S. Godfrey, G. A. Wick, J.B. Edson, and G.S. Young (1996a). Cool-skin and warm layer effects on sea surface temperature. *J. Geophys. Res.*, 101:1295–1308.

Fairall, C.W., E. F. Bradley, D. P. Rogers, J. B. Edson, and G.S. Young (1996b). Bulk parameterization of air-sea fluxes for Tropical Ocean-Global Atmosphere Coupled -Ocean Atmosphere Response Experiment. *J. Geophys. Res.*, 101:3747–3764.

Fouquart, Y. and B. Bonnel (1980). Computation of solar heating of the earth's atmosphere: A new parameterization. *Contrib. Atmos. Phys.*, 53:35–62.

Frank, W.M. and C. Cohen (1985). Properties of tropical cloud ensembles estimated using a cloud model and an observed updraft population. *J. Atmos. Sci.*, 42:1911–1928.

Fritsch, J.M. and C.F. Chappell (1980). Numerical prediction of convectively driven mesoscale pressure systems. Part I: Convective parameterization. *J. Atmos. Sci.*, 37:1722–1733.

Fritsch, J.M. and J. Kain (1993). Convective parameterization for mesoscale models: The Fritsch-Chappel scheme, Chapter 15. In *The representation of cumulus convection in numerical models of the atmosphere*, (Eds. K.A. Emanuel and D.J. Raymond),Meteo. Mon., pages 159–164. American Meteorological Society.

Garand, L. (1983). Some improvements and complements to the infrared emissivity algorithm including a parameterization of the absorption in the continuum region. *J. Atmos. Sci.*, 40:230–244.

Garand, L. and J. Mailhot (1990). The influence of infrared radiation on numerical weather forecasts. In *Proceedings of the seventh conference on atmospheric radiation, San Francisco, USA*, pages J146–J151. American Meteorological Society.

Garstang, M. and A.K Betts (1974). A review of the tropical boundary layer and cumulus convection: Structure, parameterization, and modeling. *Bull. Amer. Meteor. Soc.*, 55:1195–1205.

Geleyn, J.-F. (1986). Use of a modified Richardson number for parameterizing the effect of shallow convection. In *Short- and Medium-range numerical weather prediction, Collection of papers presented at the WMO/IUCGG NWP Symposium, Tokyo, 4-8 August, 1986*, pages 141–149.

Godrey, J.S., R.A. Houze, R.H. Johnson, R. Lukas, J.-L. Redelsperger, A. Sumi, and R. Weller (1998). Coupled Ocean-Atmosphere Response Experiment COARE: An interim report. *J. Geophys. Res.*, 103:14395–14450.

Grant, A.L.M. and P. Hignett (1998). Aircraft observations of the surface energy balance in TOGA-COARE. *Quart. J. Roy. Meteor. Soc.*, 124:101–122.

Gregrory, D. and M.J. Miller (1989). A numerical study of the parameterization of deep tropical convection. *Quart. J. Roy. Meteor. Soc.*, 115:1209–1241.

Hagan, D., D. Rogers, C. Friehe, R. Weller, and E. Walsh (1997). Aircraft observations of sea surface temperature variability in the tropical Pacific. *J. Geophys. Res.*, 102:15733–15747.

Hartmann, D. H., H. Hendon, and R. A. Houze (1984). Some implications of the mesoscale circulations in tropical cloud clusters for large-scale dynamics and climate. *J. Atmos. Sci.*, 41:850–852.

Heymsfield, A. J., G. M. McFarquhar, W. D. Collins, J. A. Goldstein, F. P. J. Valero, J. Spinhirne, W. Hart, and P. Pilewskie (1998). Cloud properties leading to highly reflective tropical cirrus: interpretations from CEPEX, TOGA COARE, and Kwajalein, Marshall islands moisture with inclusion of a layer of vegetation. *J. Geophys. Res.*, 103:8805–8812.

Houze, R. A. (1989). Observed struture of mesoscale convective systems and implications for large scale heating. *Quart. J. Roy. Meteor. Soc.*, 115:425–461.

Houze, R.A. and A.K. Betts (1981). Convection in GATE. *Rev. Geophys.*, 19:541–576.

Jabouille, P., J.L. Redelsperger, and J.P. Lafore (1996). Modification of surface fluxes by atmospheric convection in the TOGA COARE region. *Mon. Wea. Rev.*, 124:816–837.

Jakimow, G., E. Yakimiw, and A. Robert (1992). An implicit formulation for the horizontal diffusion in grid point models. *Mon. Wea. Rev.*, 120:124–130.

Johnson, R. H. (1984). Partitioning tropical heat and moisture budgets into cumulus and mesoscale components: Implications for cumulus parameterization. *Mon. Wea. Rev.*, 112:1590–1601.

Kain, J. and M.E. Baldwin (1999). Parameterized convection and the quantitative precipitation problem. In *23rd conference on Hurricanes and tropical meteorology Volume II*, pages 870–872. American Meteorological Society.

Kain, J.S. and J. M. Fritsch (1992). The role of the convective 'trigger' function in numerical forecasts of mesoscale convective systems. *Meteor. Atmos. Phys.*, 49:93–106.

Kain, J.S. and J.M. Fritsch (1990). A one-dimensional entraining /detraining plume model and its application in convective parameterization. *J. Atmos. Sci.*, 47:2784–2802.

Kallberg, P. (1977). Test of a lateral boundary relaxation scheme in a barotropic model. Report, ECMWF, Research Department, Internal Report 3.

Kingsmill, D.E. and R.A. Houze (1999). Kinematic characteristics of air flowing into and out of precipitating convection over the west Pacific warm pool: an airborne Doppler radar survey. *Quart. J. Roy. Meteor. Soc.*, 125:1165–1207.

Kodama, K.R. and S. Businger (1998). Weather and forecasting challenges in the Pacific region of the National Weather Service. *Wea. Forecasting*, 13:523–546.

Kong, F.Y. and M.K. Yau (1997). An explicit approach to microphysics in MC2. *Atmosphere-Ocean*, 35:257–291.

Leary, C. A. and R.A. Houze (1979). The structure and evolution of convection in a tropical cloud cluster. *J. Atmos. Sci.*, 36:437–457.

Leary, C.A. and R.A. Houze (1980). Contribution of mesoscale motions to the mass and heat fluxes of an intense tropical convective system. *J. Atmos. Sci.*, 37:784–796.

LeMone, M.A., E.J. Zipser, and S.B. Trier (1998). The role of environmental shear and thermodynamic conditions in determining the structure and evolution of mesoscale convective systems during TOGA COARE. *J. Atmos. Sci.*, 55:3493–3518.

Lewis, J. M. (1975). Test of the Ogura-Cho model on a prefrontal squall line case. *Mon. Wea. Rev.*, 103:764–778.

Lin, X. and R. H. Johnson (1996a). Heating, moistening, and rainfall over the western Pacific warm pool during TOGA COARE. *J. Atmos. Sci.*, 53:3367–3383.

Lin, X. and R. H. Johnson (1996b). Kinematic and thermodynamic characteristics of the flow over the western Pacific warm pool during TOGA COARE. *J. Atmos. Sci.*, 53:695–715.

Lucas, C., E.J. Zipser, and M.A. LeMone (1994). Vertical velocity in oceanic convection off tropical Australia. *J. Atmos. Sci.*, 51:3183–3193.

Lukas, R (1991). The diurnal cycle of sea surface temperature in the western equatorial pacific. *TOGA Notes*, 2:1–5.

Mailhot, J. (1994). The regional finite-element (RFE) model Scientific description - Part 2: Physics Numerical Prediction Research Division, AES.

Mailhot, J., S. Belair, R. Benoit, B. Bilodeau, Y. Delage, L. Fillion, L. Garand, C. Girard, and A. Tremblay (1998). Scientific description of RPN physics library Version 3.6. pages 1–188.

Mangum, L. J., H. P. Freitag, and M. J. McPhaden (1994). TOGA-TAO array sampling schemes and sensor evaluations. In *Proceedings of the Oceans'94, Brest, France, 13-16 September 1994*, pages 402–406.

Mapes, B.E. (1993). Gregarious tropical convection. *J. Atmos. Sci.*, 50:2026–2037.

Mapes, B.E. and R. A. Houze (1987). An integrated view of the 1987 Australian monsoon and its mesoscale convective systems. *Quart. J. Roy. Meteor. Soc.*, 119:733–754.

Mapes, B.E. and R.A. Houze (1993). Cloud clusters and superclusters over the oceanic warm pool. *Mon. Wea. Rev.*, 121:1398–1415.

McBride, J.L., N.E. Davidson, K. Puri, and G.C. Tyrell (1995). The flow during TOGA COARE as diagnosed by the BMRC tropical analysis and prediction system. *Mon. Wea. Rev.*, 123:717–736.

McBride, J.L., B.W. Gunn, G.J. Holland, T.D. Keenan, and N.E. Davidson (1989). Time series of total heating and moistening over the Gulf of Carpentaria radiosonde array during AMEX. *Mon. Wea. Rev.*, 117:2701–2713.

McFarquhar, G. M. and A. J. Heymsfield (1996). Microphysical characteristics of three cirrus anvils sampled during the Central Equatorial Pacific Experiment. *J. Atmos. Sci.*, 53:2401–2423.

McFarquhar, G. M. and A. J. Heymsfield (1997). Parameterization of tropical cirrus ice crystal size distributions and implications for radiative transfer: Results from CEPEX. *J. Atmos. Sci.*, 54:2187–2200.

McNider, R.T., J.A. Song, and S.Q. Kidder (1995). Assimilation of GOES-derived solar insolation into a mesoscale model for studies of cloud shading effects. *Int. J. Remote Sensing*, 16:2207–2231.

Molinari, J. and M. Dudek (1992). Parameterization of convective precipitation in mesoscale numerical models: A critical review. *Mon. Wea. Rev.*, 120:326–344.

Nakazawa, T. (1988). Tropical cloud clusters within intraseasonal variations over the western Pacific. *J. Meteor. Soc. Japan*, 66:823–839.

Nitta, T. (1977). Response of cumulus updraft and downdraft to GATE A/B-scale motion systems. *J. Atmos. Sci.*, 34:1163–1186.

Numaguti, A. (1995). Characteristics of 4-to-20 day period disturbances observed in the equatorial Pacific during the TOGA COARE IOP. *J. Meteor. Soc. Japan*, 73:353–377.

Nuret, M and M. Chong (1996). Monitoring the performance of the ECMWF operational analysis using the enhanced TOGA COARE observational network. *Wea. Forecasting*, 11:53–65.

Nuret, M. and M. Chong (1998). Characteristics of heat and moisture budgets of a mesoscale convective system observed during TOGA-COARE. *Quart. J. Roy. Meteor. Soc.*, 124:1163–1181.

Peaceman, D.W. and H.H. Rachford (1955). The numerical solution of parabolic and elliptic differential equations. *J. Soc. Indust. Appl. Math.*, 3:28–41.

Protat, A. (1999). *Personal Communication.*

Protat, A., Y. Lemaitre, and G. Scialom (1996). Scale interactions involved in the initiation and evolution of mesoscale convective systems observed during TOGA COARE. In *27th conference on Radar Meteorology*, pages 734–736. American Meteorological Society.

Protat, A., Y. Lemaitre, and G. Scialom (1997). Retrieval of kinematic fields using a single-beam airborne Doppler radar performing circular trajectories. *J. Appl. Meteor.*, 14:769–791.

Protat, A., Y. Lemaitre, and G. Scialom (1998). Thermodynamic analytic fields from Doppler-radar data by means of the MANDOP analysis. *Quart. J. Roy. Meteor. Soc.*, 124:1633–1668.

Ramage, C. S. (1971). *Monsoon Meterology*, volume 15, 296 pp. Academic Press.

Raymond, D.J. (1995). Regulation of moist convection over the west Pacific warm pool. *J. Atmos. Sci.*, 52:3945–3959.

Rickenbach, T. M. and S. A. Rutledge (1998). Convection in TOGA COARE: horizontal scale, morphology, and rainfall production. *J. Atmos. Sci.*, 55:2715–2729.

Riddle, A. C., W. M. Angevine, W. L. Ecklund, E. R. Miller, D. B. Parsons, D. A. Carter, and K. S. Gage (1996). In situ and remotely sensed horizontal winds and temperature intercomparisons obtained using integrated sounding systems during TOGA COARE. *Contrib. Atmos. Phys.*, 69:49–61.

Ritchie, H. and M. Tanguay (1996). A comparison of spatially averaged Eulerian and semi-Lagrangian treatments of mountains. *Mon. Wea. Rev.*, 124:167–181.

Robert, A. (1993). Bubble convection experiments with a semi-implicit formulation of the Euler equations. *J. Atmos. Sci.*, 50:1865–1873.

Rogers, R.F. and J.M. Fritsch (1996). A general framework for convective trigger function. *Mon. Wea. Rev.*, 124:2438–2452.

Sherwood, S.C. (1999). Convective precursors and predictability in the tropical western Pacific. *Mon. Wea. Rev.*, 127:2977–2991.

Sherwood, S.C. and R. Wahrlich (1999). Observed evolution of tropical deep convective events and their environment. *Mon. Wea. Rev.*, 127:1777–1795.

Sheu, R-S., J. A. Curry, and G. Liu (1996). Satellite retrieval of tropical precipitation using combined International Satellite Cloud Climatology project DX and SSM/I data. *J. Geophys. Res.*, 101:21291–21301.

Short, D. A., P. A. Kucera, B.S. Ferrier, J.C. Gerlach, S. A. Rutledge, and O.W. Thiele (1997). Shipboard radar rainfall patterns within the TOGA COARE IFA. *Bull. Amer. Meteor. Soc.*, 78:2817–2836.

Siebesma, P. (1998). Shallow cumulus convection. In Plate, E.J., E.E. Fedorovich, X.V. Viegas, and J.C. Wyngaard , editors, *Buoyant convection in geophysical flows*, pages 441–486. Kluwer Academic Publishers.

Slingo, A. (1989). A GCM parameterization for the shortwave radiative properties of water clouds. *J. Atmos. Sci.*, 46:1419–1427.

Slingo, J. M. (1987). Development and verification of a cloud prediction scheme for the ECMWF model. *Quart. J. Roy. Meteor. Soc.*, 113:899–927.

Stensrud, D.J. and J.-W. Bao (1992). Behaviors of variational and nudging assimilation techniques with a chaotic low-order model. *Mon. Wea. Rev.*, 120:3016–3028.

Stensrud, D.J and J.M. Fritsch (1994). Mesoscale convective systems in weakly forced large-scale environments. Part II: Generation of a mesoscale initial condition. *Mon. Wea. Rev.*, 122:2068–2083.

Stephens, G.L. (1984). The parameterization of radiation for numerical weather prediction and climate models. *Mon. Wea. Rev.*, 112:826–867.

Sui, C.-H., X. Li, K.-M. Lau, and D. Adamec (1997). Multiscale air-sea interactions during TOGA COARE. *Mon. Wea. Rev.*, 125:448–462.

Takayabu, Y.N., K.-M. Lau, and C.-H. Sui (1996). Observation of a quasi-2-day wave during TOGA COARE. *Mon. Wea. Rev.*, 124:1892–1913.

Tanguay, M., A. Robert, and R. Laprise (1990). A semi-implicit semi-Lagrangian fully compressible regional forecast model. *Mon. Wea. Rev.*, 118:1970–1980.

Tanguay, M., A. Simard, and A. Staniforth (1989). A three-dimensional semi-Lagrangian scheme for the Canadian regional finite-element forecast model. *Mon. Wea. Rev.*, 117:1861–1871.

Tanguay, M., E. Yakimiw, H. Ritchie, and A. Robert (1992). Advantages of spatial averaging in semi-Lagrangian schemes. *Mon. Wea. Rev.*, 120:113–123.

Thompson, R. M., S.W. Payne, W.W. Recker, and R.J. Reed (1979). Structure of synoptic-scale wave disturbances in the intertropical convergence zone of the eastern Atlantic ocean. *J. Atmos. Sci.*, 36:53–71.

Tiedtke, M. (1993). Representation of clouds in large-scale models. *Mon. Wea. Rev.*, 121:3040–3061.

Tiedtke, M., W.A. Heckley, and J. Slingo (1988). Tropical forecasting at ECMWF: the influence of physical parameterization on the mean structure of forecasts and analyses. *Quart. J. Roy. Meteor. Soc.*, 114:639–664.

Tollerud, E. I. and S. K. Esbensen (1985). A composite life cycle of nonsquall mesoscale convective systems over the tropical ocean. Part I: Kinematic fields. *J. Atmos. Sci.*, 42:823–837.

Ullrich, F. (1995). Interaction between deep convection and shortscale gravity waves. *Raumfahrt e. V.*, page 106.

Webster, P. J., C.A. Clayson, and J. A. Currie (1996). Clouds, radiation, and the diurnal cycle of sea surface temperature in the tropical western Pacific. *J. Climate*, 9:1712–1730.

Webster, P.J. and R. Lukas (1992). TOGA COARE: The Coupled Ocean Atmosphere Response Experiment. *Bull. Amer. Meteor. Soc.*, 73:1377–1416.

Weller, R.A. and S.P. Anderson (1996). Surface meteorology and air-sea fluxes in the western equatorial Pacific warm pool during the TOGA Coupled Ocean-Atmosphere Response Experiment. *J. Climate*, 9:1959–1990.

Yakimiw, E. and A. Robert (1990). Validation experiments for a nested grid-point regional forecast model. *Atmosphere-Ocean*, 28:466–472.

Yanai, M., S. Esbensen, and J.H. Chu (1973). Determination of bulk properties of tropical cloud clusters from large-scale heat and moisture budgets. *J. Atmos. Sci.*, 30:611–627.

Young, G.S., D.V. Ledvina, and C.W. Fairall (1992). Influence of precipitating convection on the surface energy budget observed during a Tropical Ocean Global Atmosphere pilot cruise in the tropical western Pacific ocean. *J. Geophys. Res.*, 97:9595–9603.

Zhang, D.-L. and J.M. Fritsch (1986). Numerical simulation of the meso-β-scale structure and evolution of the 1977 Johnstown flood. Part I: Model description and verification. *Mon. Wea. Rev.*, 43:1913–1943.

Zhang, D.-L., E.-Y. Hsie, and M.W. Moncrieff (1988). A comparison of explicit and implicit predictions of convective and stratiform precipitating weather systems with a meso-β-scale numerical model. *Quart. J. Roy. Meteor. Soc.*, 114:31–60.